

# Properties & Design Equations for Silicon Carbide

Adam T. Ghoniem<sup>1</sup>

Nasr M. Ghoniem

**DRAFT**

September 7, 2007

Nasr M. Ghoniem, President

***DIGITAL MATERIALS SOLUTIONS (DMS)***



11809 Andasol Ave  
Granada Hills, CA. 91344

---

<sup>1</sup>aghoniem@gmail.com, Tel.(818) 373-9853

# Contents

<b>1</b>	<b>Introduction</b>	<b>2</b>
<b>2</b>	<b>Properties of Sintered <math>\alpha</math>-SiC</b>	<b>3</b>
2.1	Crystallography, Density and Lattice Expansion . . . . .	3
2.2	Elastic Properties . . . . .	7
2.3	Strength and Related Properties . . . . .	13
2.4	Creep Characteristics . . . . .	19
2.5	Tribological Characteristics . . . . .	24
2.6	Thermal Properties . . . . .	26
<b>3</b>	<b>Properties of Foam-SiC</b>	<b>32</b>
3.1	Manufacturing . . . . .	32
3.2	Thermal Properties of Foam-SiC . . . . .	36
3.2.1	Thermal Expansion . . . . .	36
3.2.2	Thermal conductivity, Diffusivity and Specific Heat . . . . .	39
3.3	Mechanical Properties of Foam-SiC . . . . .	46
3.3.1	Mechanical Test Results . . . . .	47
3.3.2	Property and Correlations . . . . .	48
3.4	Fluid Flow and Heat transfer . . . . .	59
<b>4</b>	<b>Radiation Effects on SiC Properties</b>	<b>67</b>
<b>A</b>	<b>Ashbys' Design Correlations[60]</b>	<b>96</b>
A.1	Mechanical Properties . . . . .	96
A.2	Thermal Properties . . . . .	97
A.3	Electrical Properties . . . . .	97

# 1 Introduction

Silicon carbide is one of the most important materials for high temperature applications because of its high strength and stiffness at high temperatures, and because it offers unparallel high temperature capabilities. The material finds applications in a wide range of industries, with primary use in structural components including heat exchanges, rocket engines, seals, bearings, and in automotive, nuclear and aerospace components. Because of its unique semi-conducting characteristics, it is also utilized in high temperature electronics. The material is now manufactured in several forms, such as sintered  $\alpha$ -SiC bulk ceramics, chemical vapor deposited (CVD) thin films, chemical vapor infiltrated (CVI) foam pre forms, and fiber-reinforced composite structure. It is therefore expected that properties will depend on the manufacturing process as well as the exact utilization condition

In this report, we assemble available experimental data on the properties of SiC in its various manufactured forms. The data is obtained from a variety of sources, which are all referenced for future quality assessments. The report is organized as follows.

First we present the properties of Sintered  $\alpha$ -SiC as the base line that will establish corresponding properties of open-foam and SiC/SiC composite forms. Most of the data is obtained from the excellent article by R.G. Munro [1], with our own data fits that are obtained independently. Then we present all available data on SiC foams, assembled primarily from Ultramet's tests and documentation. This includes manufacturing, thermal, mechanical, and fluid flow characteristics. Some of the main data on SiC/SiC composites, which are obtained from various sources, are then presented. The effects of radiation on the properties of SiC/SiC composites are then shown. Most of the radiation effects data are assembled from work performed for the Department of Energy (DoE) fusion materials program. In addition to the presentation of data and curve fits to this data, we design equations that can be useful in performing thermal and mechanical analyses of high-temperature components. Finally, we give our conclusions on future data ready in section 6.

## 2 Properties of Sintered $\alpha$ -SiC

### 2.1 Crystallography, Density and Lattice Expansion

The crystal structure of  $\alpha$ -SiC is predominantly the hexagonal 6H structure. The temperature dependence of the lattice parameters on the basal plan (a), and in the prismatic direction (c) is shown in Figures (1) and (2), respectively. The thermal expansion coefficient as a function of temperature is then shown in Figure(3), while the temperature dependence for the density for both single crystal (6H) and sintered  $\alpha$ -SiC is shown in Figure(4).

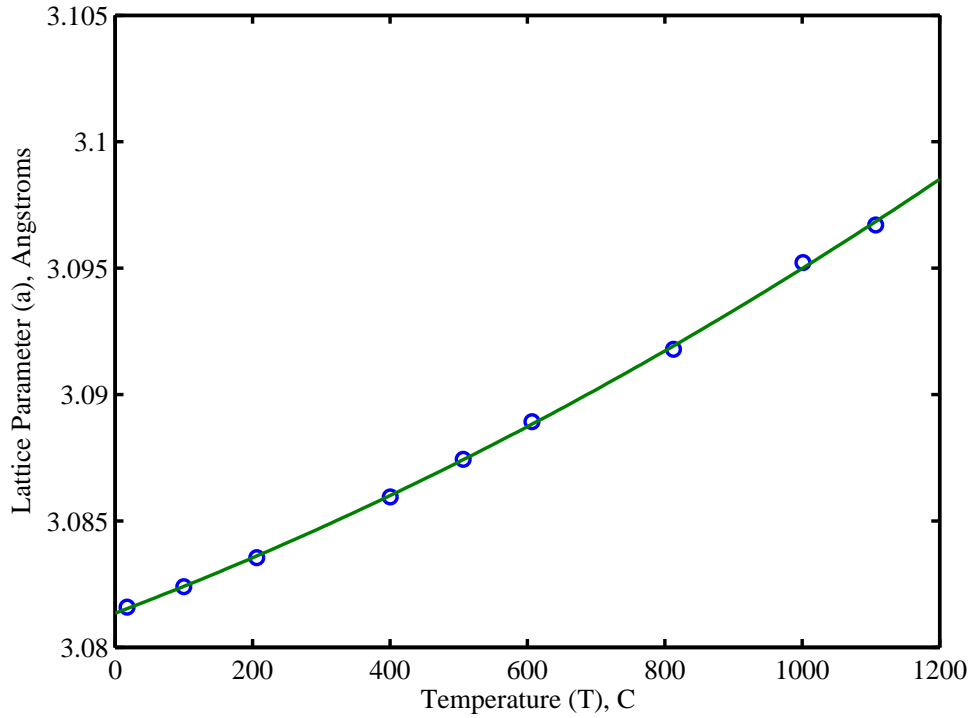


Figure 1: The lattice parameters of silicon carbide polytype 6H along the a-axis [2]

The variation of the lattice parameter ( $\text{\AA}$ ) with temperature ( $^{\circ}\text{C}$ ) for silicon carbide polytype 6H along the c-axis is shown in Figure (1) is described by the equation:

$$a = 2.883 \times 10^{-9}T^2 + 1082 \times 10^{-5}T + 3.081 \quad (1)$$

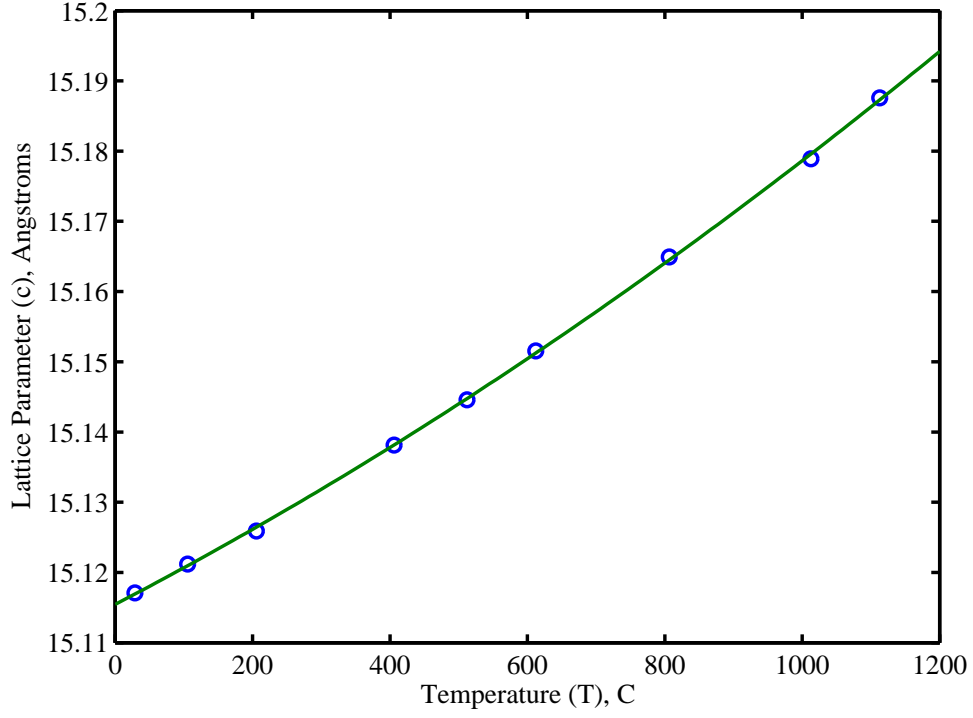


Figure 2: The lattice parameters of silicon carbide polytype 6H along the c-axis [2]

The variation of the lattice parameter ( $\text{\AA}$ ) with temperature ( $^{\circ}\text{C}$ ) for silicon carbide polytype 6H along the a-axis shown in Figure (2) is described by the equation:

$$c = 1.153 \times 10^{-8}T^2 + 5.099 \times 10^{-5}T + 15.116 \quad (2)$$

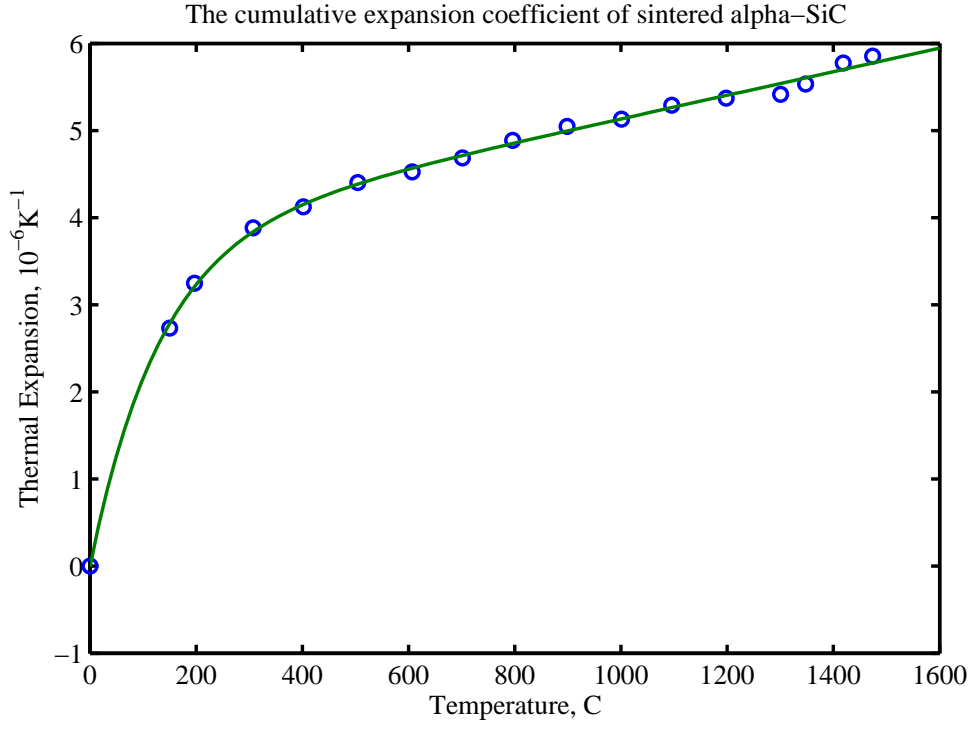


Figure 3: The thermal expansion of sintered  $\alpha$ -SiC density [3][4]

The thermal expansion coefficient of sintered  $\alpha$ -SiC as shown in Figure (3) is described by the equation:

$$a = 3.7842 + 1.351 \times 10^{-3}T - 3.789 \times 10^{-3}e^{7.649 \times 10^{-3}T} \quad (3)$$

where  $a$  is thermal expansion coefficient ( $10^{-6}\text{K}^{-1}$ ) and  $T$  is temperature ( $^{\circ}\text{C}$ )

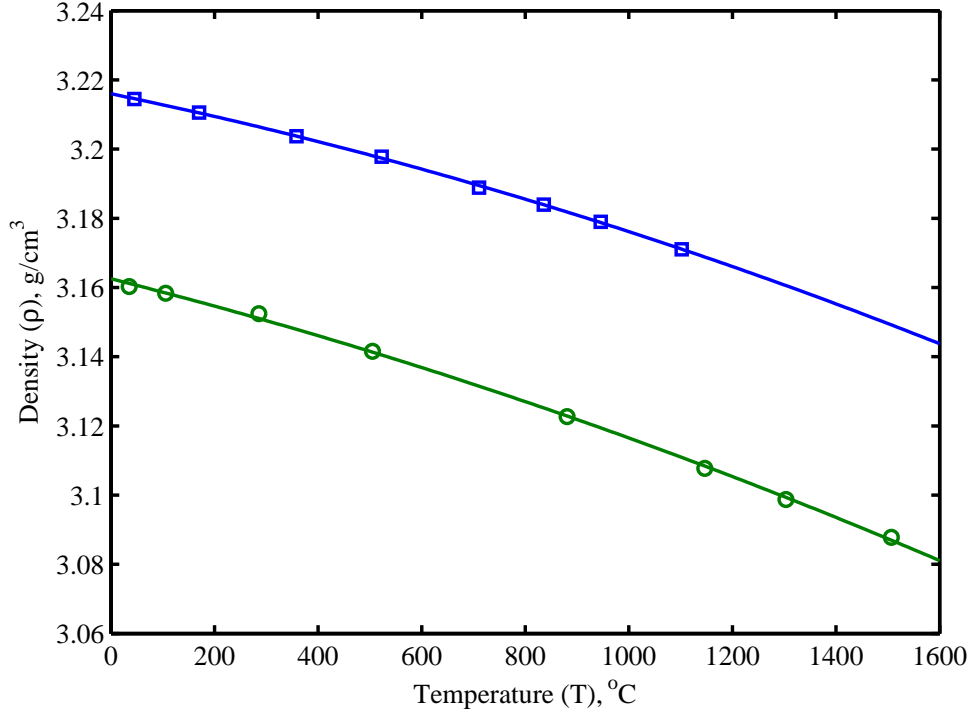


Figure 4: The density of single crystal (squares) and sintered  $\alpha$ -SiC (circles) [5][6][7]

The density ( $\text{g}/\text{cm}^3$ ) of single crystal 6H as a function of temperature ( $^{\circ}\text{C}$ ) as shown in Figure (4) is given by

$$\rho = -8.8349 \times 10^{-9}T^2 - 3.102 \times 10^{-5}T + 3.216 \quad (4)$$

The density ( $\rho, \frac{\text{g}}{\text{cm}^3}$ ) of sintered  $\alpha$ -SiC as a function of temperature ( $T, ^{\circ}\text{C}$ ) as shown in Figure (4) is described by the equation:

$$\rho = -8.159 \times 10^{-9}T^2 - 3.784 \times 10^{-5}T + 3.163 \quad (5)$$

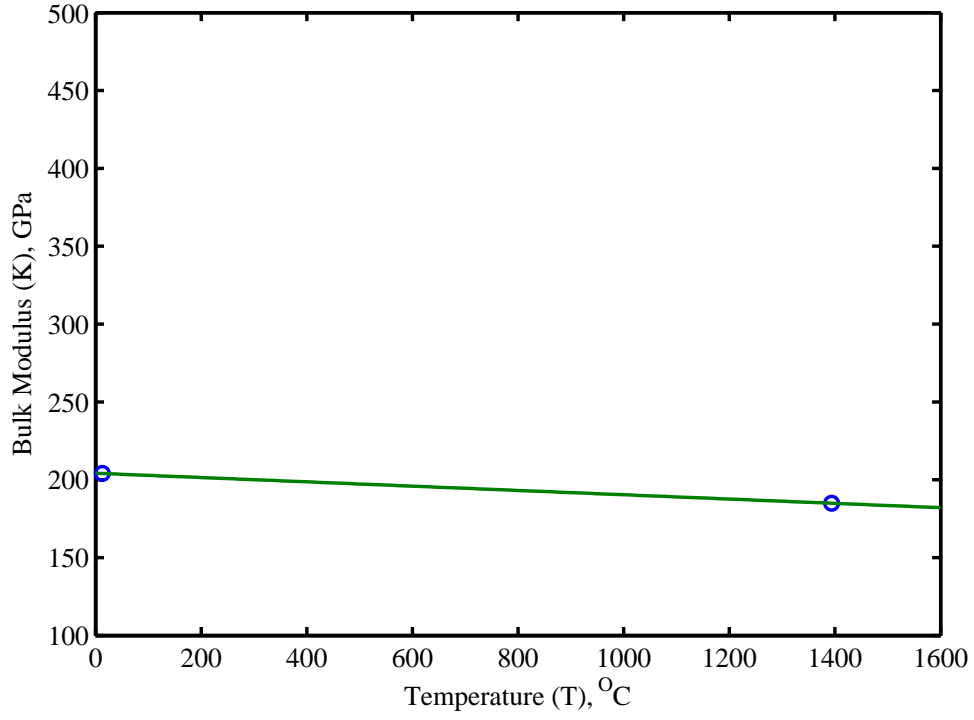


Figure 5: The Bulk Modulus as a function of Temperature for sintered  $\alpha$ -SiC [7, 6, 8, 4]

## 2.2 Elastic Properties

The bulk modulus (K, GPa) as a function of temperature (T, °C) for sintered  $\alpha$ -SiC as shown in Figure (5) is described by the equation:

$$K = -2.272 \times 10^{-2}T + 4.135 \quad (6)$$



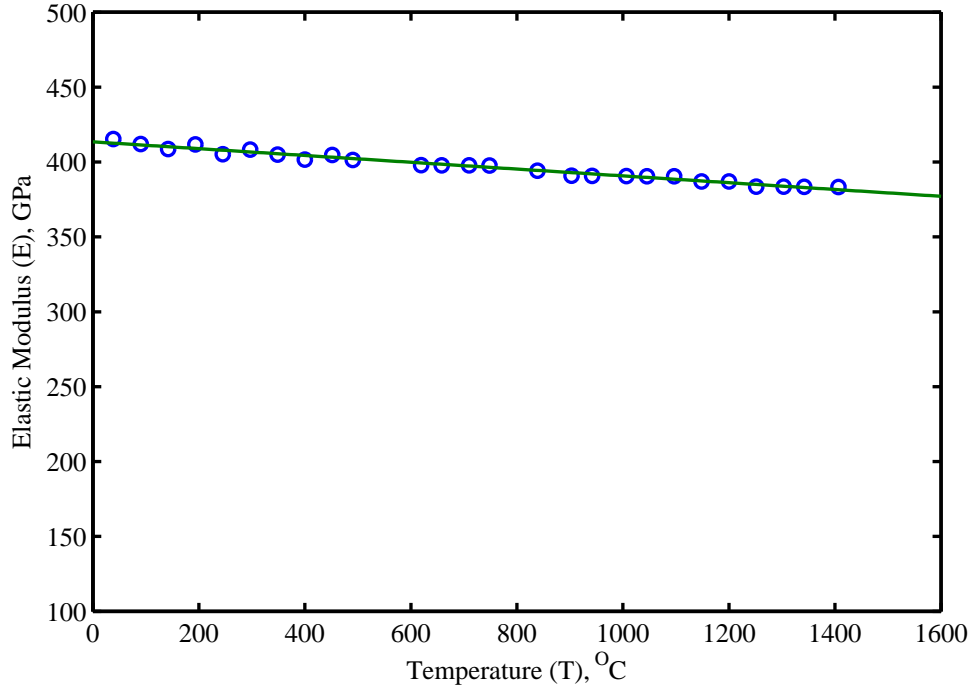


Figure 6: The Elastic Modulus as a function of Temperature for sintered  $\alpha$ -SiC [7, 6, 8, 4]

The elastic modulus (E, GPa) as a function of temperature (T, °C) for sintered  $\alpha$ -SiC as shown in Figure (6) is described by the equation:

$$E = -1.382 \times 10^{-2}T + 2.0421 \times 10^2 \quad (7)$$

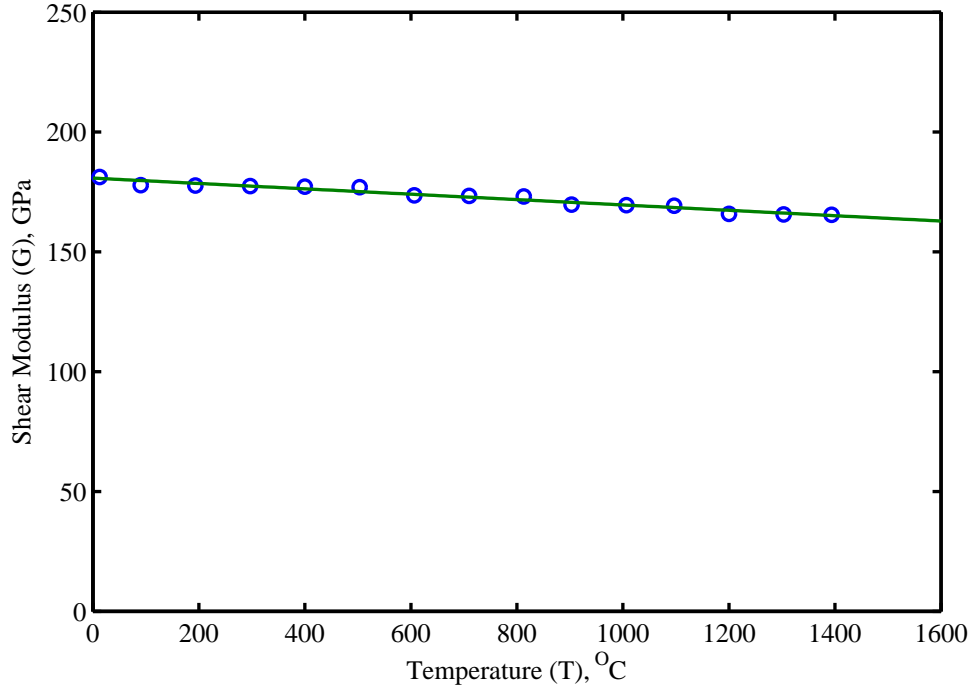


Figure 7: The Shear Modulus as a function of Temperature for sintered  $\alpha$ -SiC [7, 6, 8, 4]

The shear modulus ( $G$ , GPa) as a function of temperature ( $T$ , °C) for sintered  $\alpha$ -SiC as shown in Figure (7) is easily described by the equation:

$$G = -1.121 \times 10^{-2}T + 2.042 \times 10^2 \quad (8)$$

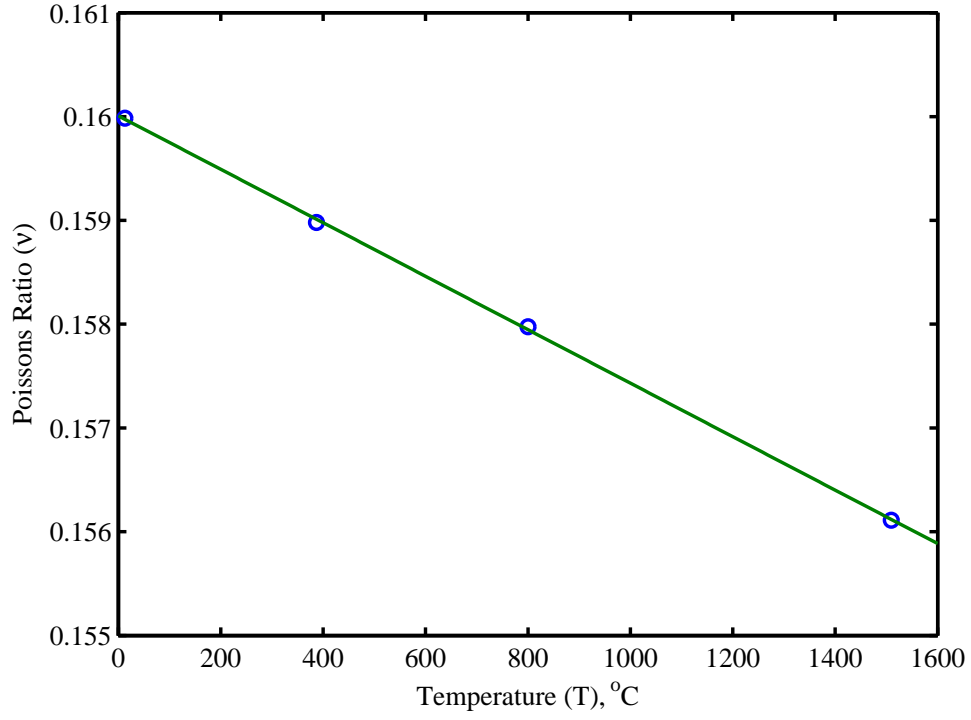


Figure 8: Poisson's ratio as a function of Temperature for sintered  $\alpha$ -SiC [7, 6, 8, 4]

Poisson's ratio as a function of temperature (T, °C) for sintered  $\alpha$ -SiC as shown in Figure (8) is easily described by the equation:

$$\nu = -2.577 \times 10^{-6}T + 1.6 \times 10^{-1} \quad (9)$$

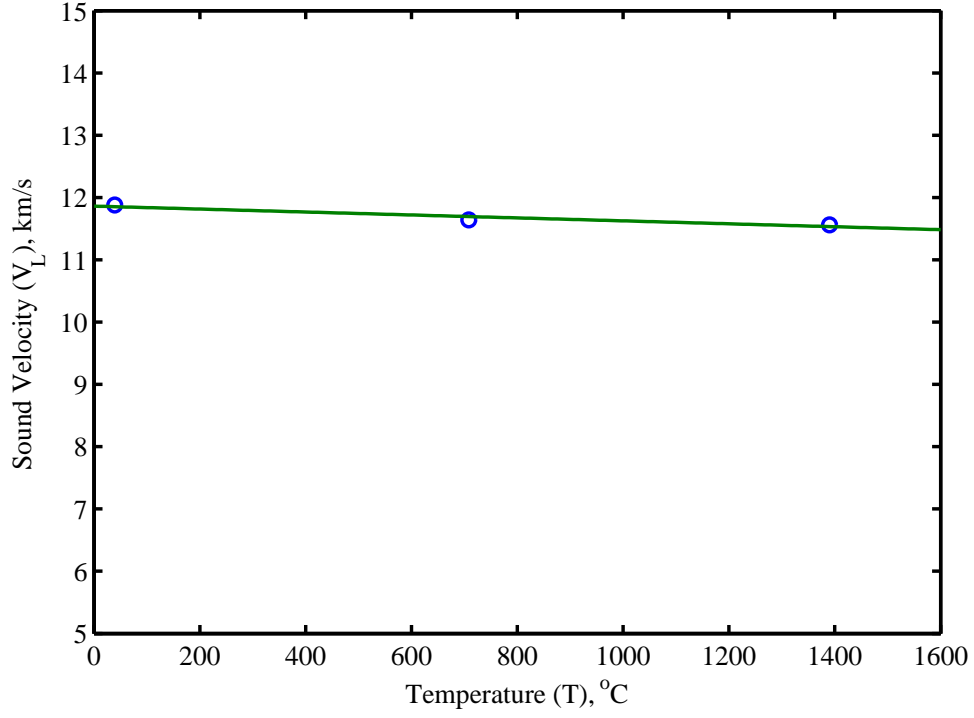


Figure 9: Sound Velocity as a function of Temperature for sintered  $\alpha$ -SiC (Longitudinal Mode) [7, 6, 8, 4]

The sound velocity ( $V_L$ , Km/s) as a function of temperature ( $T$ , °C) for sintered  $\alpha$ -SiC (Longitudinal Mode) as shown in Figure (9) can be described by the equation:

$$V_L = -2.365 \times 10^{-4}T + 11.862 \quad (10)$$

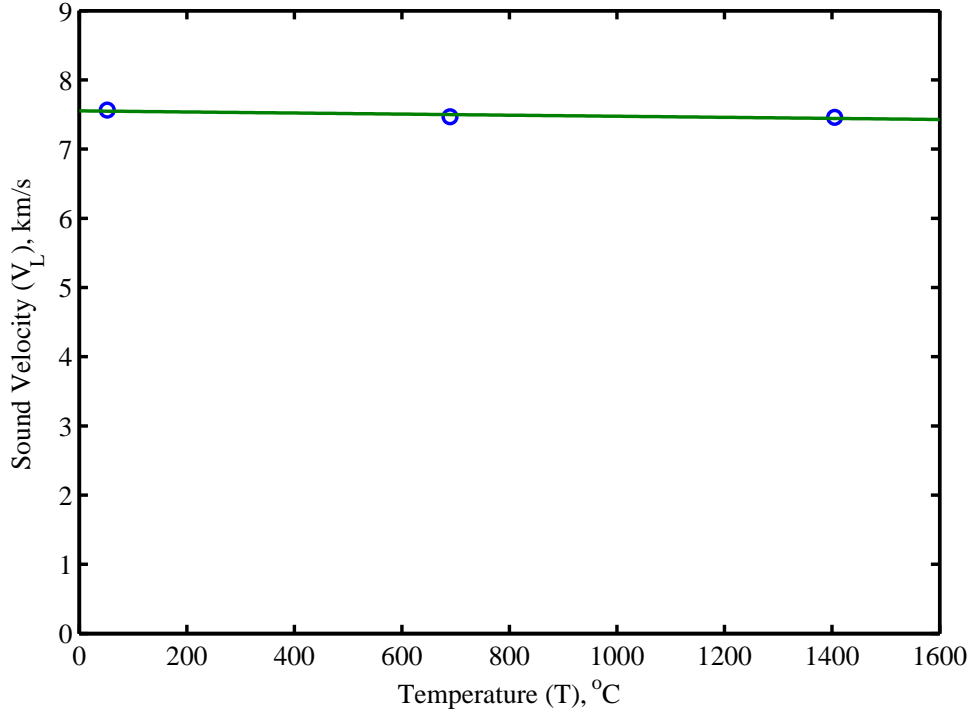


Figure 10: Sound Velocity as a function of Temperature for sintered  $\alpha$ -SiC (Shear Mode) [7, 6, 8, 4]

The sound velocity ( $V_L$ , Km/s) as a function of temperature ( $T$ , °C) for sintered  $\alpha$ -SiC (Shear Mode) as shown in Figure (10) can be described by the linear equation:

$$V_S = -7.765 \times 10^{-5}T + 7.552 \quad (11)$$

Sintered SiC is a ceramic material, and as such, the mechanical properties have significant statistical scatter as a result of the existence of microscopic cracks. While the temperature dependence of the flextural strength is shown in Figure 11, the dependence of the tensile strength on temperature is displayed in Figure 12. The increase in strength at higher temperatures is somewhat unusual, but may be attributed to the healing of microscopic cracks by the formation of a silica layer tending to their closure. Figure 13 shows the dependence of the Weibull modulus on temperature. It is clear that the data scatter does not allow a trend to be established, and hence the recommended value of the Weibull modulus is 11. On the other hand, Vickers indentation hardness shows a significant decline with temperature, as shown in Figure 14. Finally, the fracture toughness of sintered  $\alpha$ -SiC is in the range of 2.5 - 4 MPa  $\sqrt{m}$ , and can be described by a slight monotonic decrease with temperature, as shown in the figure.

## 2.3 Strength and Related Properties

Silicon carbide is a very stiff material, and retains its stiffness to very high temperatures. Let's denote the elastic constraints as follows:

E = elastic (Young's) modulus, G = shear modulus, K = bulk modulus,  $\nu$  = Poisson ratio, and  $\rho$  = density

The usual relationships between those properties should be observed, namely

$$G = \frac{E}{2(1 + \nu)} \quad (12)$$

$$K = \frac{E}{3(1 - 2\nu)} \quad (13)$$

In addition they are also related to the shear ( $V_S$ ) and longitudinal ( $V_L$ ) sound velocities as:

$$G = \rho V_S^2 \quad (14)$$

$$K = \rho[V_L^2 - (4/3)V_S^2] \quad (15)$$

Sound velocities are generally determined by ultrasonic and resonant techniques. The temperature dependences of the bulk, (K), elastic (E), and shear modulus (G) for sintered  $\alpha$ -SiC are shown in Figure 5, 6, and 7, respectively. Also, the dependence of Poisson's ratio on temperature is given in figure 8. The temperature dependencies of the longitudinal ( $V_L$ ) and shear ( $V_S$ ) sound velocities in SiC is shown in Figures 9 and 10, respectively.

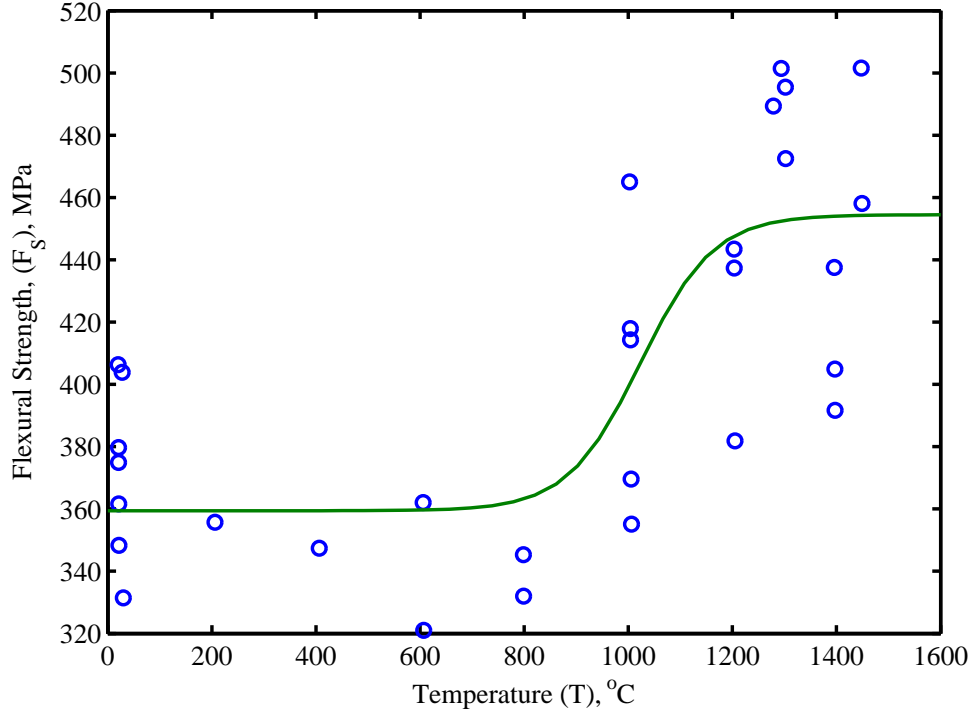


Figure 11: The flexural strength of sintered  $\alpha$ -SiC in four-point and three-point bend. Data points obtained from references [5, 6, 9, 10, 11, 12]

The flexural strength ( $F_s$ , MPa) of sintered  $\alpha$ -SiC as a function of temperature ( $T$ , °C) in four point and three point bend as shown in Figure (11) is given by:

$$F_s(MPa) = 359.42 + \frac{95.06}{(1 + 2.159 \times 10^6 \exp(-1.42 \times 10^{-2}T))} \quad (16)$$

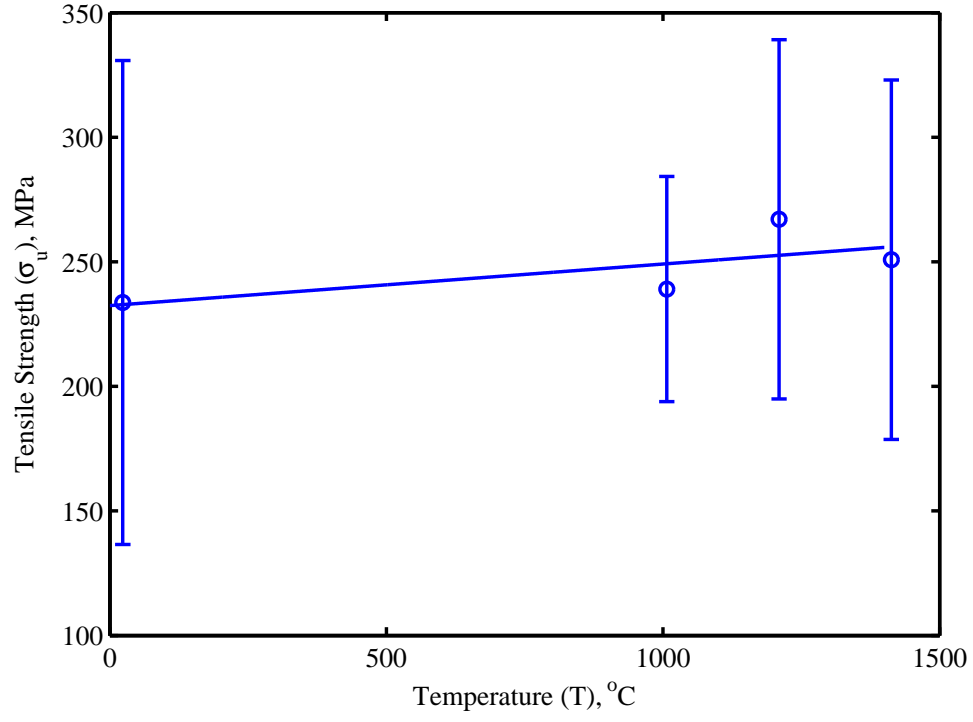


Figure 12: The tensile strength of sintered  $\alpha$ -SiC. [5, 6, 9, 10, 11, 12]

The tensile strength ( $\sigma_u$ , MPa) of sintered  $\alpha$ -SiC as a function of temperature ( $T$ , °C) as shown in Figure (12) can be described by the linear equation:

$$\sigma_u = 1.668T + 2.324 \quad (17)$$



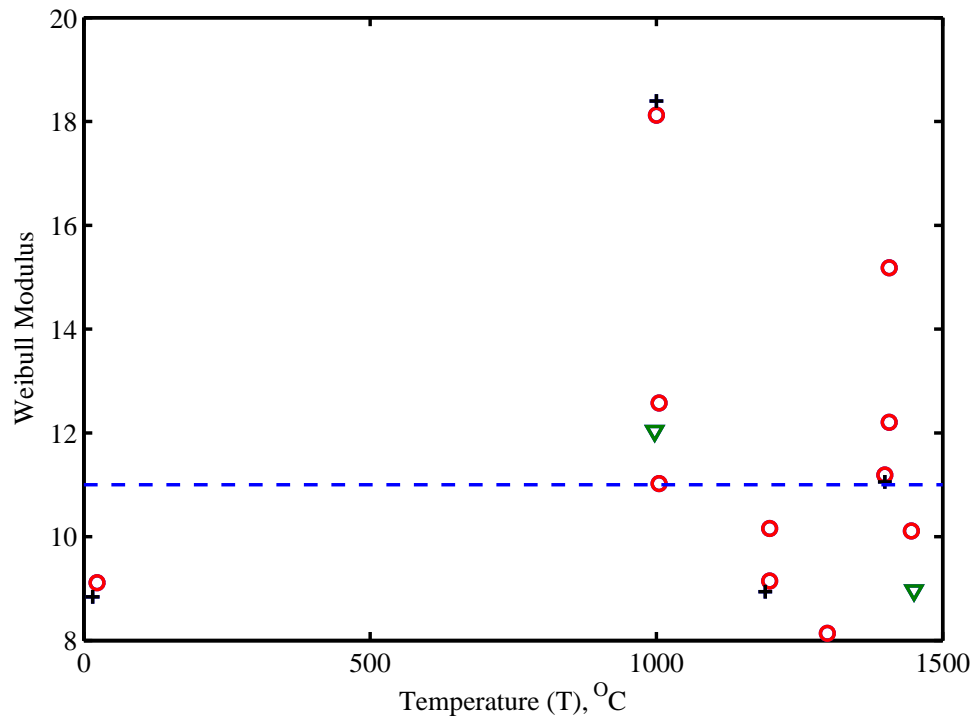


Figure 13: In the range of 0 - 1500 degrees Celsius the data are not sufficient to establish a temperature dependent trend; therefore the Weibull modulus can best be expressed as an average value of 11. [5, 6, 9, 10, 11, 12]

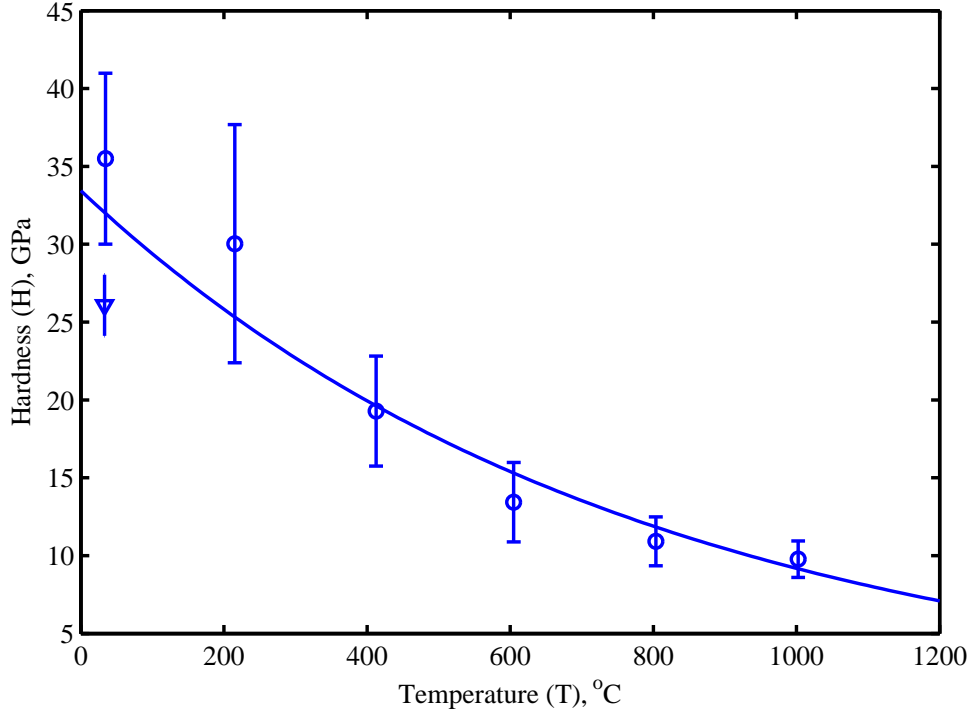


Figure 14: Vickers Indentation hardness as a function of temperature: 1000g =  $\circ$ , 500g =  $\nabla$ . [5, 6, 9, 10, 11, 12]

The Vickers hardness ( $H$ , GPa) of sintered  $\alpha$ -SiC as a function of temperature ( $T$ , °C) as shown in Figure (14) can be described by the equation:

$$H(GPa) = 33.441 \times e^{-1.292 \times 10^{-3} T} \quad (18)$$

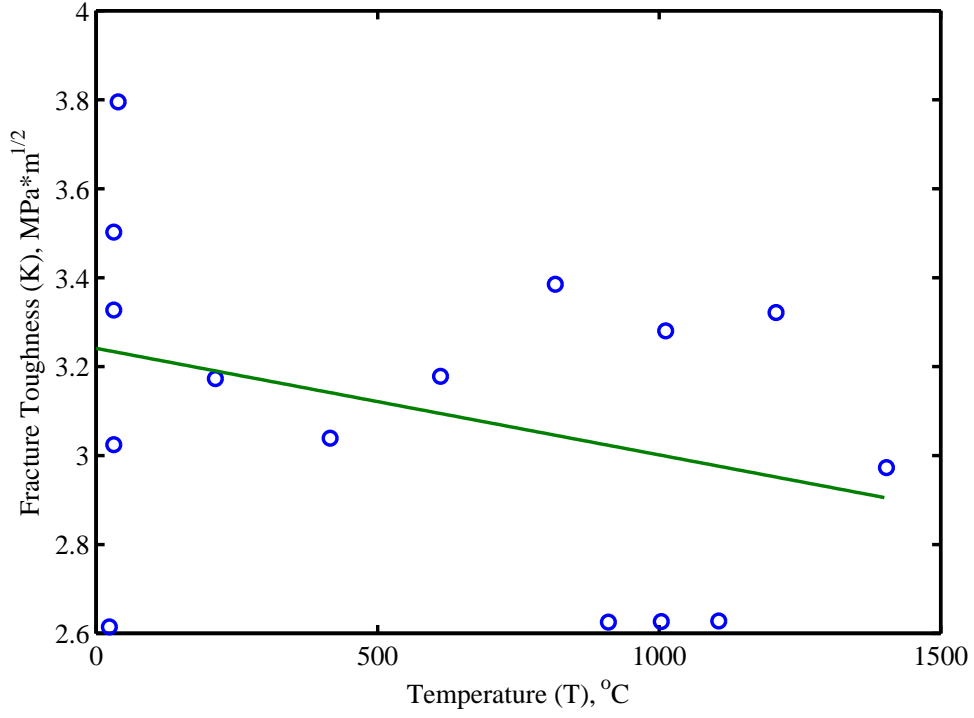


Figure 15: The fracture toughness of sintered  $\alpha$ -SiC by surface crack in flexure methods. [7, 8, 10, 13, 14, 15, 16, 17, 18, 19]

The fracture toughness ( $K_c$ , MPa  $\sqrt{m}$ ) of sintered  $\alpha$ -SiC as a function of temperature (T, °C) by surface cracks in flexure methods as shown in Figure (15) can be described by the equation:

$$K = -2.397 \times 10^{-4}T + 3.241 \quad (19)$$

## 2.4 Creep Characteristics

When subjected to stress at high temperatures,  $\alpha$ -SiC undergoes creep deformation that is dependant on the applied stress. Creep mechanisms of  $\alpha$ -SiC are not clearly determined, but because of the nearly linear stress dependence, creep deformation may be driven by diffusion processes. In Figures 16 through 21, we show the temperature and stress dependence of the creep rate in tension, flexture and compression. The creep rate ( $\dot{\epsilon}$ ,  $10^{-9}s^{-1}$ ) of sintered  $\alpha$ -SiC under compression as a function of temperature (T,  $^{\circ}C$ ) as shown in Figure 16 and Figure (21) with the curves obtained from

$$d\epsilon/dt = A\sigma^n e^{-E_{act}/RT} \quad (20)$$

with  $A = 7.35s^{-1}MPa^{-1.36}$ ,  $n = 1.36$  and  $E_{act} = 442$  kJ/mol for  $T \leq 1600^{\circ}C$ ; and  $A = 4.5 \times 10^{14}s^{-1}MPa^{-1.32}$ ,  $n = 1.32$  and  $E_{act} = 944$ kJ/mol for  $T > 1600^{\circ}C$ .

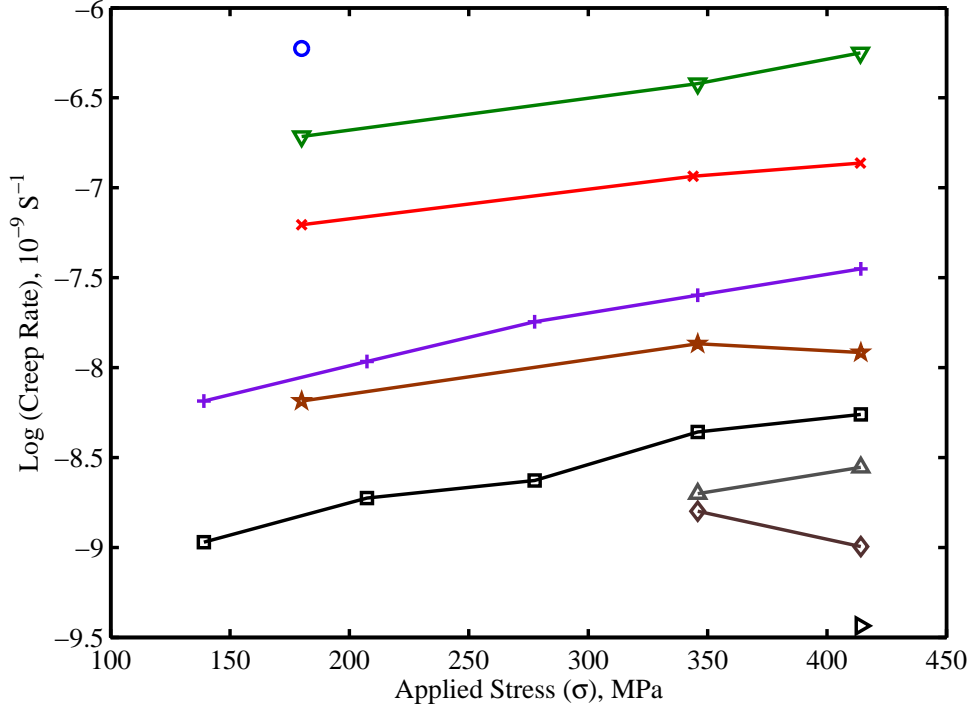


Figure 16: The creep rate of sintered  $\alpha$ -SiC in compression. [20] o = 1800  $^{\circ}C$ ,  $\nabla$  = 1750  $^{\circ}C$ ,  $\times$  = 1700  $^{\circ}C$ ,  $+$  = 1650  $^{\circ}C$ ,  $\square$  = 1600  $^{\circ}C$ ,  $\bullet$  = 1550  $^{\circ}C$ ,  $\blacktriangleright$  = 1500  $^{\circ}C$ ,  $\blacktriangleleft$  = 1450  $^{\circ}C$ ,  $\triangle$  = 1400  $^{\circ}C$ .

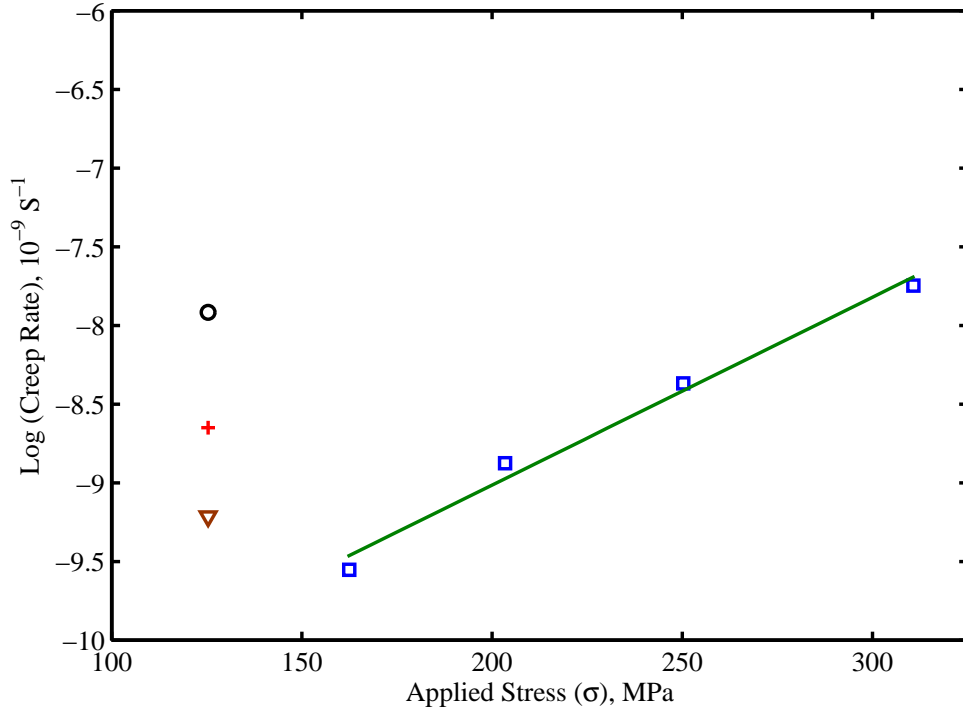


Figure 17: The creep rate of sintered  $\alpha$ -SiC in Tension and Flexure. [21, 22] o = 1525 °C in Tension, + = 1500 °C in Tension,  $\nabla$  = 1475 °C in Tension, and  $\square$  = 1450 °C in Flexure.

For sintered  $\alpha$ -SiC in Tension at 1450 °C the creep rate can be described by the linear equation;

$$\log\left[\frac{d\epsilon}{dt}\right] = 1.194 \times 10^{-2}\sigma - 11.403 \quad (21)$$

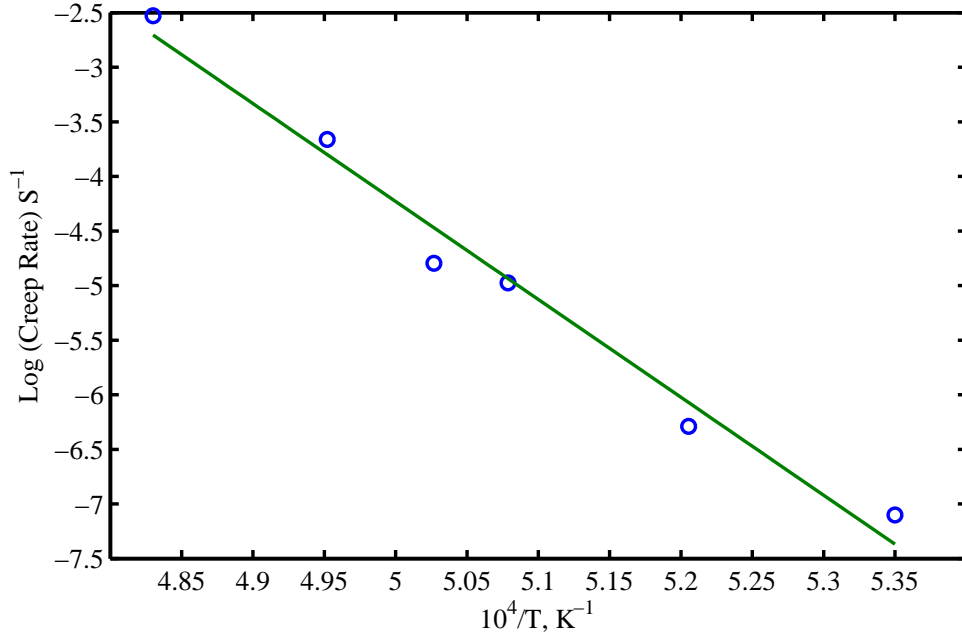


Figure 18: Arrhenius type plot of the creep rate at 179MPa Compression. [21, 22]

The creep rate of of sintered  $\alpha$ -SiC at 179 MPa while in compression can be described by the generated equation:

$$\log\left[\frac{d\epsilon}{dt}\right] = \frac{-8.968 \times 10^4}{T} + 40.61 \quad (22)$$

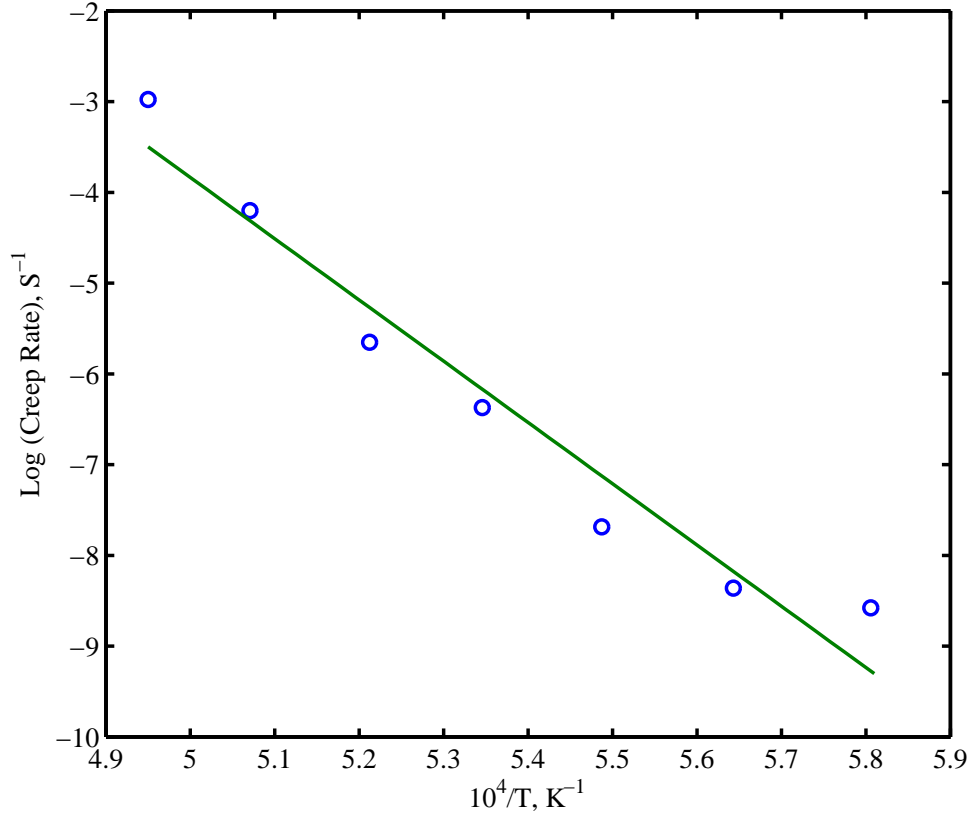


Figure 19: Arrhenius type plot of the creep rate at 345 MPa Compression. [21, 22]

The creep rate of sintered  $\alpha$ -SiC at 345 MPa while in compression can be described by the generated equation:

$$\log\left[\frac{d\epsilon}{dt}\right] = \frac{-6.75 \times 10^4}{T} + 29.915 \quad (23)$$

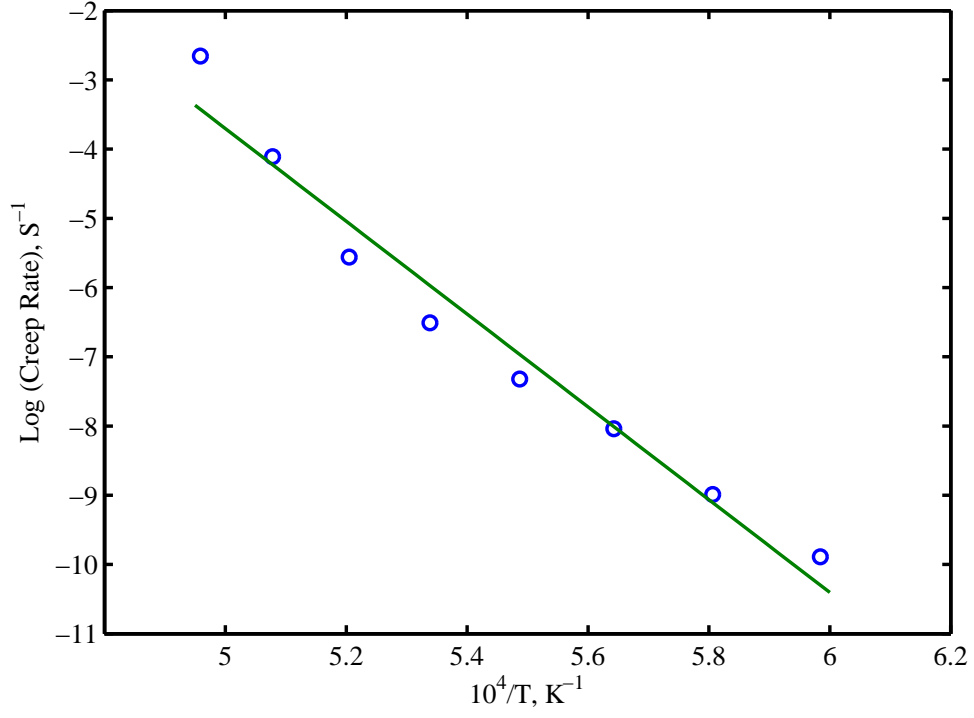


Figure 20: Arrhenius type plot of the creep rate at 414 MPa Compression. [21, 22]

The creep rate of sintered  $\alpha$ -SiC at 414 MPa while in compression can be described by the generated equation:

$$\log\left[\frac{d\epsilon}{dt}\right] = \frac{-6.703 \times 10^4}{T} + 29.815 \quad (24)$$



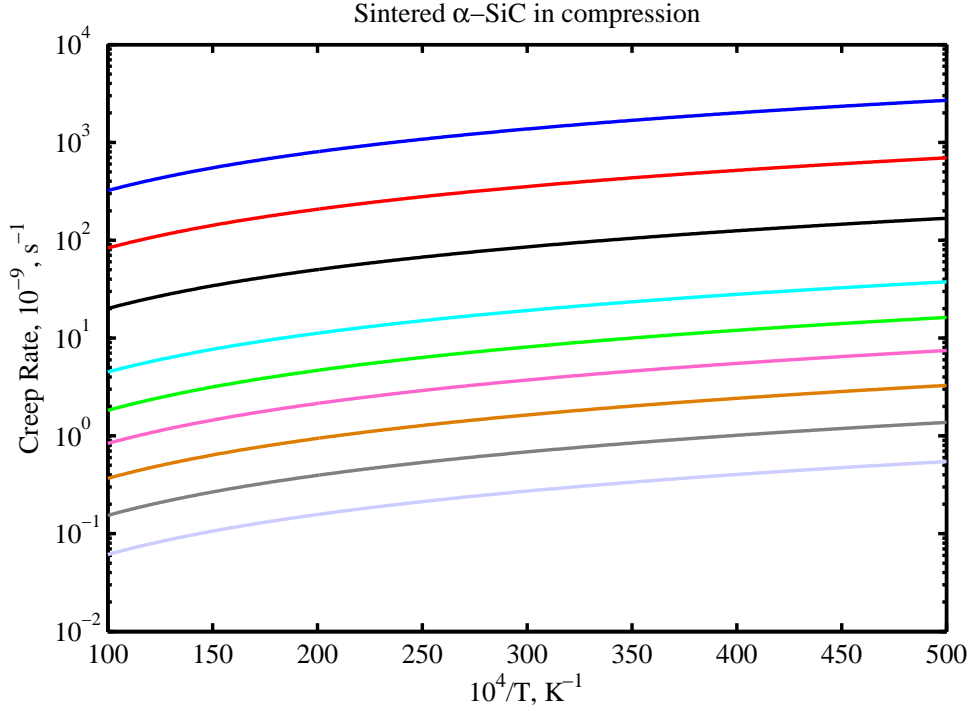


Figure 21: The blue line is for 1800 C, the red line is for 1750 C, the black line is for 1700 C, the turquoise line is for 1650 C, the green line is for 1600 C, the pink line is for 1550 C, the brown line is for 1500 C, the dark grey line is for 1450 C, and the light grey line is for 1400 C. [21, 22]

## 2.5 Tribological Characteristics

The key tribological properties are the coefficient of friction (COF) and the wear coefficient ( $K_w$ ). Considerable scatter in the data is observed for both measures of the tribological characteristic of  $\alpha$ -SiC as a result of the variabilities in test conditions and measurement methods. The wear coefficient ( $K_w$ ) is a dimensionless parameter that describes the wear rate. It is given by:

$$K_w = \frac{V_w \times H}{F_n \times D_s} \quad (25)$$

where  $V_w$  is the wear volume,  $H$  is the hardness,  $F_n$  is the normal force and  $D_s$  is the sliding distance. The temperature dependences of COF and  $K_w$  are shown in Figures 22 and 23, respectively.

A linear fit of the Coefficient of Friction ( $\mu$ ) vs. Temperature ( $T$ , °C) for Figure (22) is given by:

$$\mu = -3.224 \times 10^{-4}T + 0.665 \quad (26)$$

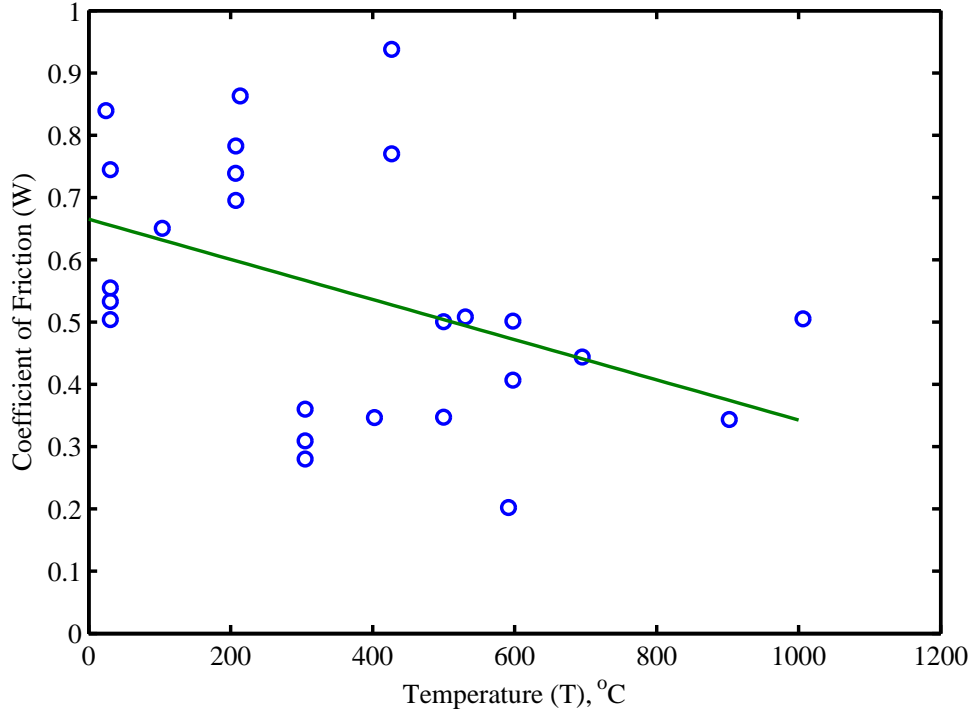


Figure 22: Wear of sintered  $\alpha$ -SiC when the load is  $\leq 10$  N, and the sliding speed is  $\leq 0.25$  m/s, due to friction . [23, 24, 25, 26, 27, 28, 29, 30, 31]

A linear fit of the Wear Coefficient ( $W$ ) vs Temperature ( $T$ , °C) for Figure (23) is given by:

$$W = 9.317T + 2.084 \quad (27)$$

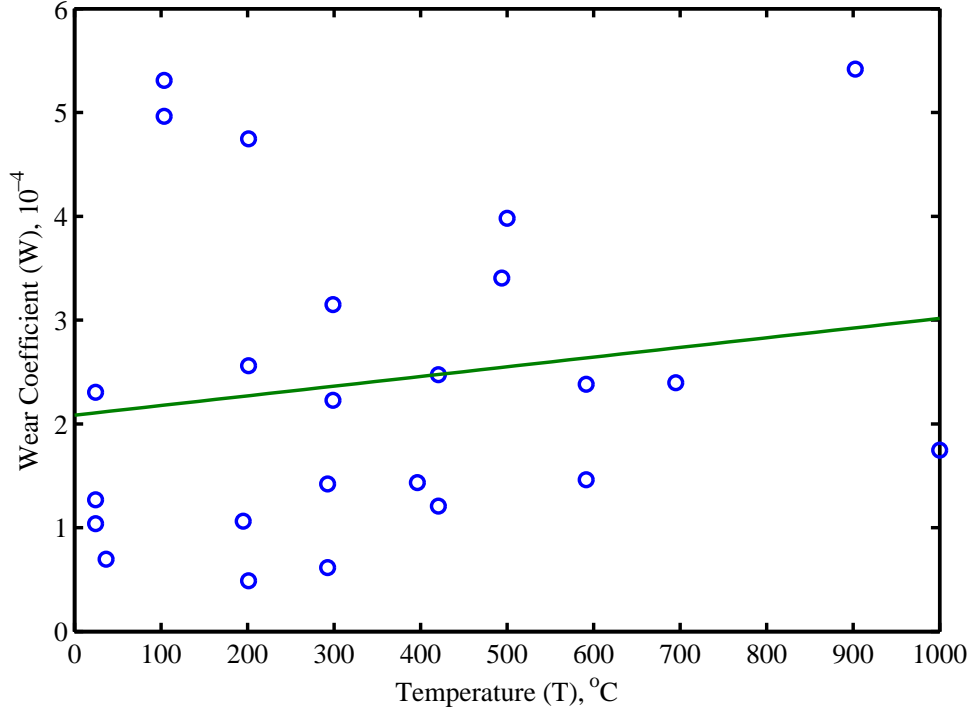


Figure 23: Wear of sintered  $\alpha$ -SiC when the load is  $\leq 10N$ , and the sliding speed is  $\leq 0.25m/s$ . [23, 24, 25, 26, 27, 28, 29, 30, 31]

## 2.6 Thermal Properties

Thermal properties of sintered  $\alpha$ -SiC include the specific heat,  $C_P$ , the thermal conductivity,  $k$ , and the thermal diffusivity,  $D$ . These three parameters are related by:

$$k = \rho \times C_P \times D \quad (28)$$

where  $\rho$  is the density. The temperature dependence of  $C_P$  ( $JKg^{-1}K^{-1}$ ) is shown in Figure 24, while those for  $k$  ( $Wm^{-1}K^{-1}$ ) are shown in Figures 26 and 27. In addition, the coefficient of thermal expansion is shown in Figure 28 as a function of temperature. It is noted that thermal conductivity measurements for reaction-sintered SiC obtained from Carborundum Company (Figure 27) are almost twice as large at low temperatures as the values obtained for sintered  $\alpha$ -SiC in Figure 26. The temperature dependence of the thermal diffusivity is shown in Figure 27.

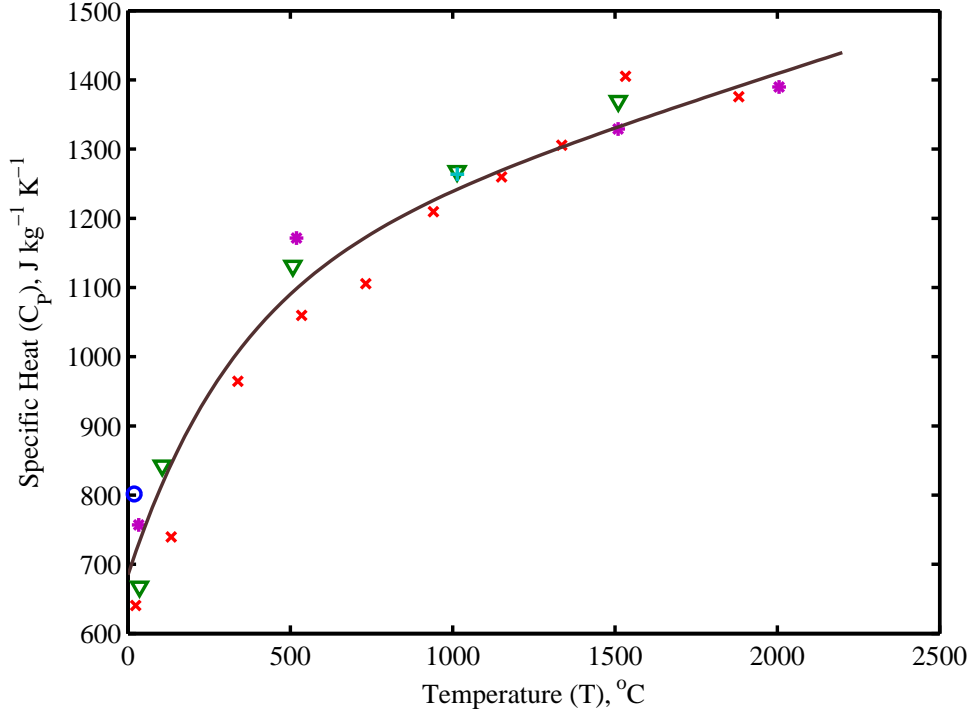


Figure 24: The specific heat of a variety of sintered  $\alpha$ -SiC materials. o is Sintered  $\alpha$ -SiC with  $B_4C$ ,  $\nabla$  is Sintered  $\alpha$ -SiC with  $Al_2O_3$ ,  $\times$  is typical Sintered  $\alpha$ -SiC,  $+$  is Sintered  $\alpha$ -SiC, and  $*$  SiC (solid). The curve was generated using Munro's interpolation formula, in which he concluded that the specific heat of sintered  $\alpha$ -SiC is not sensitive to variations in its minor constituents. [8, 30, 31, 32, 33, 34, 35, 36, 37]

The specific heat of sintered  $\alpha$ -SiC is shown in Figure (24) is given by the interpolation formula: [1]

$$C_p = 1110 + 0.15T - 425e^{-0.004T} \quad (29)$$

where  $C_p$  ( $J\ kg^{-1}\ K^{-1}$ ) is the specific heat and  $T$  is temperature in Celsius.

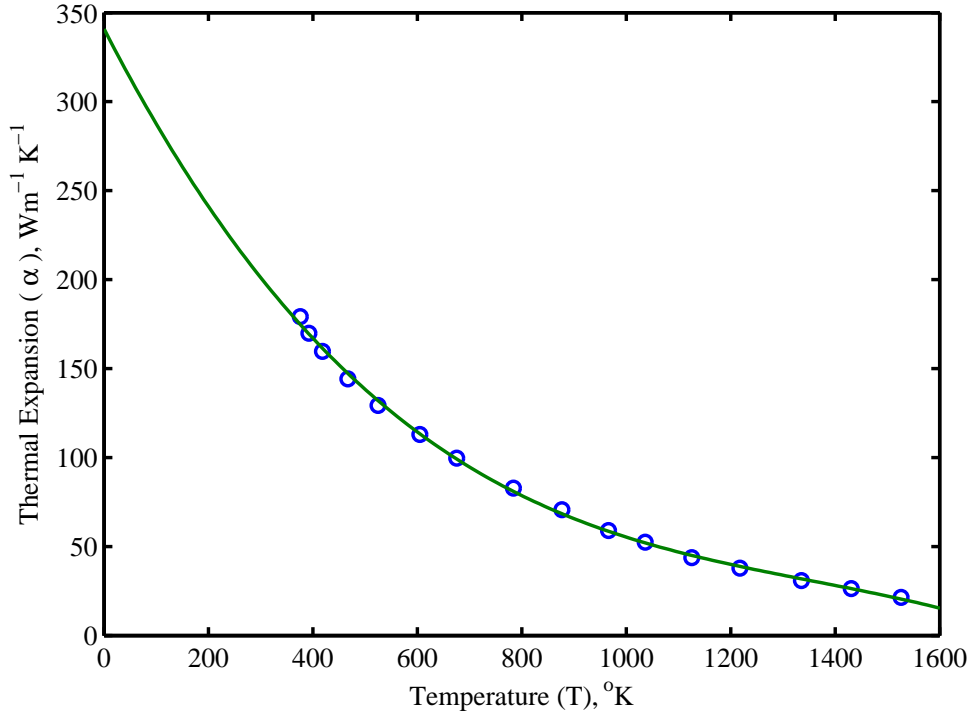


Figure 25: This Curve, for reaction sintered SiC, is based on data from the following processes: Reaction sintered SiC (Carborundum Company KT grade); specimen 1/2 inch [1.27 cm] diameter and 3-inch [7.62 cm] length; nominally 96.5 percent dense; axial heat flow, comparative method, argon atmosphere;  $\pm 10$  percent error. The data agree within 10 percent of values reported in Carborundum Company literature, references 310 and 154, which employed an axial-heat-flow, comparative method with error of about  $\pm 4$  percent. Reaction sintered SiC; 99 percent dense; approximately 10 volume percent free Si; thermal conductivity values calculated from thermal diffusivity measurements

The representative curve for the thermal expansion coefficient of SiC materials as a function of temperature as shown in 25 is represented by

$$\alpha = 4.5816 \times 10^{-4} T \quad (30)$$

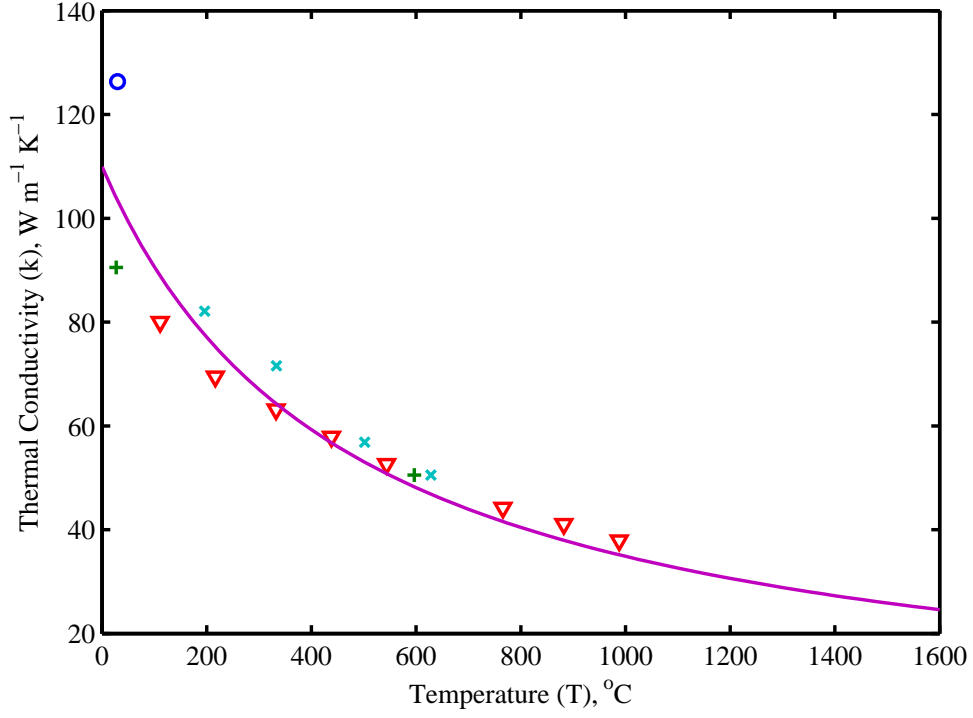


Figure 26: Thermal conductivity for sintered  $\alpha$ -SiC.  $\nabla$  represents NC-203,  $\times$  represents pre-Hexoloy SA,  $\circ$  represents Hexoloy SA, and the  $+$  sign represents yet another alloy of pre-Hexoloy SA. [8, 30, 31, 32, 33, 34, 35, 36, 37]

The thermal conductivity of sintered  $\alpha$ -SiC as shown in Figure (26) is given by the interpolation formula: [1]

$$k = \frac{52000 \times e^{-1.24 \times 10^{-5} T}}{T + 437} \quad (31)$$

where  $k$  is the thermal conductivity ( $\text{W m}^{-1} \text{K}^{-1}$ ) and  $T$  is temperature in Celsius.

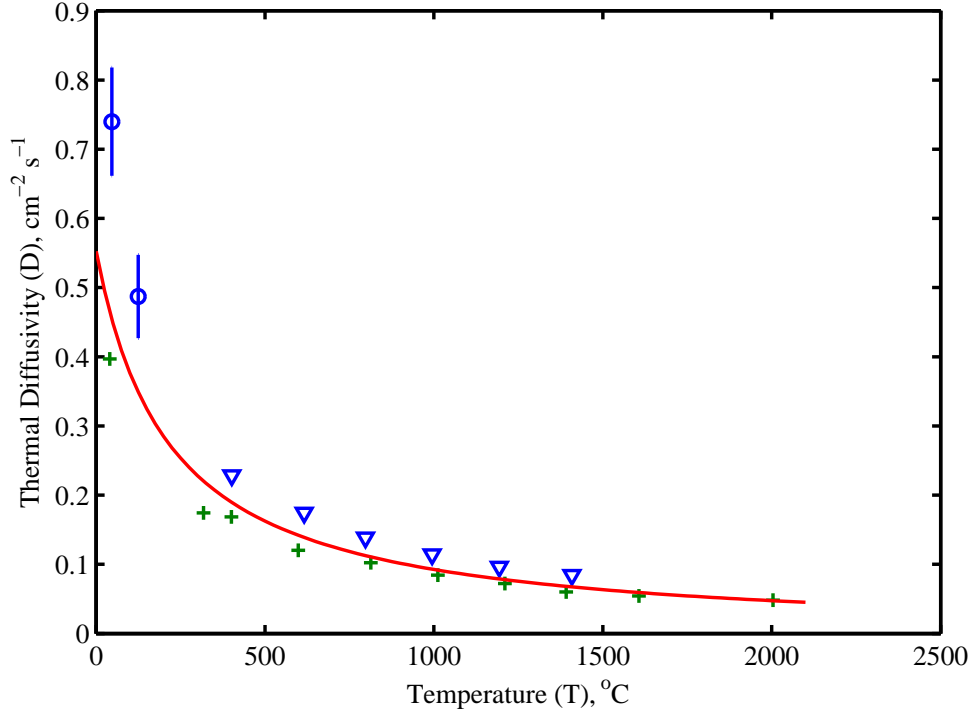


Figure 27: Thermal diffusivity for sintered  $\alpha$ -SiC. [8, 30, 31, 32, 33, 34, 35, 36, 37]

The thermal diffusivity as shown in Figure (27) is given by the interpolation formula:  
[1]

$$D = \frac{121 \times e^{-6.98 \times 10^{-5} T}}{T + 219} \quad (32)$$

where D is the thermal diffusivity ( $\text{cm}^2 \text{s}^{-1}$ ) and T is temperature in Celsius.

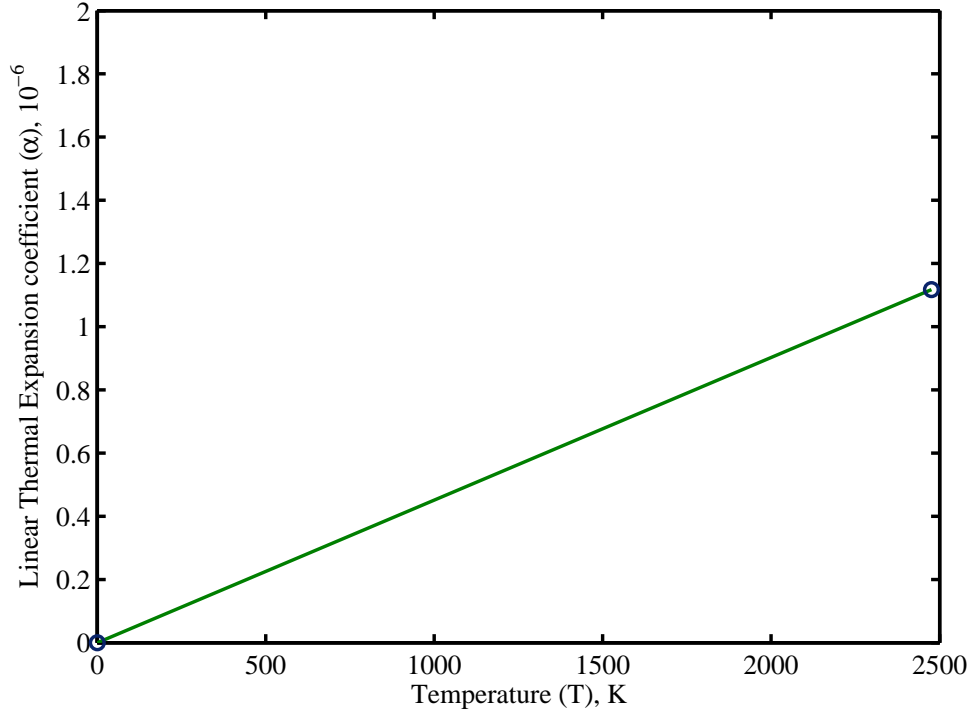


Figure 28: Representative curve for the thermal expansion of SiC materials as a function of temperature was derived from the information in the following references. The variation of reported values is about  $\pm 0.05$  percent expansion at 1000 F (811 K), and  $\pm 0.10$  percent expansion between 1000 and 4000 F (811 to 2477 K);  $\alpha = 2.4 \times 10^{-6} F^{-1} [4.3 \times 10^{-6} K^{-1}]$  75 to 1600 F [297 to 1144 K] and  $3.0 \times 10^{-6} F^{-1} [5.4 \times 10^{-6} K^{-1}]$  1000 to 4000 F [811 to 2477 K]



### 3 Properties of Foam-SiC

#### 3.1 Manufacturing

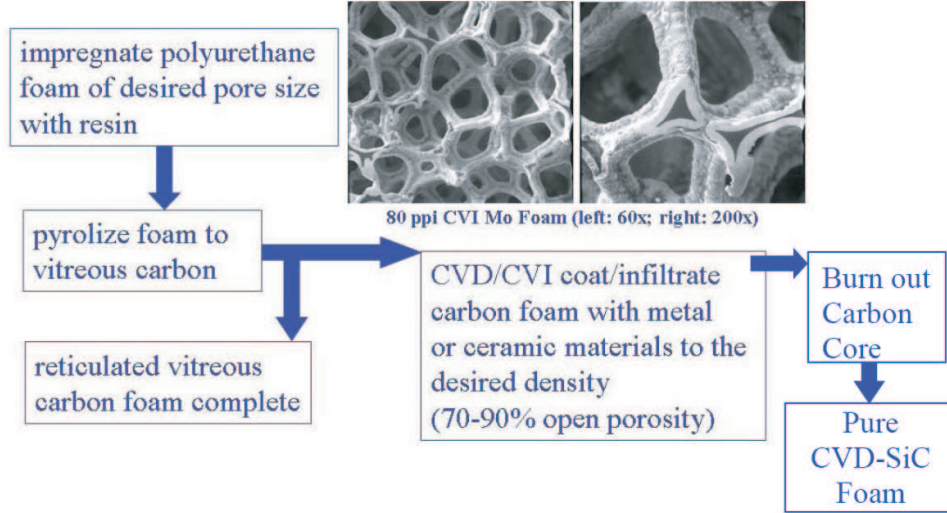


Figure 29: Process flow chart for ceramic foam fabrication.

In the CVI process, reactant gases containing the desired coating material(s) are flowed through a heated substrate, in this case the RVC foam. The compound(s) within the reactant gas stream react near the heated foam ligament surfaces to form a continuous, uniform coating over the entire substrate. SiC is deposited via the 1200-1400°C hydrogen reduction of methyltrichlorosilane ( $CH_3SiCl_3$ , or MTS), by the following reaction:



Typical deposition rates of 0.01 in/hr are achievable. The benefits of CVD/CVI include the ability to produce deposits of controlled density, thickness, orientation, and composition. Impurity levels are typically less than 0.1%, with densities of 99.9% . In addition, CVD/CVI coatings exhibit the greatest throwing power, or ability to uniformly deposit materials onto/into intricately shaped or textured substrates, thus allowing fabrication of near-net shape parts with geometries that cannot be produced through conventional machining. The greatest benefit of CVD/CVI is probably the fact that numerous materials can be deposited at temperatures that are one-half to one-tenth the melting point of the coating material itself.

Foam fabrication starts with commercially available reticulated polyurethane foams, which is converted to vitreous carbon. the reticulated vitreous carbon (RVC) foam, having

the cell size and structure desired for the final foam component, is then used as a skeletal structure to make a broad variety of metal and ceramic foams. The same type of gaseous precursor compound used in CVD is then infiltrated into the heated RVC foam substrate, where it decomposes at the heated foam ligament surfaces to grow a deposit of the desired hollow ligaments. Foam pore sizes (measured in pores per linear inch, or ppi) are available from 3-100. Fabrication of foams with an effective pore size greater than 100 ppi has also been demonstrated by Ultramet by squeezing the polyurethane foam in one, two, or three dimensions during the conversion to vitreous carbon.

The process is performed within a quartz or fused silica reaction chamber, under vacuum, similar to that shown schematically in Figure 30. The key processing parameters that must be optimized for uniform, economical foam fabrication are reactant concentration and flow rate, substrate temperature, and minimization of the number of infiltration cycles.

The level of SiC infiltration, and resultant change in foam density, is used to optimize the properties for the application. Removal of the low-strength, 3vol% vitreous carbon skeleton has no effect on mechanical properties or thermal conductivity of the 10-20vol% dense SiC foam. Electrical conductivity is further reduced because the conductivity of vitreous carbon is greater than that of SiC. It is important to note that the fine-grained, fully dense coatings deposited by CVD display better stiffness and strength than do bulk materials of the same composition fabricated by powder processing. The elastic moduli of such CVD films have regularly measured up to 25% higher than those of the bulk materials. The ceramic foam is extremely well-suited for a lightweight substrate onto which very high-stiffness, fully-dense facesheet coatings may be deposited. Since the modulus of the deposited film is so much greater than that of the vitreous carbon foam skeleton, the carbon foam has no influence on the properties of the final product; it merely acts as a "locator" for the deposited films. As discussed previously, the low-strength carbon skeleton can be rapidly and completely removed through oxidation, leaving hollow ligaments. Ceramic foams made by CVI exhibit significantly greater thermal and mechanical fracture toughness than monolithic ceramics. The ligamental structure severely inhibits crack propagation. Deposition of the fully dense facesheet is performed by altering the deposition conditions such that a dense, continuous surface layer is formed. The faceplate thickness will be optimized, as well as the foam core thickness, based on the modeling work performed by DMS. Thermal and mechanical testing of development specimens will be performed, as needed, to add to the current CVD SiC foam and solid CVD SiC database in support of the DMS effort. Molten metal exposure testing of small disc specimens will be performed using the test apparatus shown in Figure Pb, which will be incorporated into an Ultramet lab. Testing will be performed in coordination with DMS consultant Dr. Neil Morley. The disc specimens will be placed in contact with a Pb-Li melt on both sides with electrical current and heat flux passed through the disk. This test will help determine the effect of melt temperature (up to 500°C), facesheet thickness, and foam density on the electrical and thermal properties, as well as providing an evaluation of potential failure mechanisms. Of particular interest is PbLi wetting and ingress into surface microcracks. Intentionally microcracked samples will

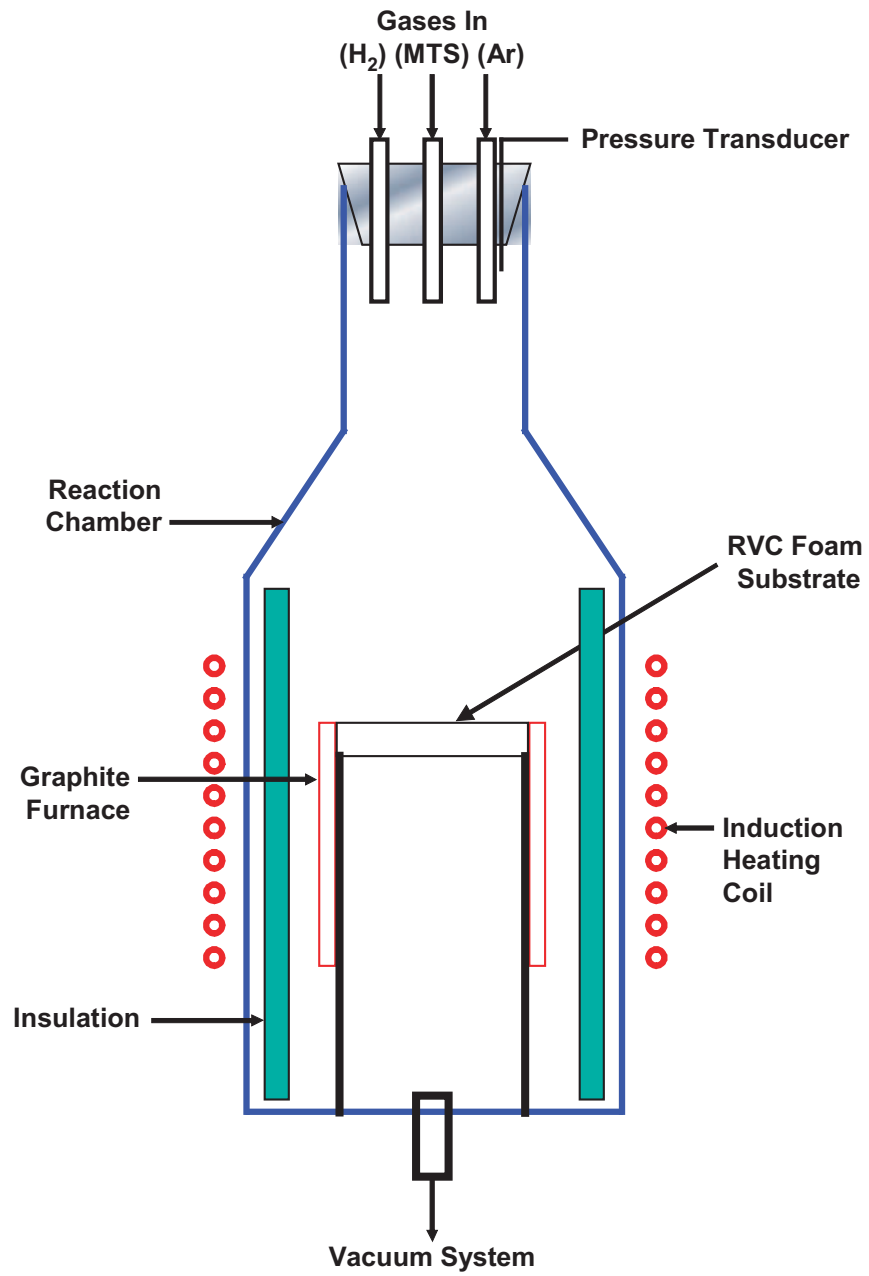


Figure 30: Schematic of typical CVD/CVI reactor for foam infiltration.

be exposed to high temperature PbLi to study wetting and ingress resistance. Surface and cross-sectional evaluation of the materials produced will be performed by optical and scanning electron microscopy (SEM). Elemental analysis will be performed through energy-dispersive X-ray spectroscopy (EDS), while the phases present will be determined by X-ray diffraction (XRD).

## 3.2 Thermal Properties of Foam-SiC

The thermal and mechanical properties of foam-SiC were experimentally determined by the EMTL Mechanics and structures Lab, under contract with Ultramet [38]. A total of sixteen mechanical and eight thermal tests were performed on 65 ppi and 100 ppi - 10% and 20% dense SiC-foam samples provided by Ultramet. Tests were conducted between room temperature and 1400°C. The following data analysis is based on these tests. The following test matrix was established:

Table: Test matrix for thermal and mechanical properties established by [38]

Test Type Determined	Test Temperature	Material Type	Properties
Compression	1000°C	65 PPI-10% 65 PPI-20%	Ucs, Ec Ucs, Ec
Tension	Room Temperature	65 Ppi-10% 65 Ppi-20% 100 Ppi-10% 100 Ppi-20%	Uts, Et Uts, Et Uts, Et Uts, Et
Shear, core	Room Temperature	65 Ppi-10% 65 Ppi-20% 100 Ppi-10% 100 Ppi-20%	Uss Uss Uss Uss
CTE	Room Temperature - 100°C	65 Ppi-10% 65 Ppi-20% 100 Ppi-10% 100 Ppi-20%	CTE CTE CTE CTE
Conductivity	Room Temperature - 1400°C	65 Ppi-10% 65 Ppi-20% 100 Ppi-10% 100 Ppi-20%	TC TC TC TC

Where: UCS = Ultimate compressive strength, ksi EC = Elastic compressive modulus, Msi Uts = Ultimate Tensile Strength, ksi Et = Elastic Tensile Modulus, Msi Uss = Ultimate Shear Strength, ksi CTE = Coefficient of Thermal Expansion, in/in-°C

### 3.2.1 Thermal Expansion

Thermal expansion measurements were performed by the pushrod dilatometer technique in general accordance with test Specification ASTM E-228. EMTL operates two types of dilatometers; a vitreous silica (quartz) pushrod dilatometer for the temperature range -320°F to 1800°F, and a graphite pushrod dilatometer, RT to 5000°F.

In the quartz dilatometer, the specimen is supported between members of a quartz frame and pushrod assembly. The assembly is inserted into a furnace capable of uniformly heating the specimen zone. As the specimen temperature is changed, changes

in its length dimension result in relative displacement of the quartz pushrod and frame transducer, and recorded on one scale of an X-Y plotter. Specimen temperature is sensed by thermocouple, and is recorded on the other scale. Thus a continuous record of dilation versus temperature is produced. EMTL utilizes the NIST fused silica standard reference material, SRM 739, to perform calibrations of this system. For measurement of these SiC foams, an argon gas flow was maintained during testing.

Each thermal expansion specimen was tested first in the quartz dilatometer RT to 850°C and then again to 1200°C in the graphite dilatometer. This method provides the best definition for each sample at both the low and high temperatures. Heating rates were 3°C/minute in both dilatometers.

Measurements of thermal expansion,  $\frac{\Delta L}{L}$ , as a function of temperature are shown in Figure 30 for 65 ppi-10% dense foam, 65 ppi-10% dense foam, 100 ppi- 20% dense foam and for 100 ppi-20% dense foam. The average coefficient of thermal expansion over the Room Temperature - 1400°C temperature range is indicated in figure captions. The data shows slight non-linear dependence on temperature. Therefore, a temperature dependent coefficient of thermal expansion  $\alpha$ , can be obtained by the data, and is represented in Figure.

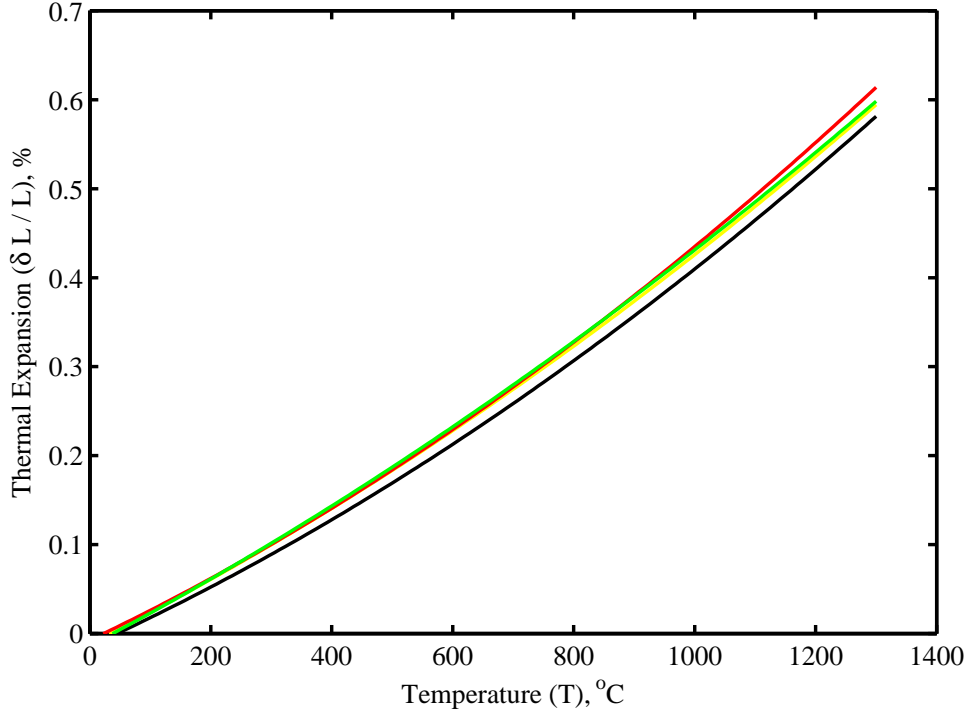


Figure 31: Ulramet Thermal Expansion data for SiC foam with  $\alpha = 4.51 \times 10^{-6}/\text{C}$ . The yellow line represents 65 ppi 10% dense foam. The black line represents 65 ppi 20% dense foam. The red line represents 100 ppi 10% dense foam. The green line represents 100 ppi 20% dense foam.

The thermal expansion (%) of 65 ppi 10% dense SiC foam as shown in Figure (31) can be represented by:

$$\frac{\delta L}{L} = 9.608 \times 10^{-8}T^2 + 3.410 \times 10^{-4}T - 1.117 \times 10^{-2} \quad (34)$$

The thermal expansion (%) of 65 ppi 20% dense SiC foam as shown in Figure (31) can be represented by:

$$\frac{\delta L}{L} = 1.14 \times 10^{-7}T^2 + 3.101 \times 10^{-4}T - 1.437 \times 10^{-2} \quad (35)$$

The thermal expansion (%) of 100 ppi 10% dense SiC foam as shown in Figure (31) can be represented by:

$$\frac{\delta L}{L} = 1.189 \times 10^{-7}T^2 + 3.235 \times 10^{-4}T - 7.527 \times 10^{-3} \quad (36)$$

The thermal expansion (%) of 100 ppi 20% dense SiC foam as shown in Figure (31) can be represented by:

$$\frac{\delta L}{L} = 8.656 \times 10^{-8}T^2 + 3.5835 \times 10^{-4}T - 1.379 \times 10^{-2} \quad (37)$$

### 3.2.2 Thermal conductivity, Diffusivity and Specific Heat

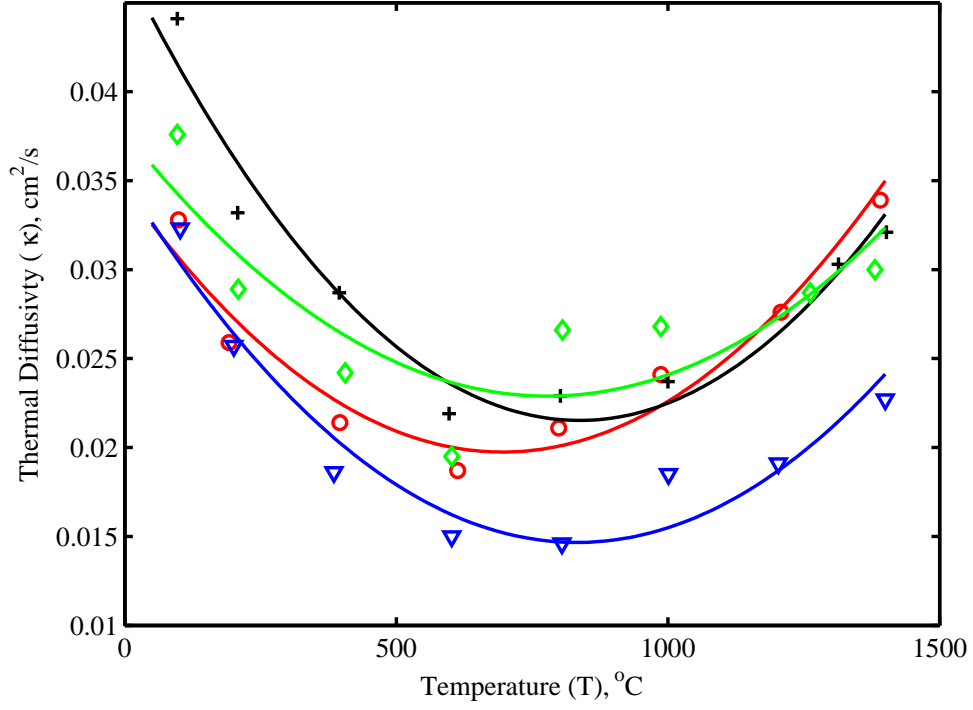


Figure 32: Ultramet thermal diffusivity data for SiC foam.

The thermal diffusivity ( $\kappa$ ) of 65 ppi 10% dense Ultramet SiC foam as a function of temperature (C) as shown in Figure (32) can be represented by:

$$\kappa = 3.071 \times 10^{-8} T^2 - 4.272 \times 10^{-5} T + 3.46 \times 10^{-2} \quad (38)$$



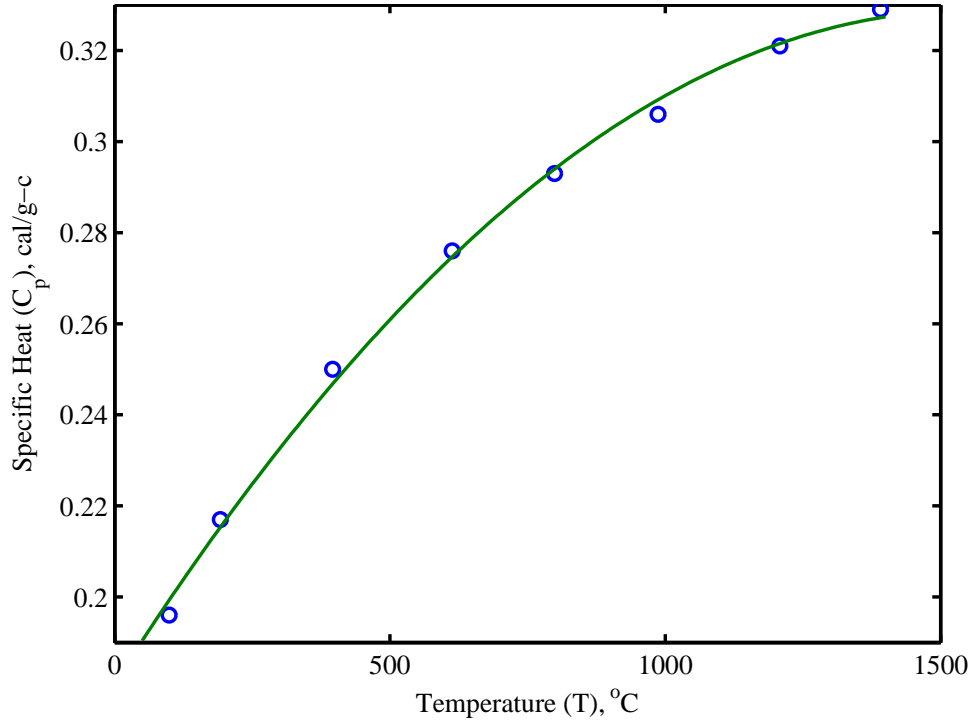


Figure 33: Ultramet specific heat data for SiC foam.

The specific heat of 65 ppi 10% dense Ultramet SiC foam as a function of temperature (C) as shown in Figure (33) can be represented by:

$$C_p = -6.128 \times 10^{-8}T^2 + 1.903 \times 10^{-4}T + 1.811 \times 10^{-1} \quad (39)$$

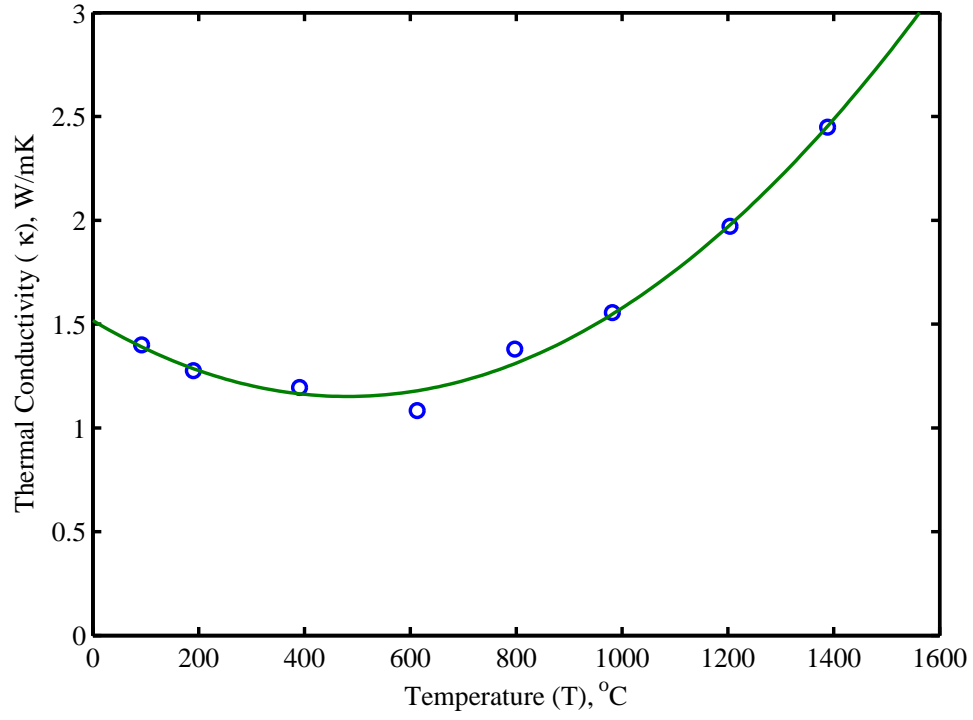


Figure 34: Ultramet SiC foam thermal conductivity data [Ultramet, 2005] for 65 ppi 10 percent dense SiC foam.

The thermal conductivity (W/mK) of SiC-Foam as a function of temperature (°C) for 65 ppi 10% dense SiC foam, as shown in Figure (34) is represented by:

$$k = 1.582 \exp(-6T^2) - 1.522 \exp(-6T) + 1.517 \quad (40)$$

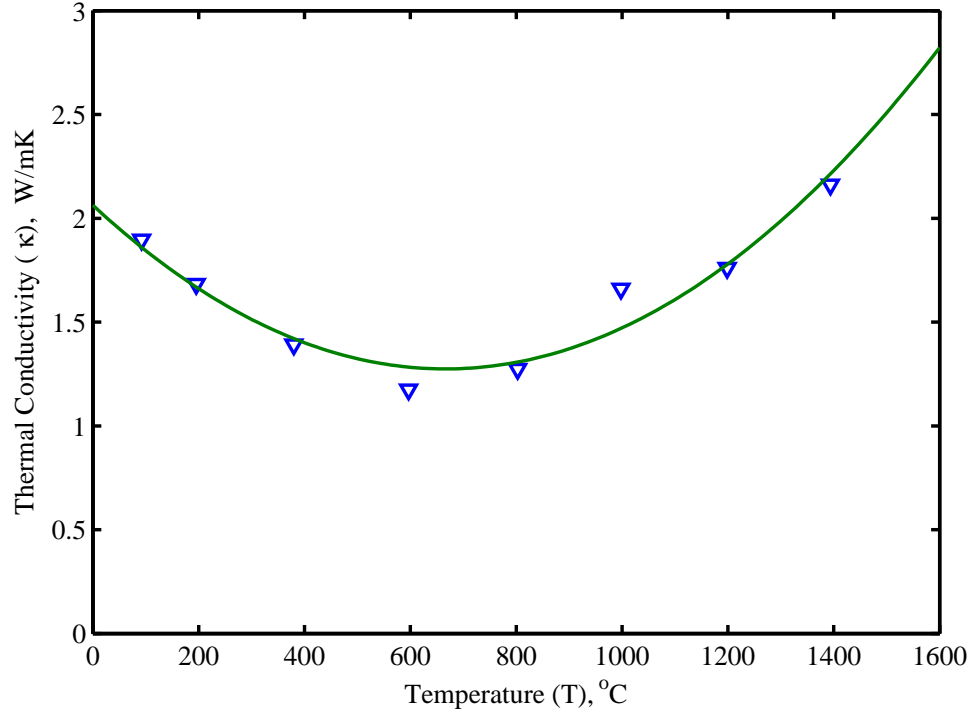


Figure 35: Ultramet SiC foam thermal conductivity data [Ultramet, 2005] for 65 ppi 20 percent dense SiC foam.

The thermal conductivity (W/mK) of SiC-Foam as a function of temperature (°C) for 65 ppi 20% dense SiC foam, as shown in Figure (35) is represented by:

$$k = 1.776 \times 10^{-6}T^2 - 2.367 \times 10^{-3}T + 2.063 \quad (41)$$

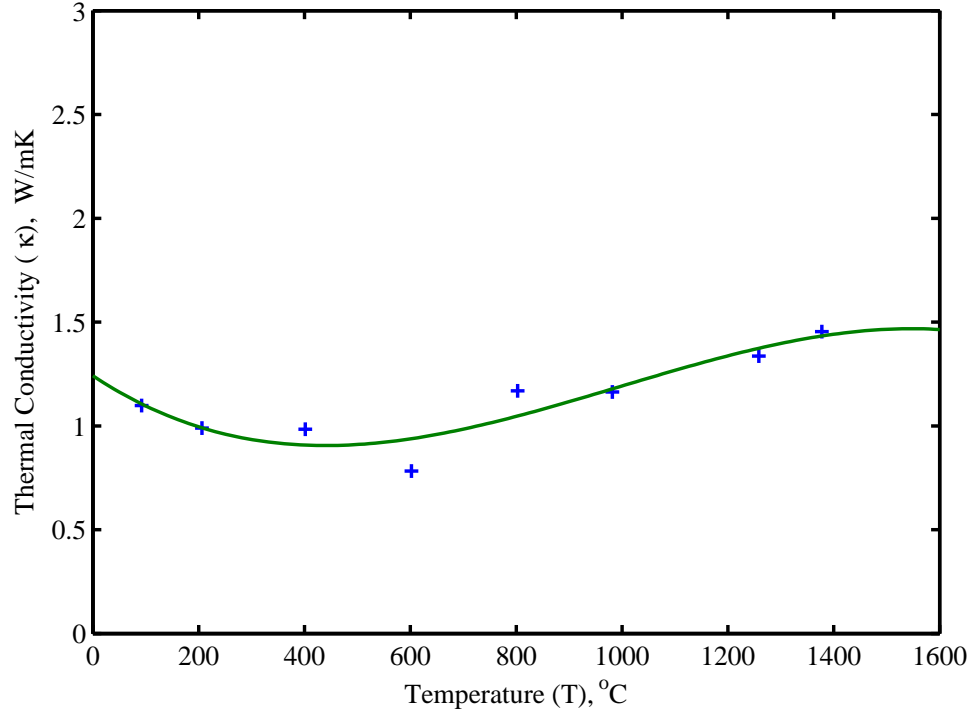


Figure 36: Ultramet SiC foam thermal conductivity data [Ultramet, 2005] for 100 ppi 10 percent dense SiC foam.

The thermal conductivity (W/mK) of SiC-Foam as a function of temperature (°C) for 65 ppi 10% dense SiC foam, as shown in Figure (36) is represented by:

$$k = -8.296 \times 10^{-10}T^3 + 2.471 \times 10^{-6}T^2 - 1.69 \times 10^{-3}T + 1.242 \quad (42)$$

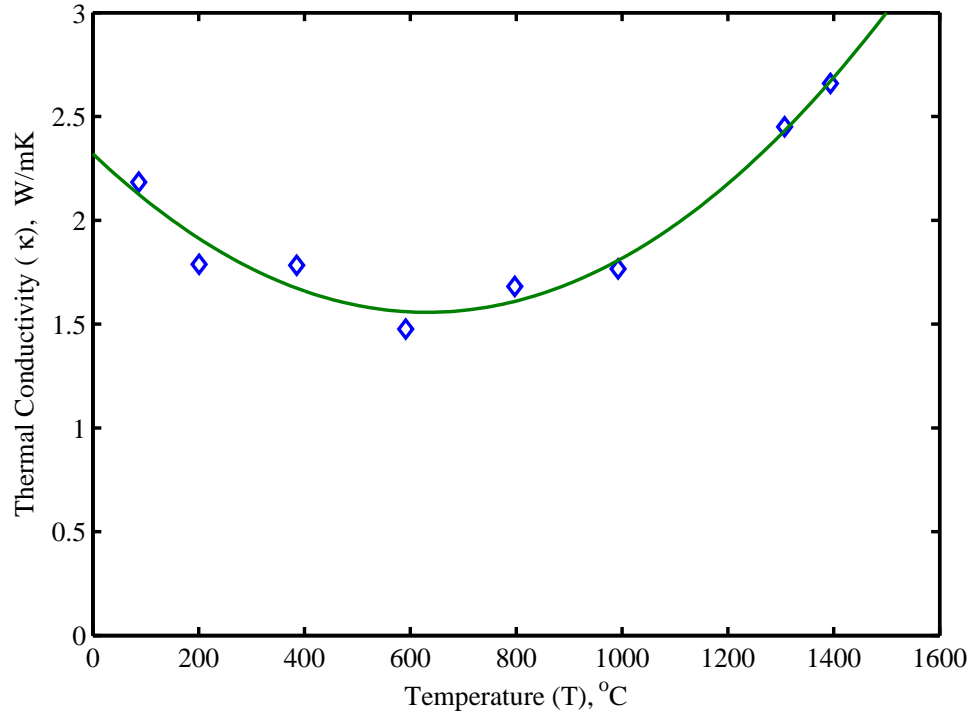


Figure 37: Ultramet SiC foam thermal conductivity data [Ultramet, 2005] for 65 ppi 10 percent dense SiC foam.

The thermal conductivity (W/mK) of SiC-Foam as a function of temperature (°C) for 100 ppi 20% dense SiC foam, as shown in Figure (37) is represented by:

$$k = 1.916 \times 10^{-6}T^2 - 2.419 \times 10^{-3}T + 2.321 \quad (43)$$

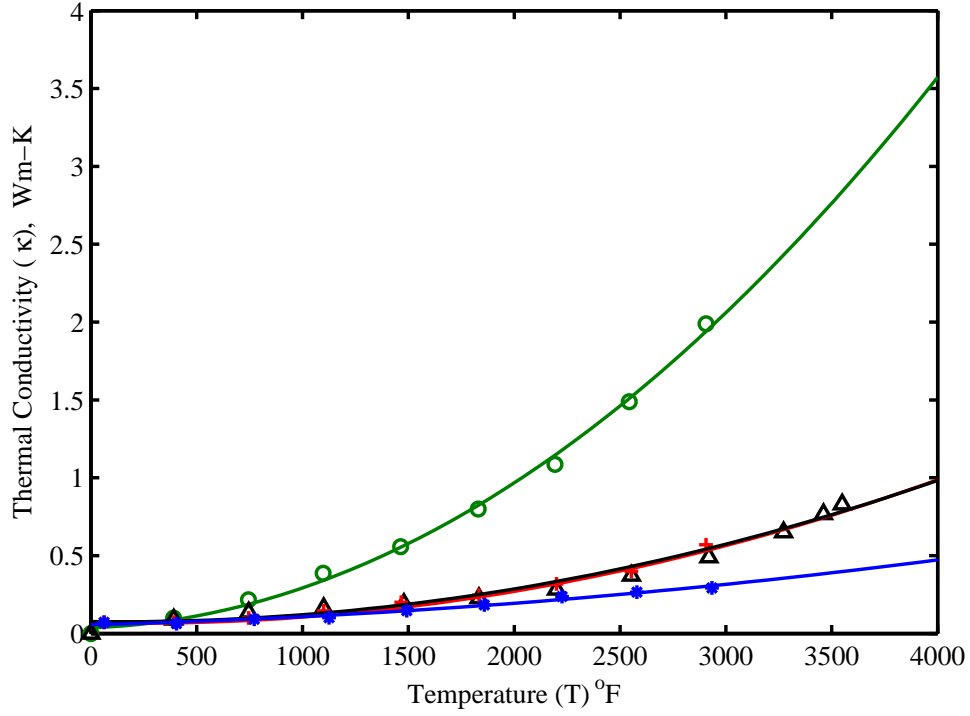


Figure 38: This is a graph of Thermal Conductivity (W/m-K) vs. Temperature (Fahrenheit). The green line represents RVC-1100, the red line represents FRCI-12, the black line represents AFCF-65, and the blue line represents AETB-12.

The thermal conductivity (W/mK) of RVC-1100 as a function of temperature ( $^{\circ}\text{C}$ ) as shown in Figure (38) is represented by:

$$k = 2.093 \times 10^{-7}T + 4.658 \times 10^{-5} + 3.675 \times 10^{-2} \quad (44)$$

The thermal conductivity (W/mK) of AFCF-65 as a function of temperature ( $^{\circ}\text{C}$ ) as shown in Figure (38) is represented by:

$$k = 6.438 \times 10^{-8}T^2 - 2.794 \times 10^{-5}T + 6.885 \times 10^{-2} \quad (45)$$

The thermal conductivity (W/mK) of FRCI-12 as a function of temperature ( $^{\circ}\text{C}$ ) as shown in Figure (38) is represented by:

$$k = 6.089 \times 10^{-8}T^2 - 1.693 \times 10^{-5}T + 7.651 \times 10^{-2} \quad (46)$$

The thermal conductivity (W/mK) of AETB-12 as a function of temperature ( $^{\circ}\text{C}$ ) as shown in Figure (38) is represented by:

$$k = 1.758 \times 10^{-8}T^2 + 3.369 \times 10^{-5}T + 5.658 \times 10^{-2} \quad (47)$$

### 3.3 Mechanical Properties of Foam-SiC

In performing mechanical tests at EMTL, the following methods were followed:

For room temperature tension, the following guidelines were followed. The crosshead velocity of the electromechanical test machine was set at 0.05"/minute and verified utilizing a stop watch and a dial indicator. Samples were positioned in the Instron wedge action grips, and the extensometer attached to the test sample gage section. Load and strain signals were electronically calibrated and strain signals zeroed. All signals were interfaced to a microcomputer via an A/D convertor. The crosshead of the test machine was engaged and the test specimen loaded to failure, with all generated data stored on diskette. Stress versus strain plots were created from stored data files, and the data reduced to provide two physical properties: (1) Elastic modulus, and (2) Tensile Strength.

For elevated temperature compression, the following guidelines were followed. The crosshead velocity of the electromechanical test machine was set at 0.02 in/min, and verified using a stop watch and dial indicator. The specimens were centered between the graphite compressive loading platens in the heated zone of the test furnace, and the elevated temperature contacting extensometer set for a 1 inch gage length and positioned against the test sample surface. Thermocouples were placed against the loading fixture both above and below the test specimen. Note: Thermocouples were not positioned directly in contact with the specimen since sample movement might have been comprised by thermocouple attachment point and attachment method. The air furnace was closed vacuumed out, and backfilled with argon. The backfilling procedure was repeated a second time to ensure that  $O_2$  levels within the test chamber were minimized. Heating of the chamber was initiated using an automated power controller with thermocouple feedback to 5°C/minute, to target temperature. Target test temperature was held for 5 minutes prior to testing. During this time, the load signal was re-zeroed and recalibrated, and the extensometer re-zeroed. The crosshead was engaged, and test specimens loaded to failure with all generated load, strain, and temperature data stored on diskette. Stress-strain plots were generated from stored data, with compressive modulus and ultimate compressive strength calculated for each test.

For room temperature core shear, the following guidelines were followed. The crosshead velocity of the servohydraulic test machine was set at 0.02"/minute and verified utilizing a stop watch and a dial indicator. Specimens were installed within the two piece clevis style pin shear fixture, with approximately equal amounts protruding from opposite ends of the fixture. The crosshead of the test machine was engaged and the specimen loaded to failure. Load readings generated during the test temperature were acquired on an X-Y recorder and plotted versus time. The ultimate shear load applied to the sample at failure was determined, and this value divided by twice the shear plane area of the specimen (samples failed on two planes) in order to calculate ultimate shear strength.

Table 1: Room temperature properties of SiC foam

Sample Number	Elastic Modulus (Msi)	Ultimate Tensile Strength (ksi)	Strain (%)	Density (g/cc)
T65 10-1	0.704	0.40	0.060	0.3948
T65 10-3	0.800	0.57	0.072	0.3809
T65 20-1r	1.89	0.84	0.044	0.5010
T65 20-2	1.75	0.86	0.048	0.5156
T65 20-2r	1.85	0.97	0.050	0.5156
T100 10-2	0.422	0.27	0.069	0.3078
T100 10-2r	0.436	0.28	0.064	0.3078
T100 10-3	0.485	0.30	0.062	0.2750
T100 20-1r	1.20	0.61	0.054	0.5022
T100 20-2	1.74	N/A	0.016	0.5216
T100 20-2r	1.45	0.84	0.063	0.5216
T100 20-3	N/A	1.06	0.048	0.5180

### 3.3.1 Mechanical Test Results

Room temperature mechanical test data are shown in Table 1 for the various foam samples provided by Ultramet.

Table 2: The properties of various SiC foams at 1000°C

Sample Number	Elastic Modulus (msi)	Ultimate Compressive Strength (ksi)	Strain (%)	Density (g/cc)
65 ppi-10% Density	0.729	0.725	0.052	0.237
65 ppi-10% Density	N/A	0.926	0.083	0.268
65 ppi-10% Density	0.565	1.05	0.260	0.307
65 ppi-10% Density	0.565	1.05	0.063	0.307
65 ppi-20% Density	2.13	1.47	0.085	0.498
65 ppi-20% Density	2.13	1.47	0.063	0.498
65 ppi-20% Density	1.08	2.03	0.2	0.605



### 3.3.2 Property and Correlations

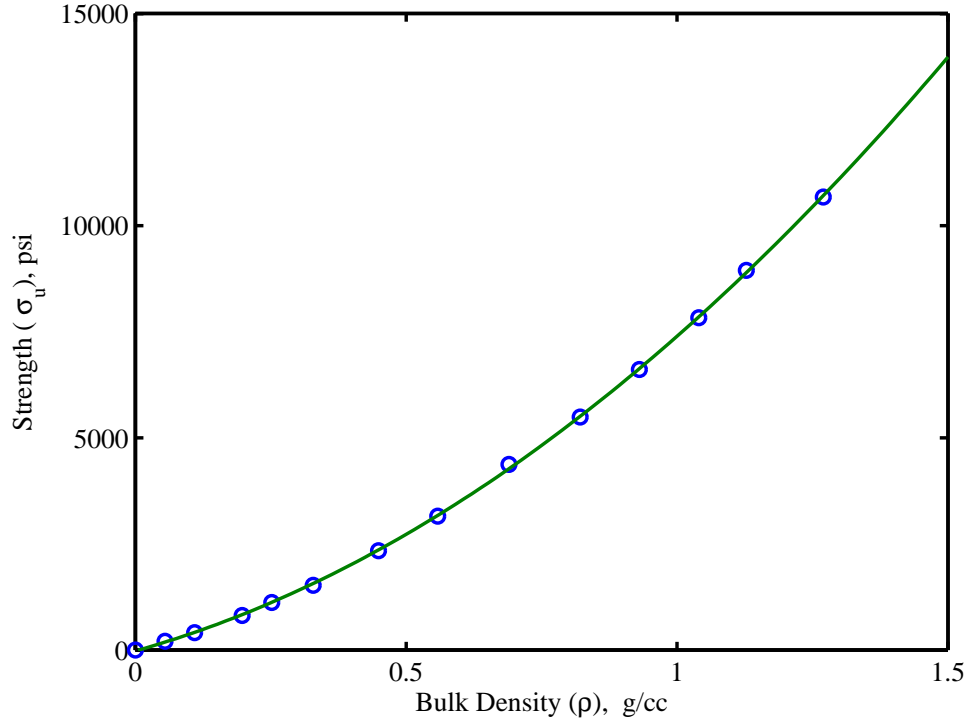


Figure 39: Compressive data set for Strength vs. Bulk Density for 80-ppi, 20% dense SiC foam.

The compressive data set for the strength (psi) of foam-SiC as a function of bulk density (g/cc) as shown in Figure (39) is represented by:

$$\sigma_u = 3.832 \times 10^3 \rho^2 + 3.585 \times 10^3 \rho - 0.024 \times 10^3 \quad (48)$$

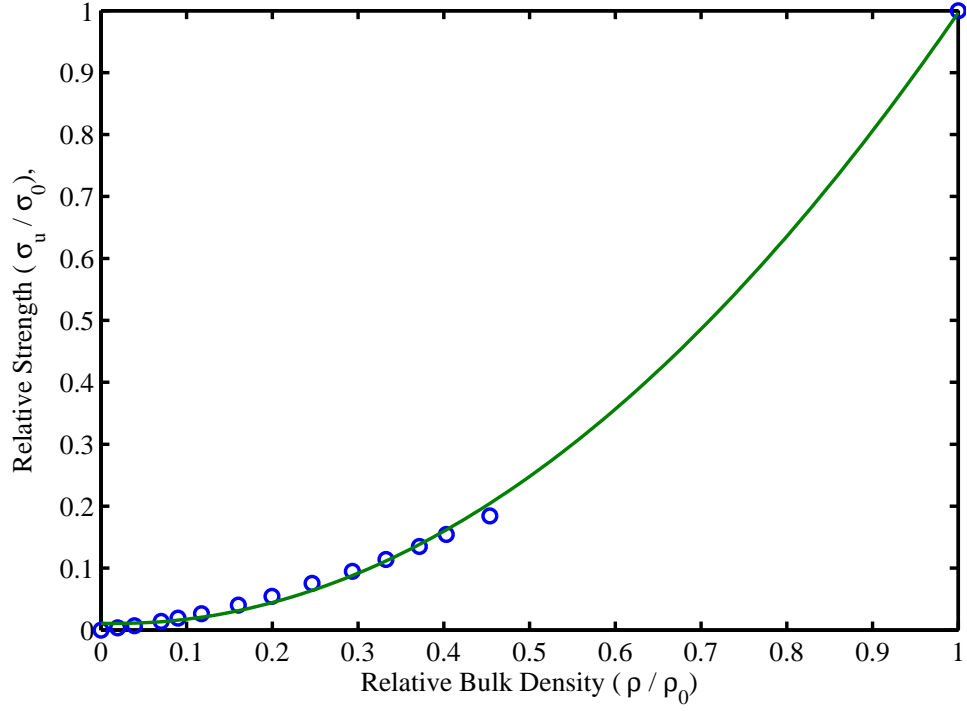


Figure 40: Relative Compressive Data Set for Strength vs. Bulk Density for 80-ppi, 20% dense SiC foam.

The relative compressive data set for the strength of foam-SiC as a function of relative density as shown in Figure (40) is represented by:

$$\frac{\sigma_u}{\sigma_0} = 1.023\left(\frac{\rho}{\rho_o}\right)^2 - 3.796 \times 10^{-2} \frac{\rho}{\rho_o} + 1.103 \times 10^{-2} \quad (49)$$

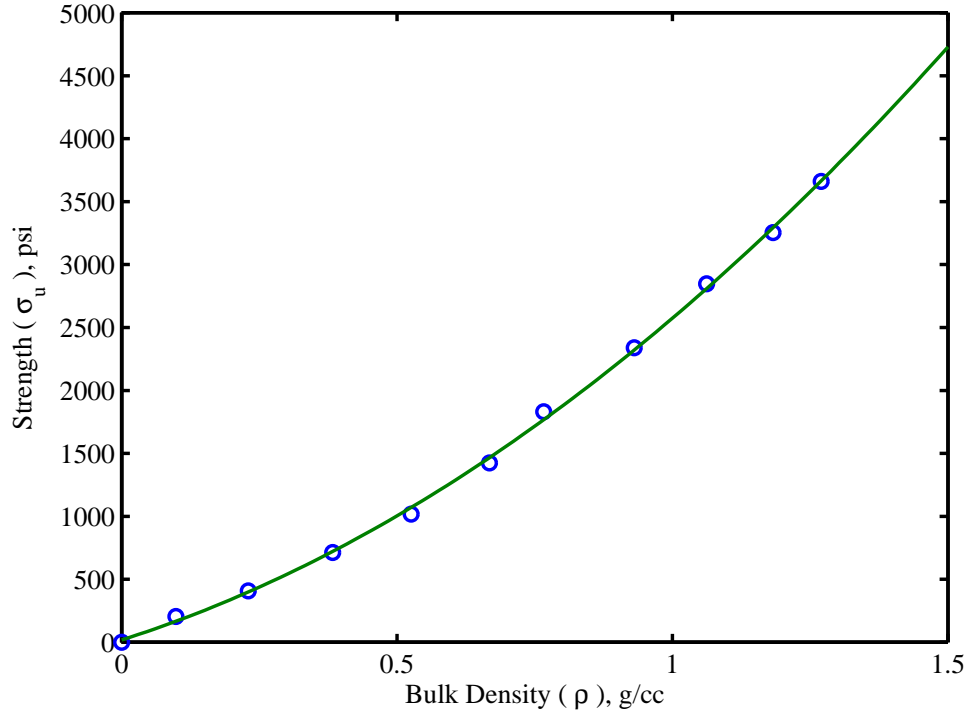


Figure 41: Tensile data set for Strength vs. Bulk Density for 80-ppi, 20% dens SiC foam.

The tensile data set for the strength (psi) of foam-SiC as a function of bulk density (g/cc) as shown in Figure (41) is represented by:

$$\sigma_u = 1.169 \times 10^3 \rho^2 + 1.387 \times 10^3 \rho + 0.018 \times 10^3 \quad (50)$$

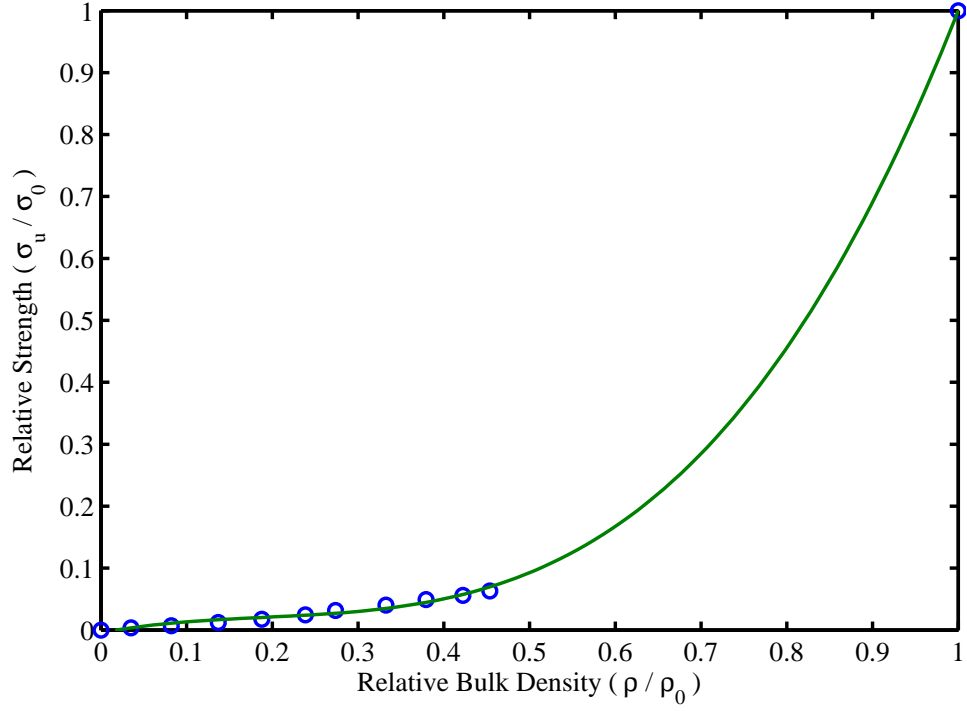


Figure 42: Relative Tensile data set for Strength vs. Bulk Density for 80-ppi, 20% dense SiC foam.

The relative tensile data set for the strength of foam-SiC as a function of relative density as shown in Figure (42) is represented by:

$$\frac{\sigma_u}{\sigma_o} = 1.749\left(\frac{\rho}{\rho_o}\right)^3 - 1.003\left(\frac{\rho}{\rho_o}\right)^2 + 0.258\frac{\rho}{\rho_o} - 4.303 \times 10^{-3} \quad (51)$$

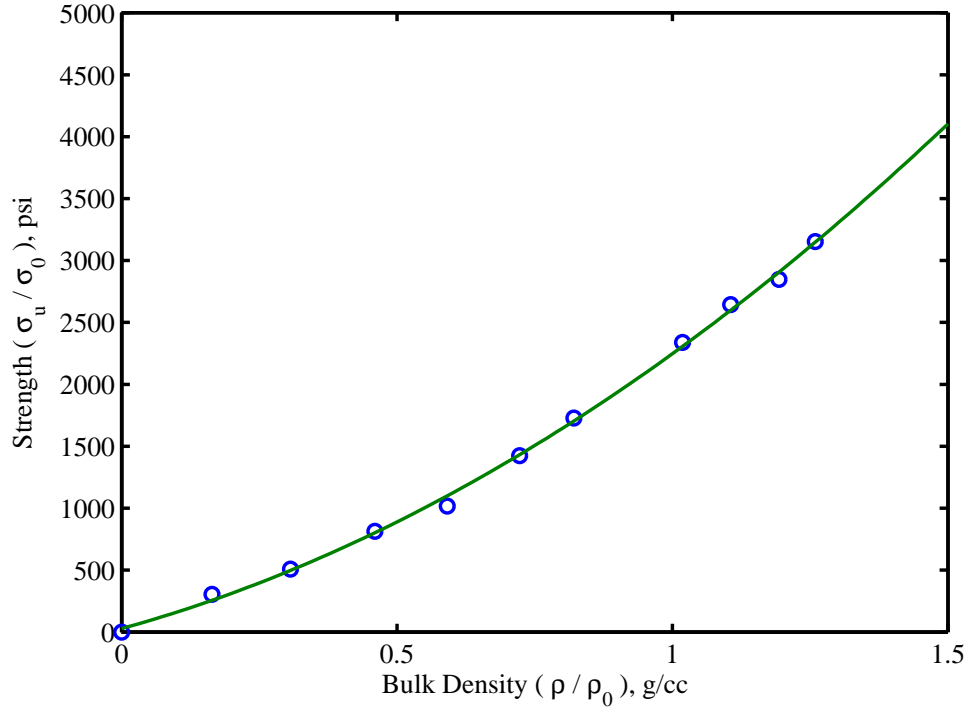


Figure 43: Shear data set for Strength vs. Bulk Density for 80-ppi, 20% dense SiC foam.

The shear data set for the strength (psi) of foam-SiC as a function of bulk density (g/cc) as shown in Figure (43) is represented by:

$$\sigma_u = 0.995 \times 10^3 \rho^2 + 1.225 \times 10^3 \rho + 0.028 \times 10^3 \quad (52)$$

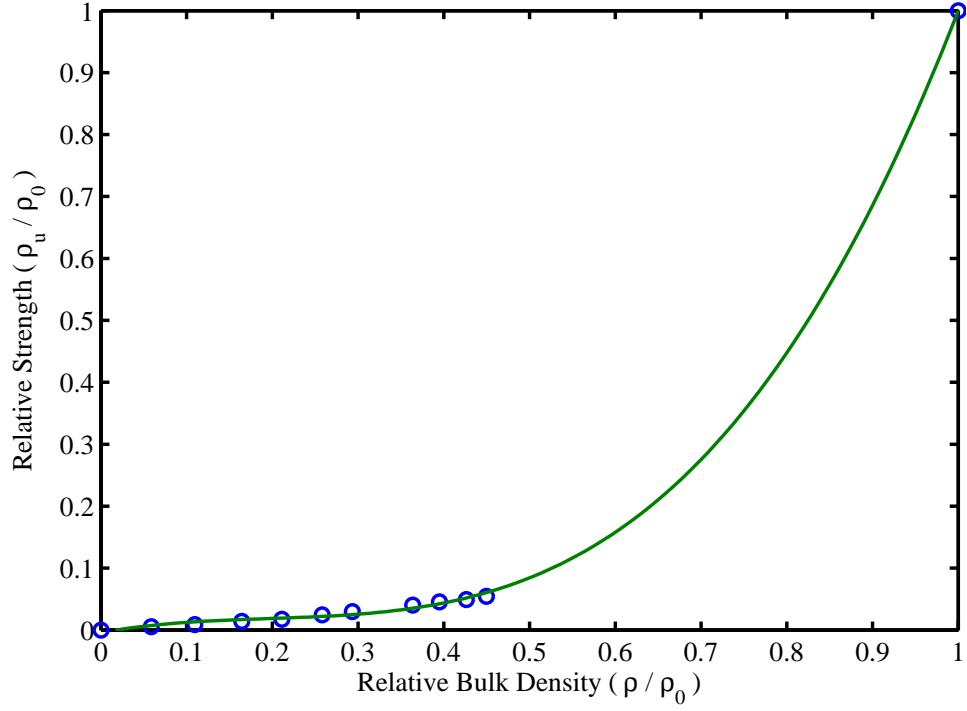


Figure 44: Relative Shear data set for Strength vs. Bulk Density for 80-ppi, 20% dense SiC foam.

The relative shear data set for the strength of foam-SiC as a function of relative density as shown in Figure (44) is represented by:

$$\frac{\sigma_u}{\sigma_o} = 1.809\left(\frac{\rho}{\rho_o}\right)^3 - 1.06\left(\frac{\rho}{\rho_o}\right)^2 + 0.258\frac{\rho}{\rho_o} - 4.303 \times 10^{-3} \quad (53)$$

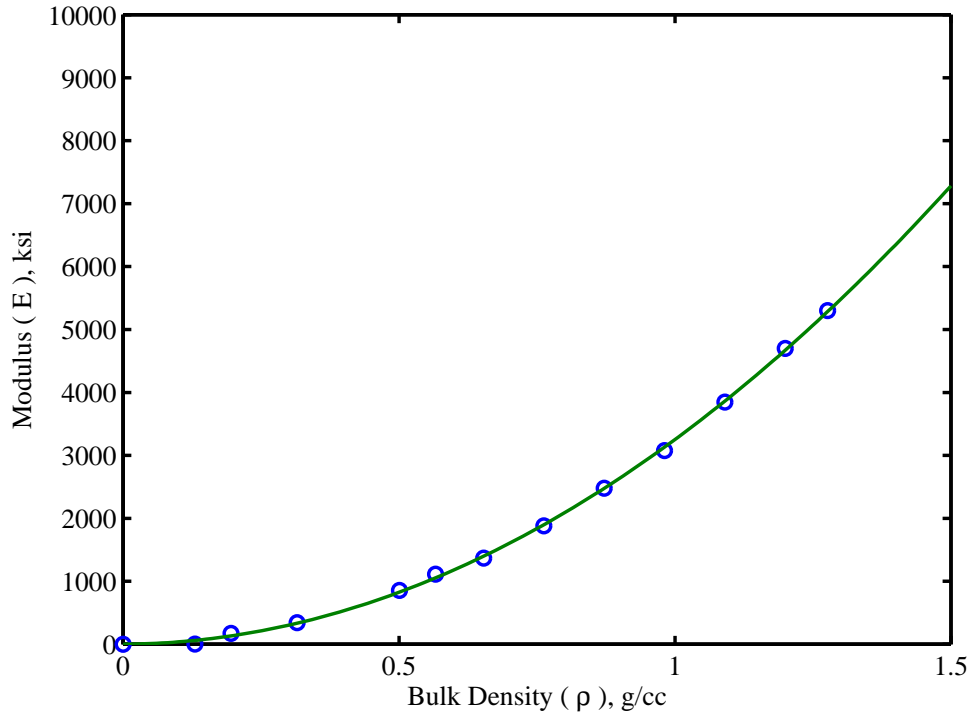


Figure 45: Tensile data set for Young's modulus vs. bulk density for 80-ppi, 20% dense SiC foam.

The tensile data set for Young's modulus as a function of density as shown in Figure (45) is represented by:

$$E = 3.206 \times 10^3 \rho^2 + 4.728 \times \rho - 6.883 \times 10^{-1} \quad (54)$$

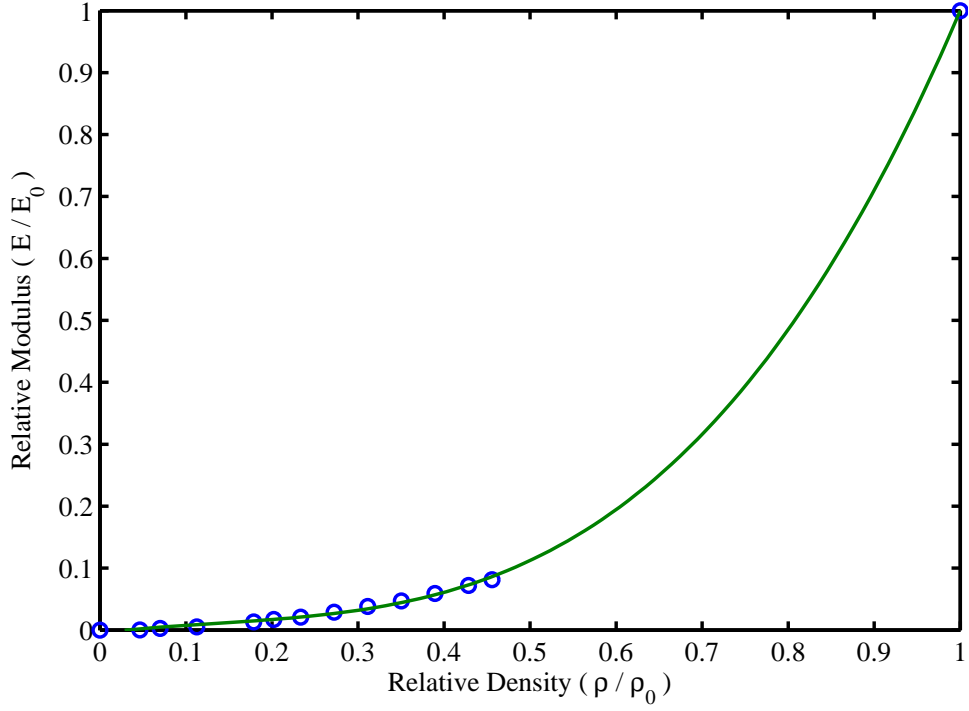


Figure 46: Relative Tensile data set for Young's modulus vs. bulk density for 80-ppi 20% dense SiC foam.

The relative tensile data set for the relative Young's modulus as a function of relative density as shown in Figure (46) is represented by:

$$\frac{E}{E_o} = 1.402\left(\frac{\rho}{\rho_o}\right)^3 - 0.562\left(\frac{\rho}{\rho_o}\right)^2 + 0.164\frac{\rho}{\rho_o} - 4.576 \times 10^{-3} \quad (55)$$



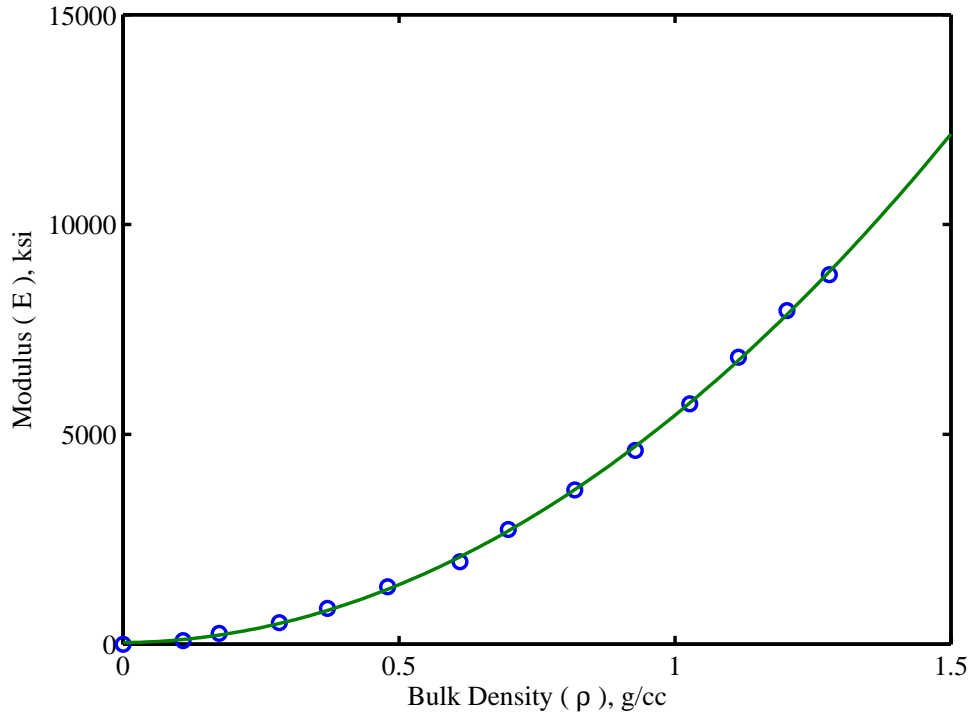


Figure 47: Compressive data set for Modulus vs. Bulk Density for 80-ppi 20%

The compressive data set for the modulus as a function of density as shown in Figure (47) is represented by:

$$K = 5.318 \times 10^3 \rho^2 + 1.004 \times 10^2 \rho + 3.761 \times 10 \quad (56)$$

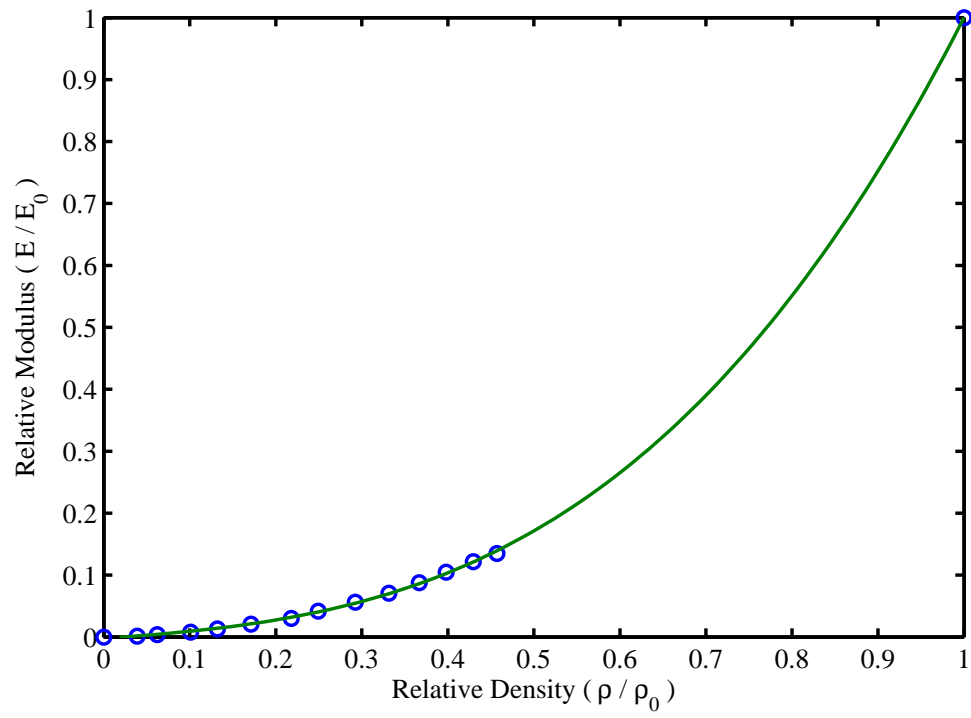


Figure 48: This data set represents the relative compressive data set for Young's modulus of SiC-Foam.

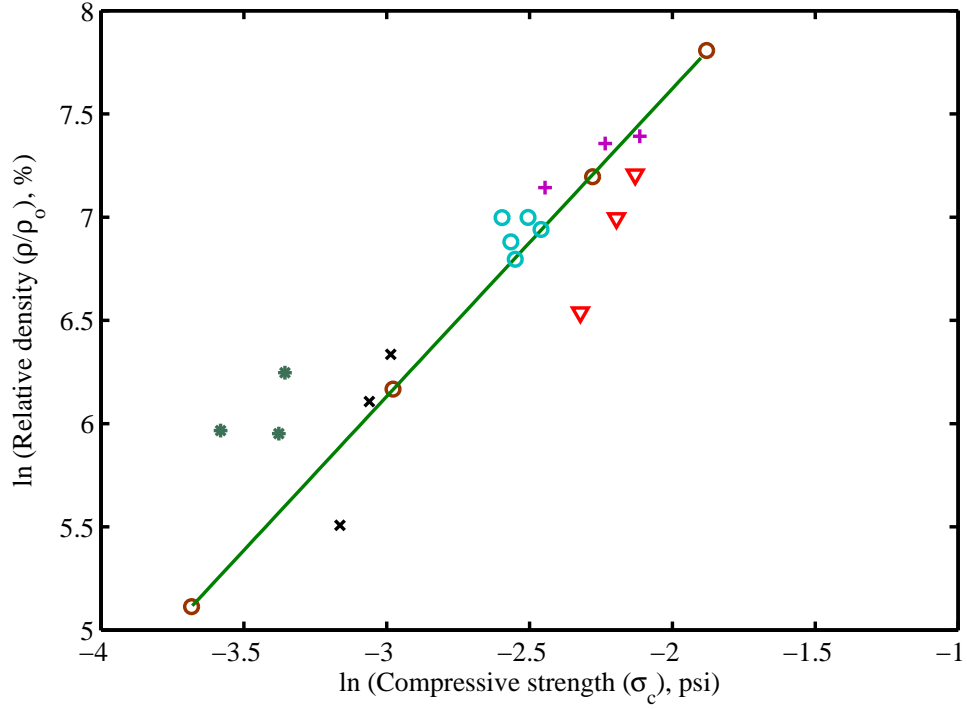


Figure 49: This is a graph of relative density (%) vs. compressive strength (psi) for various SiC foams. The HT was 100 hours at 1830 in AR +5.9%. The  $\square$  symbol represents the Theoretical value, with  $\text{psi} = 42,000(RD)^3/2$ , the + symbol represents 45 ppi 10% after HT, the  $\nabla$  symbol represents 45 ppi 10% as received, the \* symbol represents 45 ppi 3% as received, the  $\times$  symbol represents 45 ppi 3% after HT, the oC symbol represent 65 ppi 3% as received

For the theoretical value for the relative density (%) as a function of compressive strength (psi) for SiC-Foam as shown in Figure (49)

$$\ln\left(\frac{\rho}{\rho_o}\right) = 1.491 \ln(\sigma_c) + 10.603 \quad (57)$$

A direct relationship between the relative density and compressive strength can be written as:

$$\sigma_c = \quad (58)$$

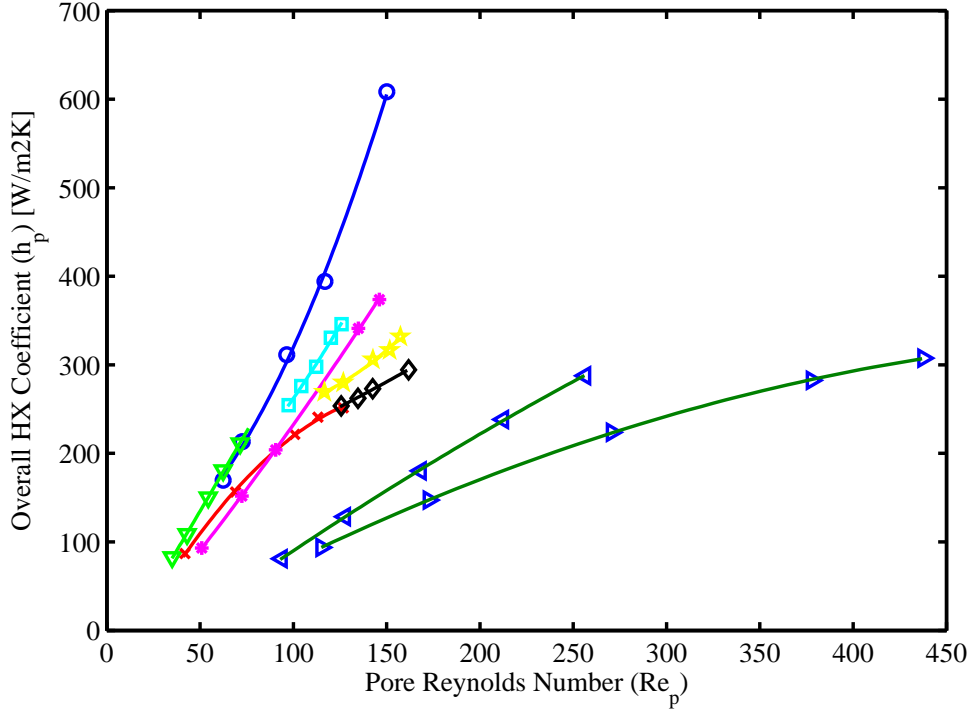


Figure 50: This is a graph of the Overall HX coefficient ( $W/m^2K$ ) as a function of the Pore Reynolds Number. The  $\circ$  symbol represents SiC-100-89-1/4'', the  $\square$  symbol represents SiC-65-89-1/4'', the  $*$  symbol represents SiC-100-88-1/4'', The  $\star$  symbol represents SiC-100-89-3/8'', the  $\diamond$  symbol represents SiC-65-90-3/8'', the  $\times$  symbol represents SiC-100-90-3/8'', The  $\nabla$  represents SiC-100-77-3/8'', and the  $\triangleright$  symbol represents SiC-20-90-3/8''

### 3.4 Fluid Flow and Heat transfer

The overall heat transfer coefficient ( $h_p$ ), ( $Wm^{-2}K^{-1}$ ) as a function of the pore Reynolds number ( $Re_p$ ) as shown in in Figure (50), has 9 different samples, and each sample has its own design equation:

The design equation for SiC-100-89-1/4'' is:

$$h_p = 2.1321 \times 10^{-2} Re_p^2 + 3.8296 \times 10^{-1} Re_p + 68.26 \quad (59)$$

The design equation for SiC-100-80-1/4'' is:

$$h_p = 1.367 \times 10^{-3} Re_p^2 + 3.434 Re_p - 40.43 \quad (60)$$

The design equation for SiC-100-90-3/8'' is:

$$h_p = -1.214 \times 10^{-2} Re_p^2 + 4.021 Re_p - 61.223 \quad (61)$$

The design equation for SiC-65-89-1/4'' is:

$$h_p = 9.94 \times 10^{-3} Re_p^2 + 1.053 Re_p + 57.42 \quad (62)$$

The design equation for SiC-100-88-1/4" is:

$$h_p = 2.646 \times 10^{-3} Re_p^2 + 2.446 - 38.7 \quad (63)$$

The design equation for SiC-100-89-3/8" is:

$$h_p = 1.188 \times 10^{-2} Re_p^2 - 1.743 Re_p + 31.07 \quad (64)$$

The design equation for SiC-100-90-3/8" is:

$$h_p = 1.367 \times 10^{-3} Re_p^2 + 7.498 \times 10^{-1} Re_p + 1.375 \times 10^2 \quad (65)$$

The design equation for SiC-100-77-3/8" is:

$$h_p = -8.758 \times 10^{-4} Re_p^2 + 1.581 Re_p - 59.33 \quad (66)$$

The design equation for SiC-20-90-3/8" is:

$$h_p = -1.018 \times 10^{-3} Re_p^2 + 1.223 Re_p - 33.56 \quad (67)$$

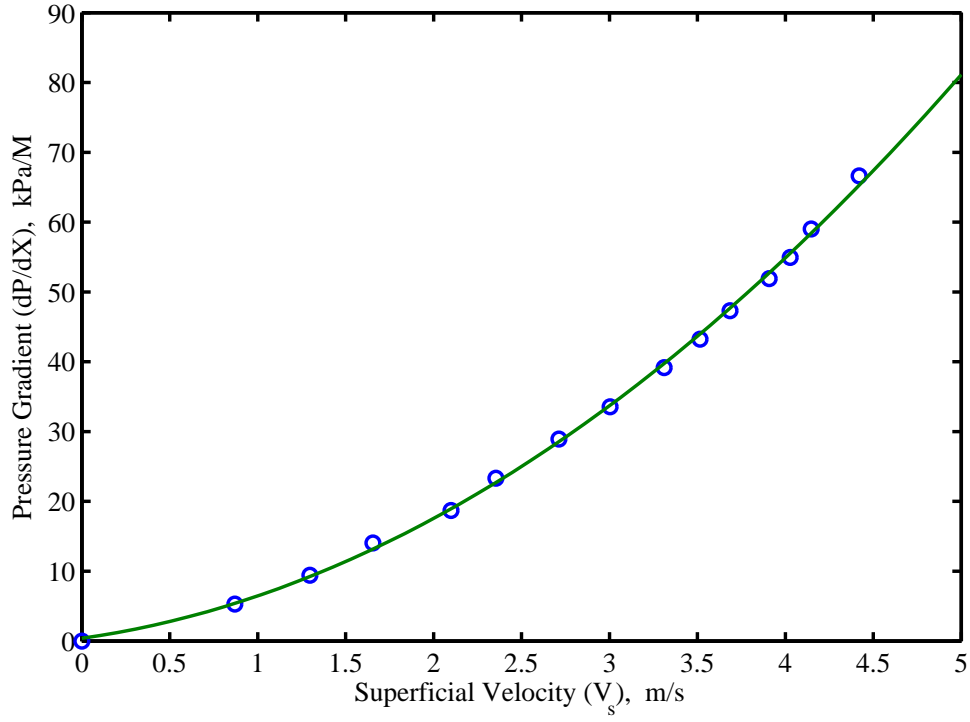


Figure 51: This is a graph of the Pressure Gradient (kPa/m) as a function of the superficial Velocity (m/s) for the sample SiC-65-0.8873

The design equation for the pressure gradient ( $\frac{dP}{dX}$ , kPa/m) as a function of the superficial velocity ( $V_s$ , m/s) for the sample SiC-65-0.8873 as shown in Figure (51) is:

$$\frac{dP}{dX} = 2.522(V_s)^2 + 3.532V_s \quad (68)$$

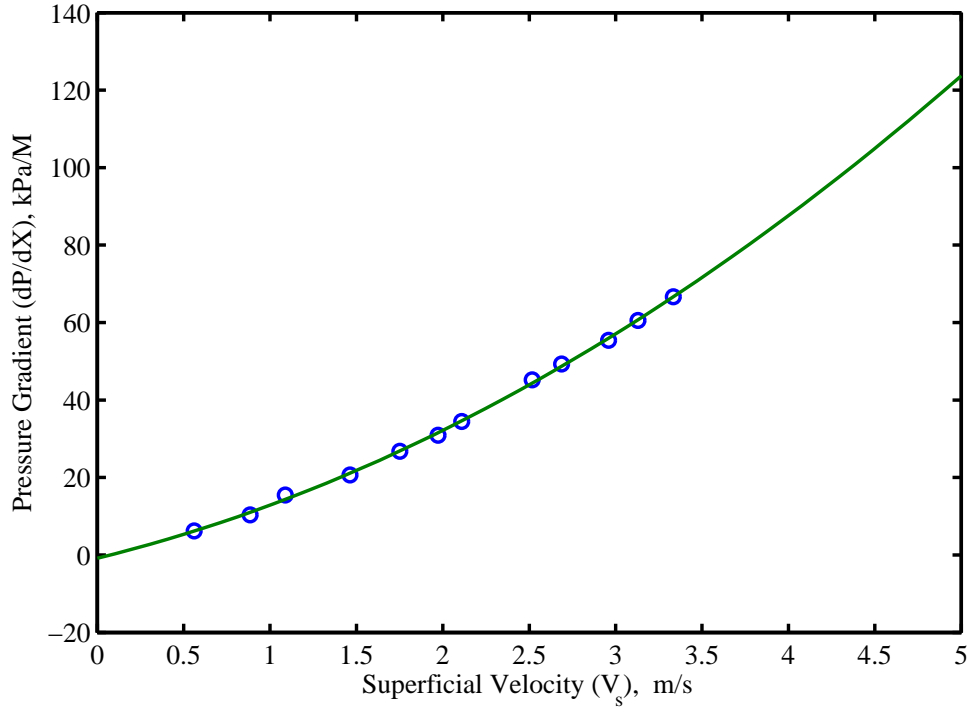


Figure 52: This is a graph of the Pressure Gradient (kPa/m) as a function of the superficial Velocity (m/s) for the sample SiC-65-0.8034

The design equation for the pressure gradient ( $\frac{dP}{dX}$ , kPa/m) as a function of the superficial velocity ( $V_s$ , m/s) for the sample SiC-65-0.8034 as shown in Figure (52) is:

$$\frac{dP}{dX} = 2.803(V_s)^2 + 10.899V_s \quad (69)$$

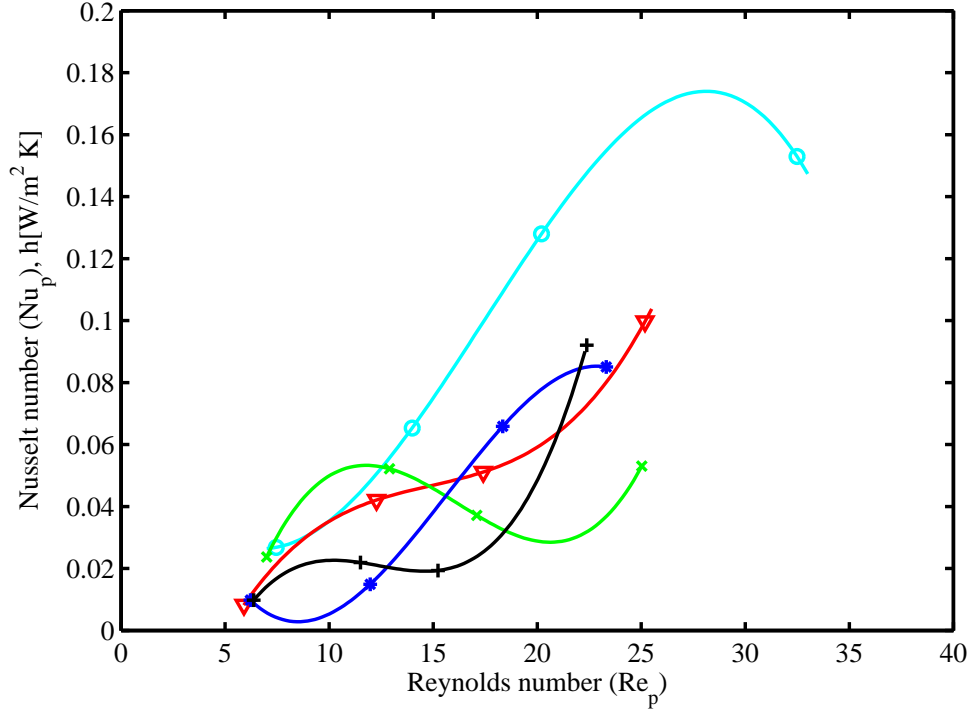


Figure 53: This graph depicts various types of SiC foam Nusselt number as a function of the Reynolds number. The O symbol represents SiC 80 ppi,  $e = 0.915$ , the  $\nabla$  symbol represents SiC 100 ppi,  $e = 0.886$ , the x symbol represents SiC 130 ppi,  $e = 0.895$ , the \* symbol represents SiC 130 ppi,  $e = 0.881$ , and the + symbol represents SiC 130 ppi,  $e = 0.857$ .

Figure (53) contains various graphs of SiC foam Nusselt number as a function of Reynolds number, the design equations for each curve are:

SiC 80 ppi,  $e = 0.915$

$$Nu_p = 3.048 \times 10^{-5} Re_p^3 + 1.597 \times 10^{-3} Re_p^3 - 1.752 \times 10^{-2} Re_p + 8.127 \times 10^{-2} \quad (70)$$

SiC 100 ppi,  $e = 0.886$

$$Nu_p = 3.406 \times 10^{-5} Re_p^3 - 1.521 \times 10^{-3} Re_p^2 + 2.419 \times 10^{-2} Re_p - 8.858 \times 10^{-2} \quad (71)$$

SiC 130 ppi,  $e = 0.881$

$$Nu_p = 7.163 \times 10^{-5} Re_p^3 + 2.62 \times 10^{-3} Re_p^2 - 3.25 \times 10^{-2} Re_p + 1.239 \times 10^{-1} \quad (72)$$

SiC 130 ppi,  $e = 0.857$

$$Nu_p = 8.383 \times 10^{-5} Re_p^3 - 3.12 \times 10^{-3} Re_p^2 + 3.75 \times 10^{-2} Re_p - 1.242 \times 10^{-1} \quad (73)$$



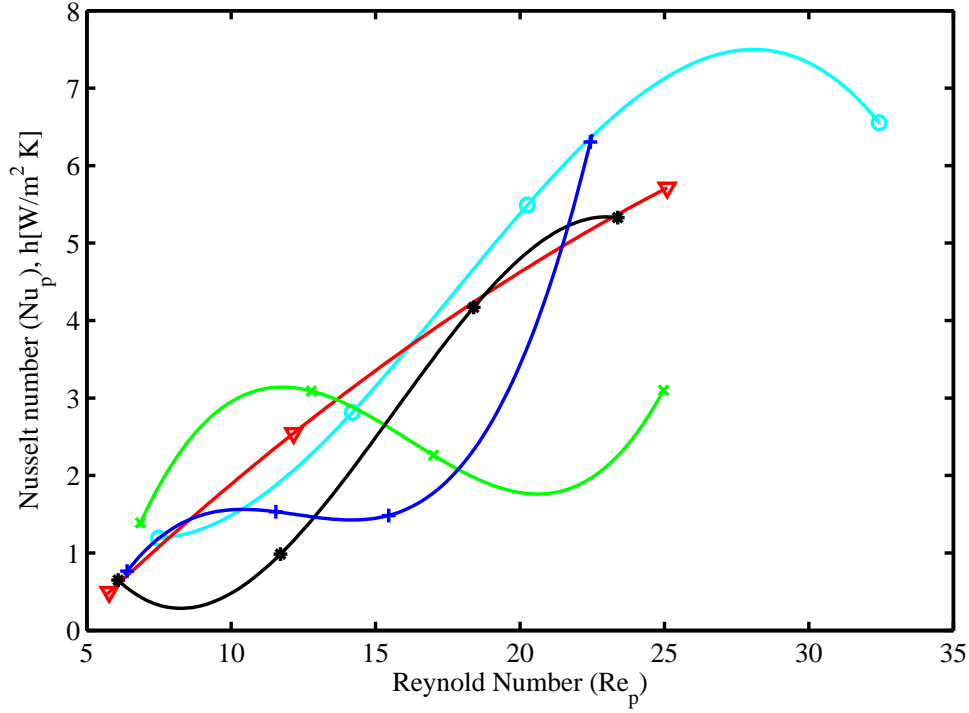


Figure 54: This graph depicts various types of SiC foam Nusselt number as a function of the Reynolds number. The O symbol represents SiC 80 ppi,  $e = 0.915$ , the  $\nabla$  symbol represents SiC 100 ppi,  $e = 0.886$ , the x symbol represents SiC 130 ppi,  $e = 0.895$ , the \* symbol represents SiC 130 ppi,  $e = 0.881$ , and the + symbol represents SiC 130 ppi,  $e = 0.857$ .

Figure (54) contains several graphs of SiC foam heat transfer coefficient ( $h$ ) as a function of the Reynolds number ( $Re_p$ ), the design equation for each of these curves are:

SiC 80 ppi,  $e = 0.915$

$$h_p = -1.404 \times 10^{-3} Re_p^3 + 7.45 \times 10^{-2} Re_p^2 - 8.621 \times 10^{-1} Re_p + 4.06 \quad (74)$$

SiC 100 ppi,  $e = 0.886$

$$h_p = -3.962 \times 10^{-3} Re_p^2 + 3.926 \times 10^{-1} Re_p - 1.642 \quad (75)$$

SiC 130 ppi,  $e = 0.895$

$$h_p = 4.001 \times 10^{-3} Re_p^3 - 1.943 \times 10^{-1} Re_p^2 + 2.912 Re_p - 10.734 \quad (76)$$

SiC 130 ppi,  $e = 0.881$

$$h_p = -3.163 \times 10^{-3} Re_p^3 + 1.483 \times 10^{-1} Re_p^2 - 1.803 Re_p + 6.841 \quad (77)$$

SiC 130 ppi,  $e = 0.857$

$$h_p = 5.14 \times 10^{-3} Re_p^3 - 1.895 \times 10^{-1} Re_p^2 + 2.275 Re_p - 7.377 \quad (78)$$

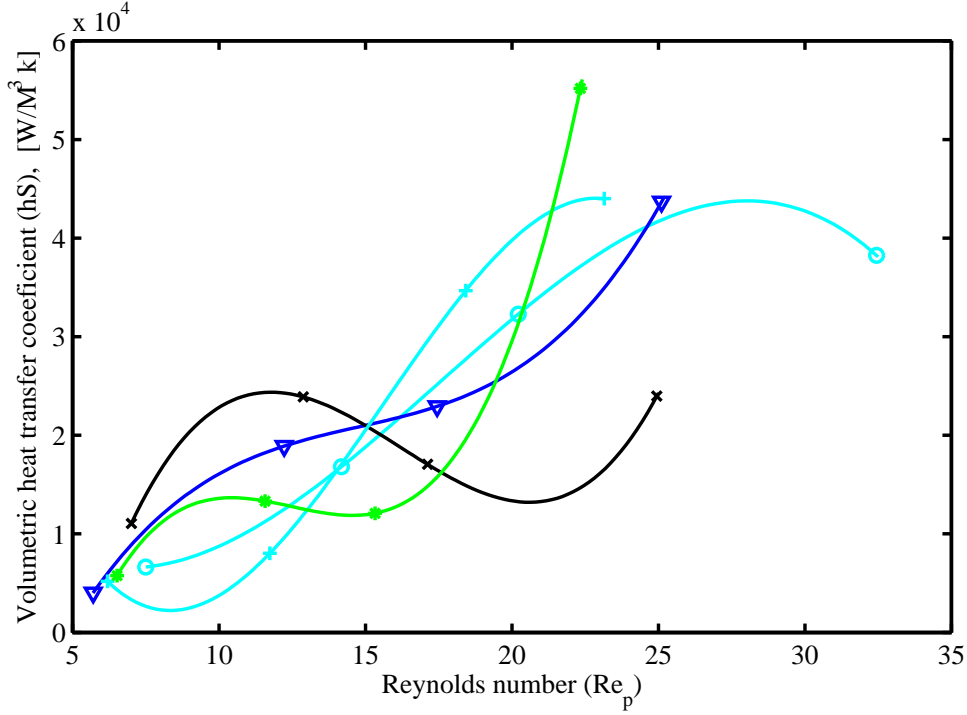


Figure 55: This graph depicts various types of SiC foam Volumetric Heat Transfer Coefficient being graphed as a function of the Reynolds number. The O symbol represents SiC 80 ppi,  $e = 0.915$ , the  $\nabla$  symbol represents SiC 100 ppi,  $e = 0.886$ , the x symbol represents SiC 130 ppi,  $e = 0.895$ , the + symbol represents SiC 130 ppi,  $e = 0.881$ , and the \* symbol represents SiC 130 ppi,  $e = 0.857$ .

Figure (55) contains several graphs of SiC foam volumetric heat transfer coefficient ( $h_s$ ) as a function of the Reynolds number ( $Re_p$ ), the design equation for each of these curves are:

SiC 80 ppi,  $e = 0.915$

$$h_s = -7.854Re_p^3 + 4.112 \times 10^2 Re_p^2 - 4.537 \times 10^3 Re_p + 2.084 \times 10^4 \quad (79)$$

SiC 100 ppi,  $e = 0.886$

$$h_s = 14.378Re_p^3 - 6.374 \times 10^2 Re_p^2 + 1.009 \times 10^4 Re_p - 3.549 \times 10^4 \quad (80)$$

SiC 130 ppi,  $e = 0.895$

$$h_s = 32.502Re_p^3 - 1.579 \times 10^3 Re_p^2 + 2.367 \times 10^4 Re_p - 8.847 \times 10^4 \quad (81)$$

SiC 130 ppi,  $e = 0.881$

$$h_s = -27.151Re_p^3 + 1.271 \times 10^3 Re_p^2 - 1.553 \times 10^4 Re - P + 5.905 \times 10^4 \quad (82)$$

SiC 130 ppi,  $e = 0.857$

$$h_s = 51.193Re_p^3 - 1.919 \times 10^3 Re_p^2 + 2.331 \times 10^4 Re_p - 7.888 \times 10^4 \quad (83)$$

## 4 Radiation Effects on SiC Properties

Table 3: Comparison of properties of commercial SiC-based fibers and bulk SiC(1-4).

	cg-Nicalon	Hi-Nicalon	Hi-Nicalon type S	Dow Sylramic	Bulk SiC
Diameter ( $\mu\text{m}$ )	14	12-14	12	10	N/A
Tensile Strength (GPa)	2.0-3.0	2.8-3.4	2.6-2.7	2.8-3.4	0.1
Elastic modulus (GPa)	170-220	270	420	390-400	0.1
Density ( $\text{g}/\text{cm}^3$ )	2.55	2.74	2.98-3.10	3.0-3.10	3.25
Coefficient of thermal expansion ( $10^{-6}/\text{K}$ )	3.2	3.5	N/A	5.4	4.0
Thermal Conductivity at 20°C ( $\text{W}/\text{m}\cdot\text{K}$ )	1.5	4	18	40-45	100-350
Oxygen content (wt.%)	11.7	0.5	0.2	0.8	0.0
C/Si atomic ratio	1.31	1.39	1.05	1.0	1.0

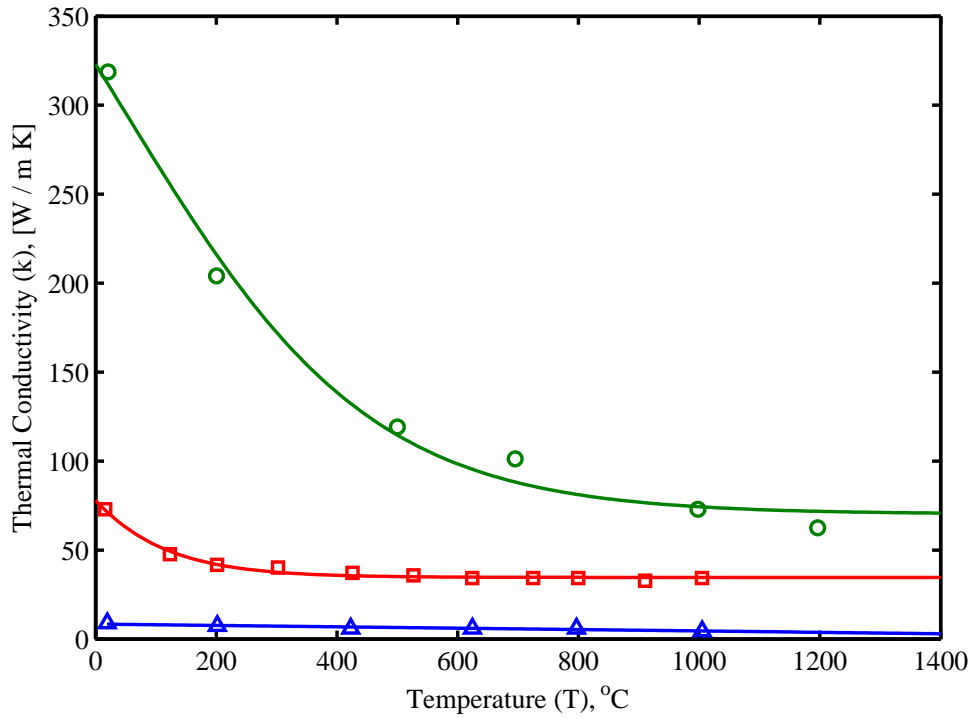


Figure 56: Comparison of the transverse thermal conductivity of monolithic CVD SiC. (Data points acquired from [39], [40])

Figure (56) displays the effects of temperature (T) on thermal conductivity (k) for three different types of composites. The design equation for each one is:

CVD SiC

$$k = 70.21 + \frac{4.47 \times 10^2}{7.681 \times 10^{-1} \times e^{-4.937 \times 10^{-3} T}} \quad (84)$$

CVR SiC/SiC

$$k = 34.641 + \frac{5.065 \times 10^2}{10.689 \times e^{-9.245 \times 10^{-3}T}} \quad (85)$$

CVI SiC/SiC

$$k = -3.895 \times 10^{-3}T + 8.447 \quad (86)$$

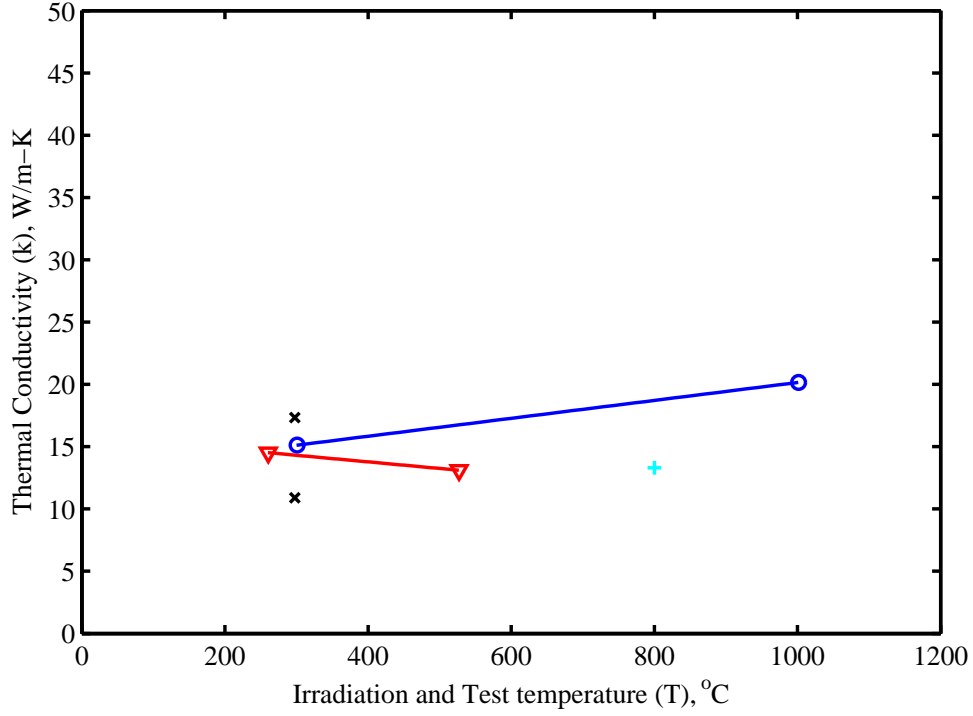


Figure 57: This graph depicts the effects of neutron irradiation on the thermal conductivity of bulk SiC. The studies were performed on samples irradiated to 25-43 dpa, whereas the data by Snead et al. were obtained on samples irradiated to 0.1 dpa. The x represents Snead et al. 1998, Morton and GE sintered SiC, the  $\nabla$  represents Youngblood and Jones 1997, Morton CVD, The o represents Senor et al 1996, Morton CVD, and the + represents Hollenber et al 1995 SiC. [41] [42] [43][44]

Figure (57) displays the effects of neutron irradiation on the thermal conductivity of bulk SiC. The design equation for Youngblood & Jones data is:

$$k = 7.193 \times 10^{-3}T + 12.958 \quad (87)$$

and the design equation for Senor's data is:

$$k = -5.292 \times 10^{-3}T + 15.895 \quad (88)$$

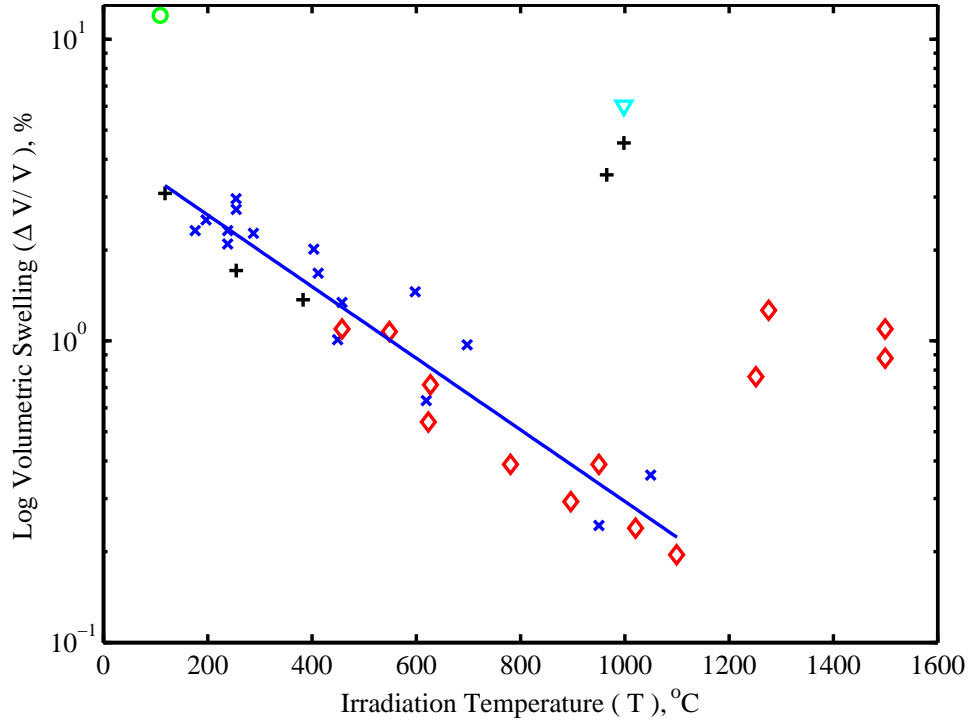


Figure 58: This graph depicts radiation induced swelling in bulk SiC as a function of irradiation temperature. [41] [42] [44] [45] [46]

Figure (58) depicts radiation induced swelling in bulk SiC as a function of irradiation temperature, and a generalized design equation for low temp radiation induced swelling ( $T < 900^{\circ}\text{C}$ ) is:

$$\frac{\Delta V}{V} = 10^{(-2.795 \times 10^{-3}T + 2.872)} \quad (89)$$

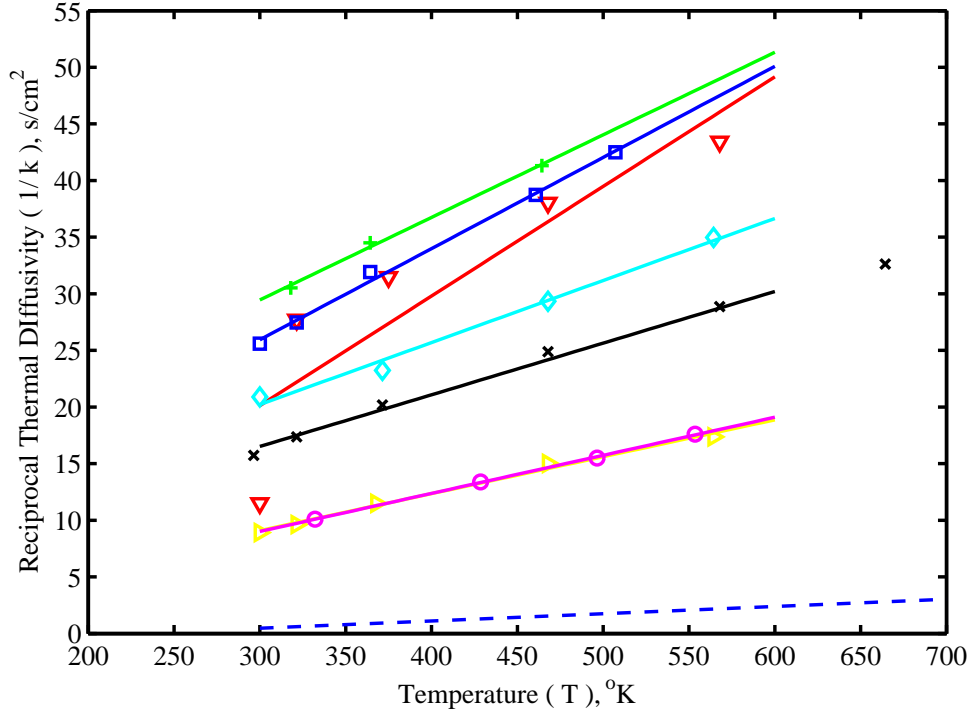


Figure 59: This data set depicts the reciprocal thermal diffusivity ( $\frac{1}{\kappa}$ ) as a function of temperature ( $^{\circ}\text{CK}$ ). [47] The + symbol represents sample M1(252C). The  $\nabla$  symbol represents sample N5(310C). The  $\square$  symbol represents sample N7(310C). The  $\diamond$  symbol represents sample M2(355C). The x symbol represents sample N3(480C). The  $\triangleright$  symbol represents sample N2(800C). The  $\circ$  symbol represents sample N1(800C). The dashed line represents the unirradiated reference sample.

Figure (59) depicts the reciprocal thermal diffusivity ( $\frac{1}{\kappa}$ ) as a function of temperature ( $^{\circ}\text{CK}$ ) for several different samples. Each samples behavior can be easily described by the following first order equation:

Sample M1(252C):

$$\frac{1}{\kappa} = 7.29 \times 10^{-2}T + 7.586 \quad (90)$$

Sample N5(310C):

$$\frac{1}{\kappa} = 9.68 \times 10^{-2}T - 8.919 \quad (91)$$

Sample N7(310C):

$$\frac{1}{\kappa} = 8.049 \times 10^{-2}T + 1.792 \quad (92)$$

Sample M2(355C):

$$\frac{1}{\kappa} = 5.477 \times 10^{-2}T + 3.786 \quad (93)$$



Sample N3(480):

$$\frac{1}{\kappa} = 4.562 \times 10^{-2}T + 2.832 \quad (94)$$

Sample N2(800C):

$$\frac{1}{\kappa} = 3.26 \times 10^{-2}T - 0.69 \quad (95)$$

Sample N1(800C):

$$\frac{1}{\kappa} = 3.363 \times 10^{-2}T - 1.081 \quad (96)$$

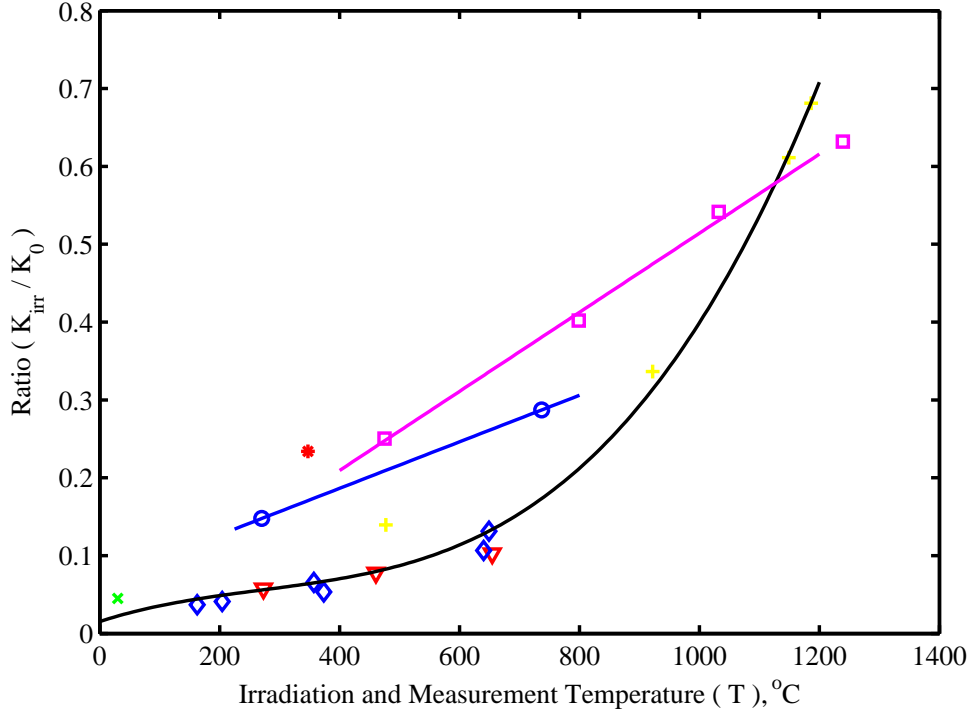


Figure 60: This data set depicts the ratio of  $\frac{K_{ir}}{K_0}$ , measured at the irradiation temperature for high purity CVD-SiC and for two types of 2D f-SiC/SiC. The  $\nabla$  symbol represents data obtained from [48], for a high purity CVD-SiC sample. The x symbol represents data obtained from [49], for a high purity CVD-SiC sample. The + symbols represents data obtained from [50], for a high purity sample of CVD-SiC. The  $\diamond$  symbol represents data obtained from [47]. The black line represents the predicted curve for the ratio of  $\frac{K_{ir}}{K_0}$  as a function of temperature ( $^{\circ}\text{C}$ ) with the generated equation. The  $\square$  symbol represents data obtained from [44], for a Nicalon/ICVI-SiC sample. The  $\circ$  symbol represents data obtained from [47], for a Hi-NiC sample with a thick PYC. The \* symbol represents data obtained from [47], for a Hi-NiC/ICVI-SiC sample with thin PYC.

The Figure (4) depicts the ratio of  $\frac{K_{ir}}{K_0}$ , measured at the irradiation temperature for high purity CVD-SiC and for two types of 2D f-SiC/SiC. The ratio of  $\frac{K_{ir}}{K_0}$ , measured at the irradiation temperature for high purity CVD-SiC can be described by the third order equation generated:

$$\frac{K_{ir}}{K_0} = 6.949 \times 10^{-10}T^3 - 5.619 \times 10^{-7}T^2 + 2.51 \times 10^{-4}T + 1.534 \times 10^{-2} \quad (97)$$

The ratio of  $\frac{K_{ir}}{K_0}$ , measured at the irradiation temperature for Nicalon/ICVI-SiC can be described by the first order generated equation:

$$\frac{K_{ir}}{K_0} = 5.08 \times 10^{-4}T + 6.231 \times 10^{-3} \quad (98)$$

The ratio of  $\frac{K_{ir}}{K_0}$ , measured at the irradiation temperature for Hi-NiC with a thick PYC can be described by the first order generated equation:

$$[h]\frac{K_{ir}}{K_0} = 2.988 \times 10^{-4}T + 6.693 \times 10^{-2} \quad (99)$$

The thermal diffusivity ( $\kappa$ ) as a function of temperature ( $^{\circ}\text{C}$ ) as shown in Figure (4) displays various sample of 2D Hi-Nicalon/ICVI-SiC composites with a thick PyC interface with various irradiated and unirradiated conditions [47]. Some of the samples behavior can be easily described with equations.

The average value of  $\kappa(T)$  for the four samples as received can be described by:

$$\kappa = 3.124 \times 10^{-8}T^2 - 6.934 \times 10^{-5}T + 6.877 \times 10^{-2} \quad (100)$$

The average value of  $\kappa(T)$  for the two unirradiated samples with their PyC interface removed by oxidation can be described by:

$$\kappa = 2.322 \times 10^{-8}T^2 - 4.343 \times 10^{-5}T + 3.016 \times 10^{-2} \quad (101)$$

The average value of  $\kappa(T)$  for the heating of samples D1 and D2 from 200  $^{\circ}\text{C}$  to 1200  $^{\circ}\text{C}$  can be described by:

$$\kappa = 1.975 \times 10^{-8}T^2 - 1.433 \times 10^{-5}T + 1.462 \times 10^{-2} \quad (102)$$

The average value of  $\kappa(T)$  for the cooling of samples D1 and D2 from 200  $^{\circ}\text{C}$  to 1200  $^{\circ}\text{C}$  can be described by:

$$\kappa = 1.547 \times 10^{-8}T^2 - 1.433 \times 10^{-5} + 1.462 \times 10^{-2} \quad (103)$$

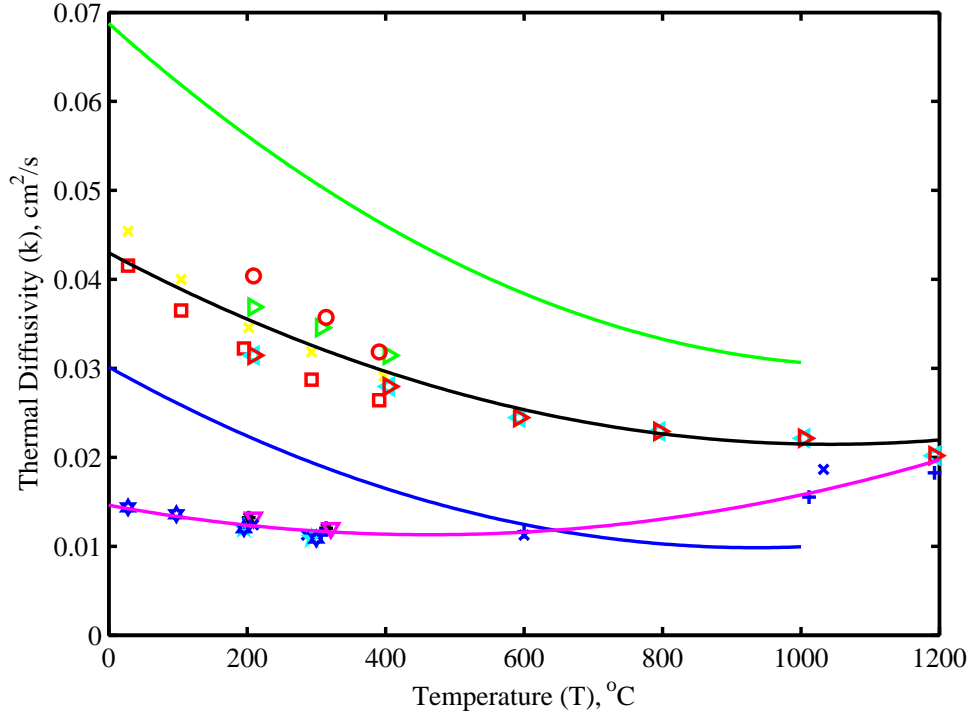


Figure 61: This data set depicts the thermal diffusivity ( $\kappa$ ) as a function of temperature ( $^{\circ}\text{C}$ ) for various samples of 2D Hi-Nicalon/ICVI-SiC composites with a thick PyC interface with various irradiated and unirradiated conditions [47]. The green line represents the average value of  $\kappa(T)$  for four as received samples. The blue line represents the average value of  $\kappa(T)$  for two unirradiated samples with the PyC interface removed by oxidation. [47] used two irradiated samples, D1 and D2, both of which were irradiated at  $335 \pm 35^{\circ}\text{C}$  to 7.1 dpa-SiC, and the samples testing was done in sequence. The  $\square$  symbol represents the  $\kappa(T)$  values for D1 in air. The  $\times$  symbol represents the  $\kappa(T)$  value for D2 in air. The  $*$  symbol represents the  $\kappa(T)$  values for D1 in vacuum. The  $\nabla$  symbol represents the  $\kappa(T)$  values for D2 in vacuum. The  $\triangleleft$  symbol represents the  $\kappa(T)$  values in argon during in situ annealing from approximately  $200^{\circ}\text{C}$  to  $1200^{\circ}\text{C}$  and a 2 hour hold time. The  $+$  symbol represents the same sample D1 being cooled from  $1200^{\circ}\text{C}$  to  $200^{\circ}\text{C}$ . The maroon line marked with the  $\triangleright$  symbol represents the  $\kappa(T)$  values for sample D2 during in situ annealing from approximately  $200^{\circ}\text{C}$  to  $1200^{\circ}\text{C}$ . The  $\bullet$  symbol represents the sample D2 being cooled from  $1200^{\circ}\text{C}$  to  $200^{\circ}\text{C}$ . The  $\diamond$  symbol represents the  $\kappa(T)$  values for sample D1 in helium from  $200^{\circ}\text{C}$  to  $400^{\circ}\text{C}$ . The  $\circ$  symbol represents the  $\kappa(T)$  values for sample D2 in helium from  $200^{\circ}\text{C}$  to  $400^{\circ}\text{C}$ . The  $\star$  symbol represents the  $\kappa(T)$  values in air from RT to  $400^{\circ}\text{C}$ . The  $\triangle$  symbol represents the  $\kappa(T)$  values in air from RT to  $400^{\circ}\text{C}$ . The black line represents the predicted values for heating, and the magenta line represents predicted values for cooling.

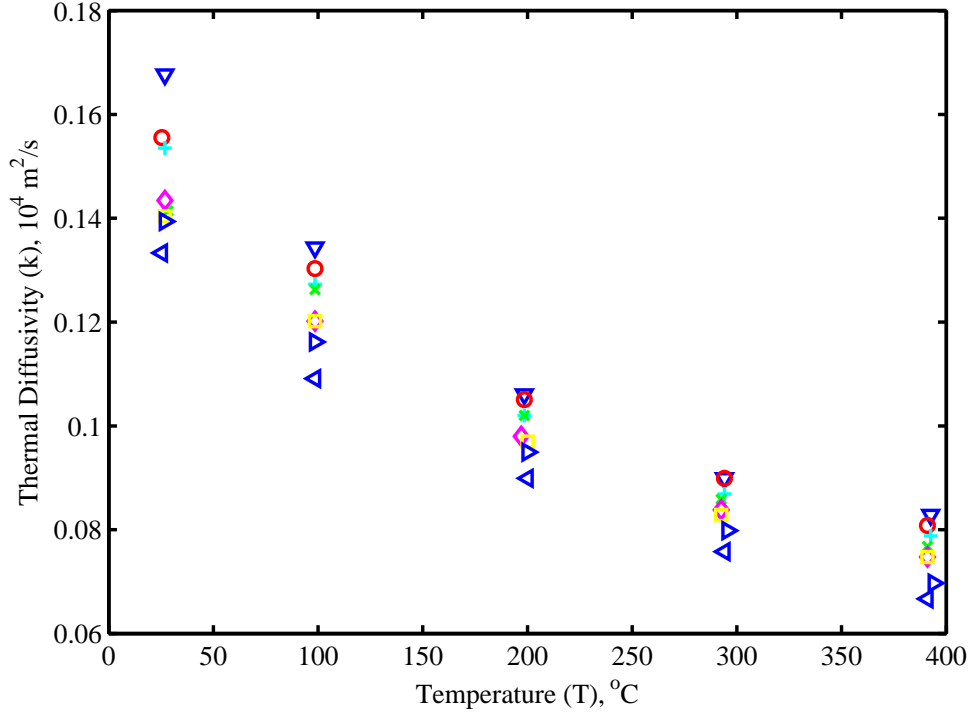


Figure 62: This figure contains the data sets of 8 disk samples cut from a 2-D  $\text{SiC}_f/\text{SiC}$  plate made from Hi-Nicalon type S fabric with a thin PyC fiber coating and an ICVI-SiC matrix [51].

In figure (4) the average calculated  $\kappa_{eff}$  values are shown for different fabrics. The relationship for Hi-Nicalon type S fabric of thermal conductivity ( $\kappa$ ) as a function of temperature ( $^{\circ}\text{C}$ ) can be described by the fifth order polynomial:

$$\begin{aligned} \kappa = & -1.456 \times 10^{-13}T^5 - 4.431 \times 10^{-10}T^4 + \\ & 5.005 \times 10^{-7}T^3 - 2.454 \times 10^{-4}T^2 + 2.992 \times 10^{-2}T + 26.601 \end{aligned} \quad (104)$$

The relationship for Tyranno SA fabric of thermal conductivity ( $\kappa$ ) as a function of temperature ( $^{\circ}\text{C}$ ) can be described by the fifth order polynomial:

$$\begin{aligned} \kappa = & 1.007 \times 10^{-13}T^5 - 4.431 \times 10^{-10}T^4 + \\ & 3.649 \times 10^{-7}T^3 - 1.908 \times 10^{-4}T^2 + 3.035 \times 10^{-2}T + 19.353 \end{aligned} \quad (105)$$

The relationship for Hi-Nicalon fabric of thermal conductivity ( $\kappa$ ) as function of temperature( $^{\circ}\text{C}$ ) can be described by the fifth order polynomial:

$$\begin{aligned} \kappa = & 1.266 \times 10^{-13}T^5 - 3.642 \times 10^{-10}T^4 + \\ & 3.925 \times 10^{-7}T^3 - 1.923 \times 10^{-4}T^2 + 3.417 \times 10^{-2}T + 12.381 \end{aligned} \quad (106)$$

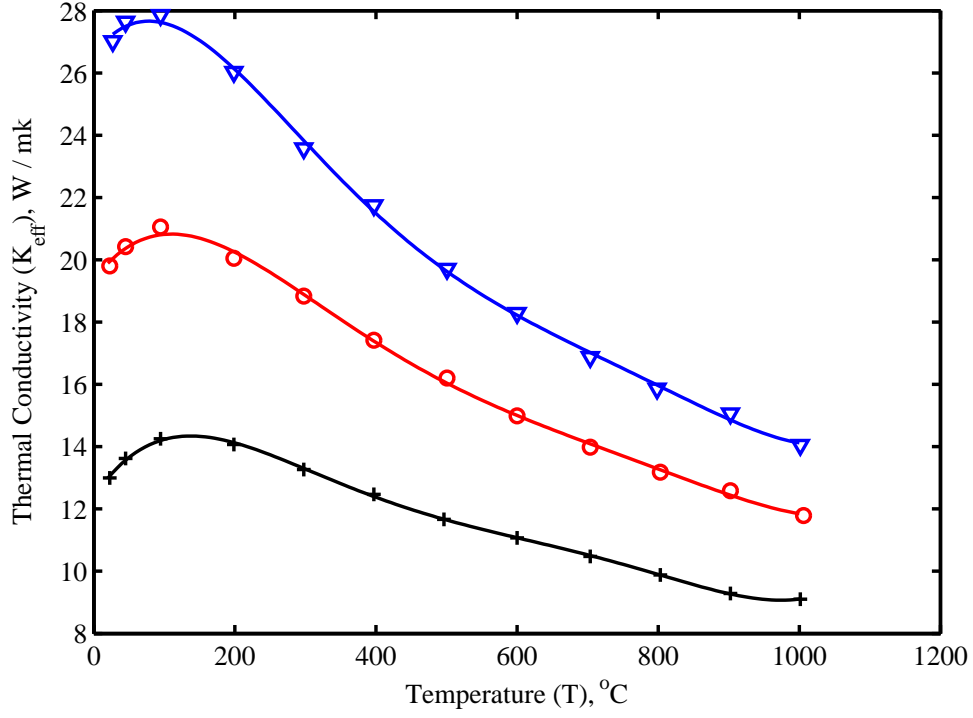


Figure 63: This data set shows the average  $\kappa_{eff}$  values calculated from the thermal diffusivity data shown in Figure (4) [51]. The  $\nabla$  symbol represents Hi-Nicalon type S fabric. The  $\circ$  symbol represents Tyranno SA fabric. The  $+$  symbol represents Hi-Nicalon fabric.

d

Table 4:

Systems	$D_f$ $\mu\text{ m}$	$\rho_f$ (g/cm <sup>3</sup> )	$t$ ( $\nu\text{m}$ )	$\rho_b$ (g/cm <sup>3</sup> )	$f_M$ (SEM)	$f_p$ (SEM)	$\epsilon$ (SEM)	$P_M$ (SEM)	Weave
Hi-Nicalon-1	13.8	2.74	0.110	2.597	0.294	0.650	0.17	0.107	PW
Hi-Nicalon-2	13.8	2.74	1.044	2.627	0.314	0.670	0.17	0.062	PW
Tyranno SA	10.0	3.02	0.190	2.667	0.262	0.577	0.12	0.105	PW
Hi-Nicalon S	12.0	3.00	0.188	2.710	0.173	0.502	0.17	0.065	5HS
Range	$\pm 1.8$	$\pm 0.02$	$\pm 0.04$	$\pm 0.02$	$\pm 0.07$	$\pm 0.06$	$\pm 0.05$	$\pm 0.007$	

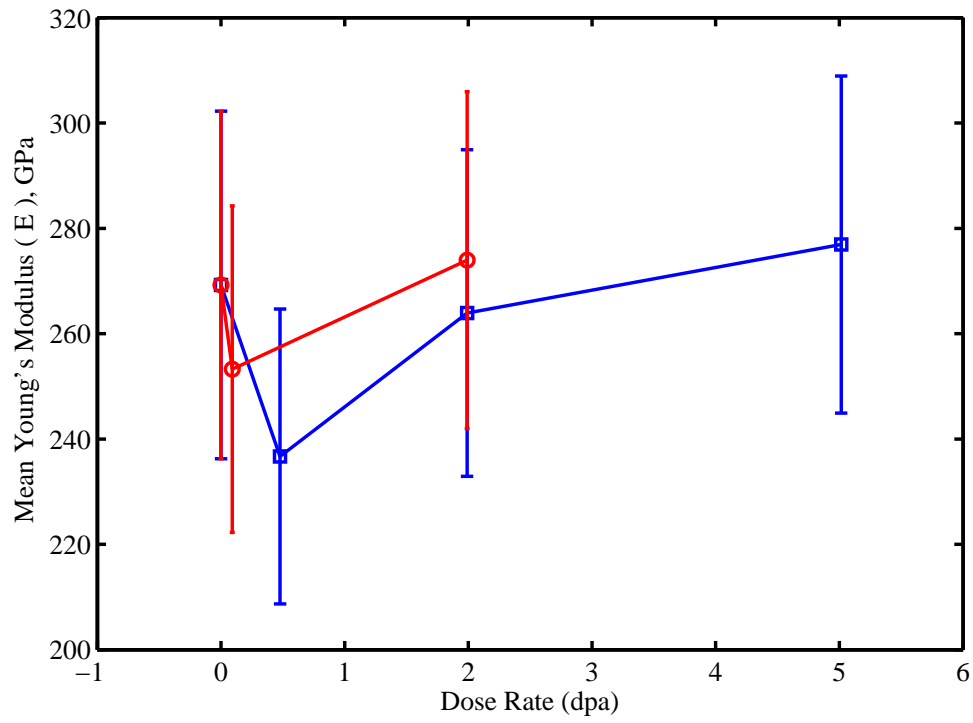


Figure 64: This data set depicts the Young's modulus for Hi-Nicalon fiber [41]. The error bars represent the 90% confidence limits for the Weibull distributed data. The  $\square$  symbol represents data for a 150 °C irradiation temperature [41], and the  $\circ$  symbol represents data for a 450 °C irradiation temperature.

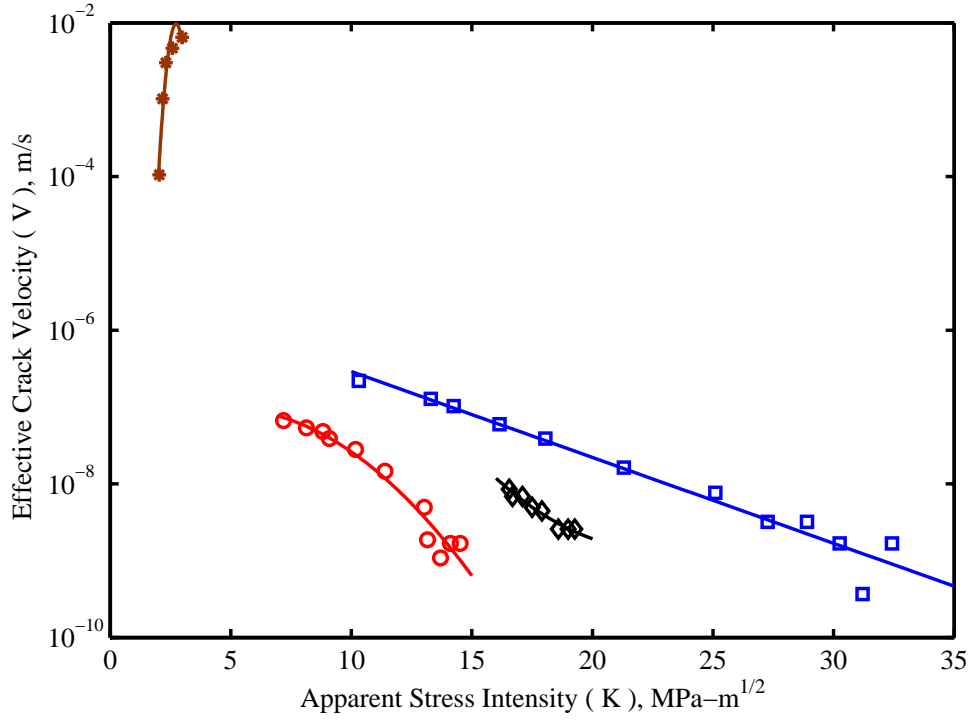


Figure 65: This data set compares the dependency of crack velocity on apparent stress intensity at 1373 °CK gettered in argon. The  $\circ$ C symbol represents the Hi-C sample. The  $\square$  symbol represents the CG-C150 sample. The  $\diamond$  sample represents the CG-C sample. The  $*$  sample represents the Monolithic silicon carbide.

In Figure (4), the dependency of crack velocity (m/s) on apparent stress intensity ( $\text{MPa}\cdot\text{m}^{\frac{1}{2}}$ ) is shown for four different samples. The relationship between crack velocity and stress intensity can be described by an equation, if you let  $y$  be the  $\log_{10}$  (effective crack velocity (m/s)) and  $x$  be the apparent stress intensity ( $\text{MPa}\cdot\text{m}^{\frac{1}{2}}$ ); Then the dependency of crack velocity on apparent stress intensity for Hi-C can be described by:

$$y = -0.021x^2 + 0.202x - 7.508 \quad (107)$$

The dependency of crack velocity on apparent stress intensity for CG-C150 can be described by:

$$y = -0.112x - 5.422 \quad (108)$$

The dependency of crack velocity on apparent stress intensity for CG-C can be described by:

$$y = 0.022x^2 - 0.982x + 2.202 \quad (109)$$

The dependency of crack velocity on apparent stress intensity for monolithic silicon carbide can be described by:

$$y = -3.669x^2 + 20.051x - 29.411 \quad (110)$$



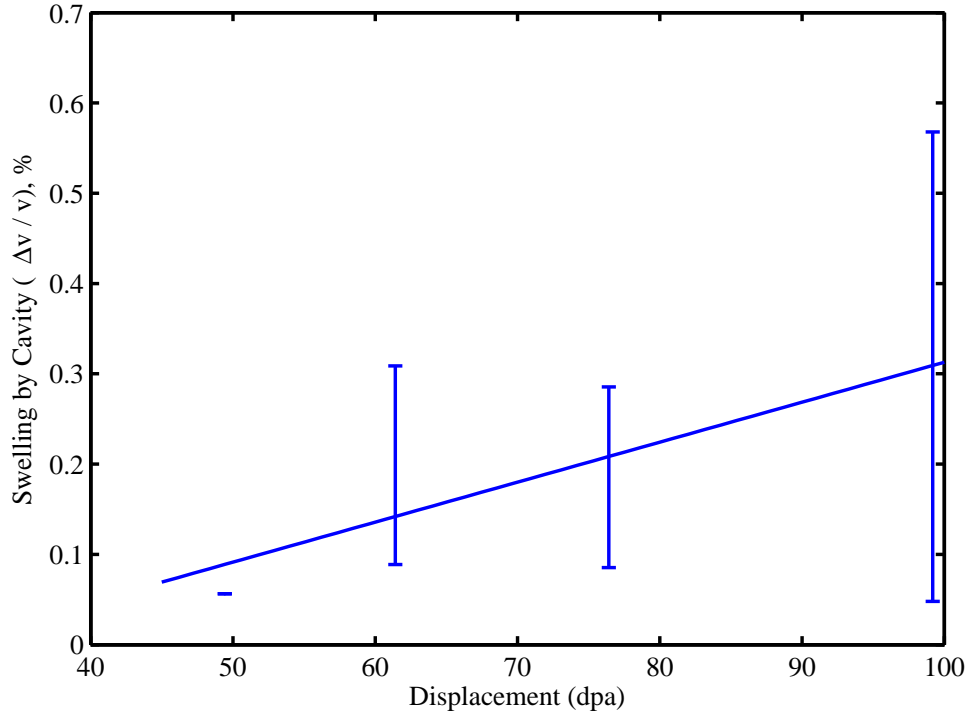


Figure 66: This data set depicts the swelling by helium cavity ( $\frac{\Delta V}{V}$ ) in matrix SiC irradiated at 1273K. [52]

The swelling by helium cavity ( $\frac{\Delta V}{V}$ ) in matrix SiC irradiated at 1273K as shown in Figure (4) can be described by:

$$\frac{\Delta V}{V} = 4.428 \times 10^{-3}(dpa) - 0.13 \quad (111)$$

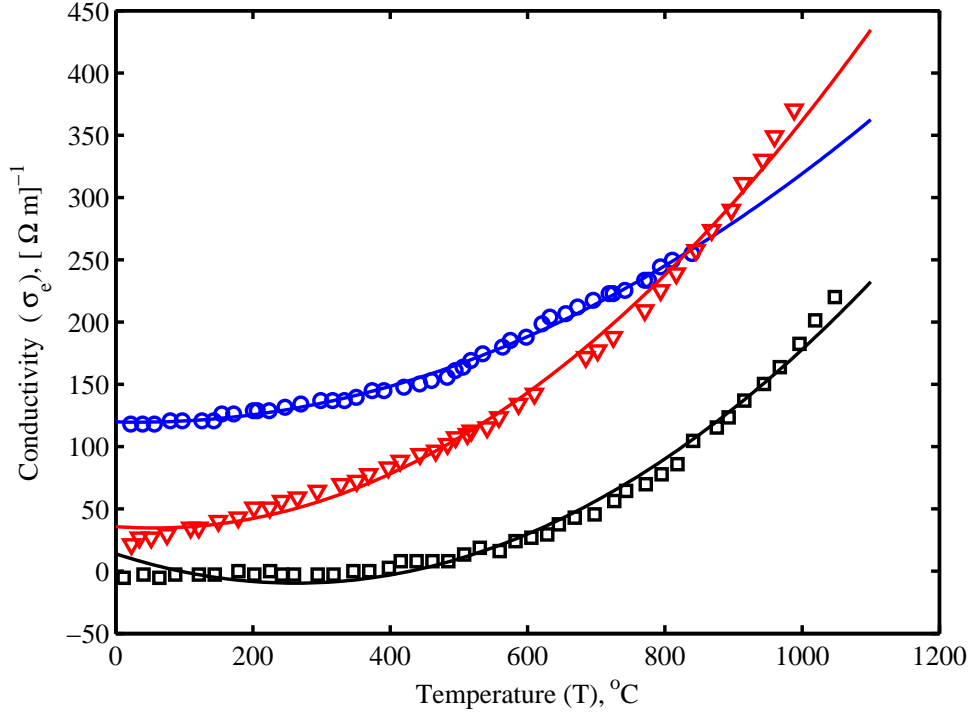


Figure 67: This data set depicts the conductivity of Nicalon type fibers under heating conditions. The  $\circ$  symbol represents CG-Nicalon type fibers. The  $\nabla$  symbol represents Hi-Nicalon type fibers. The  $\square$  symbol represents Type S fibers. [53] [54]

The conductivity of CG-Nicalon type fibers as shown in Figure (4) can be described by:

$$\sigma_e = 2.13 \times 10^{-4}T^2 - 1.377 \times 10^{-2}T + 119.89 \quad (112)$$

The conductivity of Hi-Nicalon type fibers as shown in Figure (4) can be described by:

$$\sigma_e = 3.665 \times 10^{-4}T^2 - 4.064 \times 10^{-2}T + 35.822 \quad (113)$$

The conductivity of Type S fibers as shown in Figure (4) can be described by:

$$\sigma_e = 3.442 \times 10^{-4}T^2 - 0.18T + 14.009 \quad (114)$$

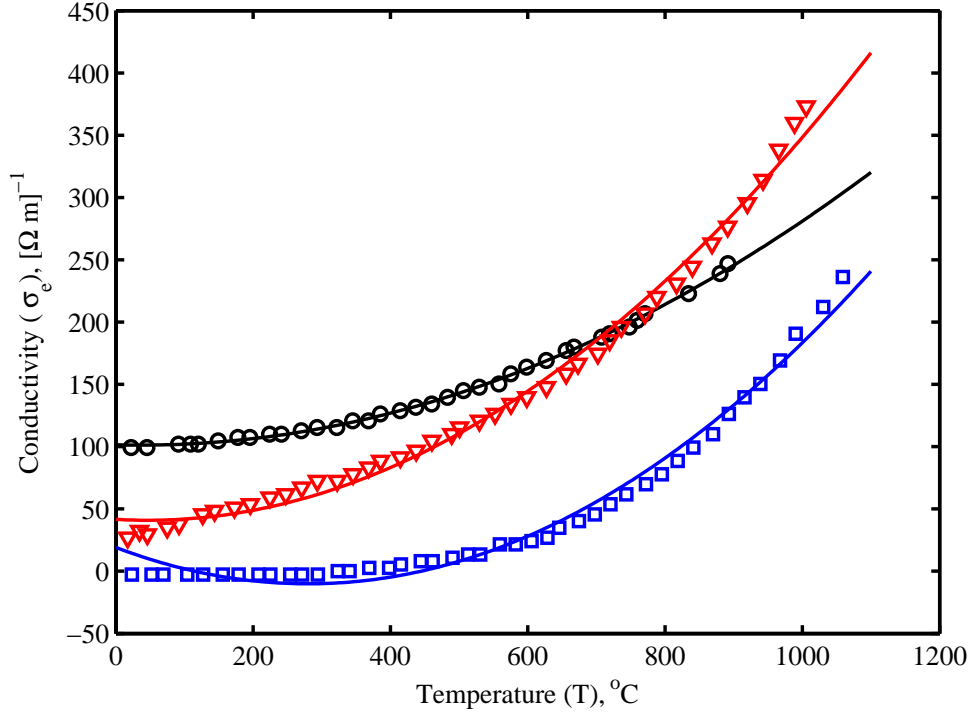


Figure 68: This data set depicts the conductivity of Nicalon type fibers under heating conditions. The  $\circ$  symbol represents CG-Nicalon type fibers. The  $\nabla$  symbol represents Hi-Nicalon type fibers. The  $\square$  symbol represents Type S fibers. [53] [54]

The conductivity of CG-Nicalon type fibers as shown in Figure (68) can be described by:

$$\sigma_e = 1.934 \times 10^{-4}T^2 - 1.382 \times 10^{-2}T + 101.49 \quad (115)$$

The conductivity of Hi-Nicalon type fibers as shown in Figure (68) can be described by:

$$\sigma_e = 3.378 \times 10^{-4}T^2 - 3.111 \times 10^{-2}T + 41.607 \quad (116)$$

The conductivity of Type S fibers as shown in Figure (68) can be described by:

$$\sigma_e = 3.73 \times 10^{-4}T^2 - 2.087 \times 10^{-1}T + 19.07 \quad (117)$$

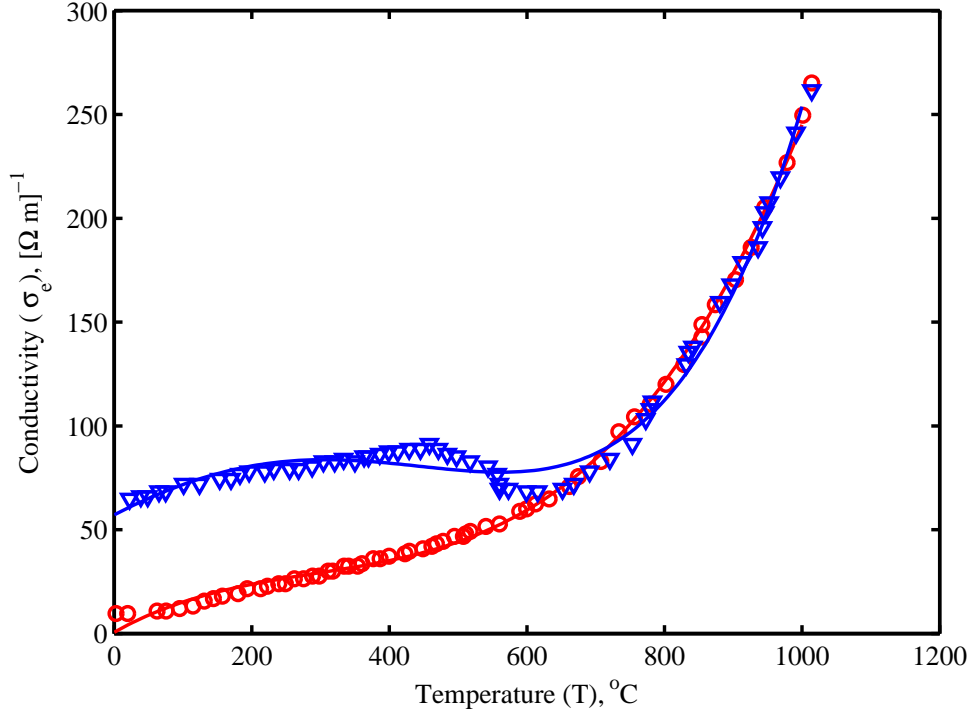


Figure 69: This figure depicts the electrical conductivity of Tyranno SA fibers. The red  $\circ$  symbol represents cooling conditions, while the blue  $\nabla$  represents heating conditions. [54]

The electrical conductivity of Tyranno SA fibers under cooling conditions as shown in Figure (69) can be described by:

$$\sigma_e = 6.829 \times 10^{-10}T^3 - 4.526 \times 10^{-4}T^2 + 1.855 \times 10^{-1}T + 6.114 \times 10^{-1} \quad (118)$$

The electrical conductivity of Tyranno SA fibers under heating conditions as shown in Figure (69) can be described by:

$$\sigma_e = 6.829 \times 10^{-10}T^4 - 4.661 \times 10^{-7}T^3 - 1.888 \times 10^{-4}T^2 + 1.686 \times 10^{-1}T + 57.165 \quad (119)$$

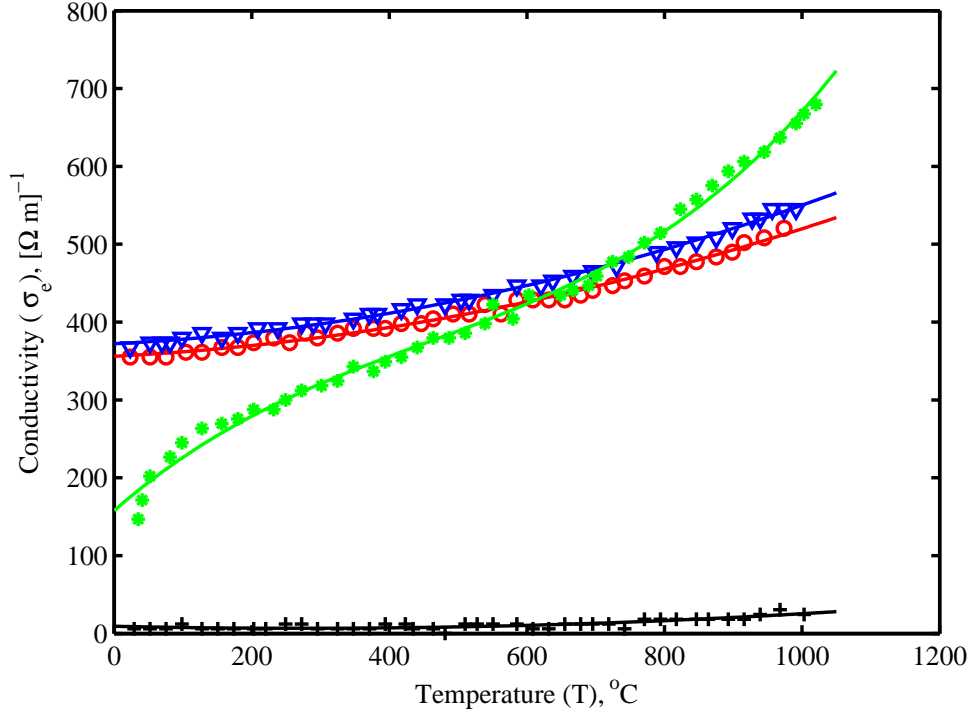


Figure 70: This figure depicts the electrical conductivity of various composites. The  $\circ$  symbol represents the conductivity of 2D SEP CG Nicalon, the  $\nabla$  symbol represents the conductivity of 3D SEP CG Nicalon, the  $+$  symbol represents 2D PIP CG Nicalon, the  $*$  symbol represents 2D SEP Hi Nicalon.

The electrical conductivity of 2D SEP CG Nicalon as shown in Figure (70) can be described by:

$$\sigma_e = 1.184 \times 10^{-4}T^2 + 4.529 \times 10^{-2}T + 356.12 \quad (120)$$

The electrical conductivity of 3D SEP CG Nicalon as shown in Figure (70) can be described by:

$$\sigma_e = 1.333 \times 10^{-4}T^2 + 4.462 \times 10^{-2}T + 372.21 \quad (121)$$

The electrical conductivity of 2D PIP CG Nicalon as shown in Figure (70) can be described by:

$$\sigma_e = 3.546 \times 10^{-5}T^2 - 1.937 \times 10^{-2}T + 9.312 \quad (122)$$

The electrical conductivity of 2D SEP Hi Nicalon as shown in Figure (70) can be described by:

$$\sigma_e = 7.298 \times 10^{-7}T^3 - 9.916 \times 10^{-4}T^2 + 7.747 \times 10^{-1}T + 157.89 \quad (123)$$

	CG-Nicalon	Hi-Nicalon	Hi-Nicalon type S	Dow Sylramic	Bulk SiC
Diameter ( $\mu\text{m}$ )	14	12-14	12	10	—
Tensile strength (GPa)	2.0-3.0	2.8-3.4	2.6-2.7	2.8-3.4	0.1
Elastic modulus (GPa)	170-220	270	420	390-400	460
Density ( $\text{g}/\text{cm}^3$ )	2.55	2.74	2.98-3.10	3.0-3.1	3.25
Coefficient of thermal expansion ( $10^{-6}/\text{K}$ )	3.2	3.5	—	5.4	4.0
Thermal conductivity at 20°C ( $\text{W}/\text{m}\cdot\text{K}$ )	1.5	4	18	40-45	100-350
Oxygen content (wt%)	11.7	0.5	0.2	0.8	0.0
C/Si atomic ratio	1.31	1.39	1.05	1.0	1.0

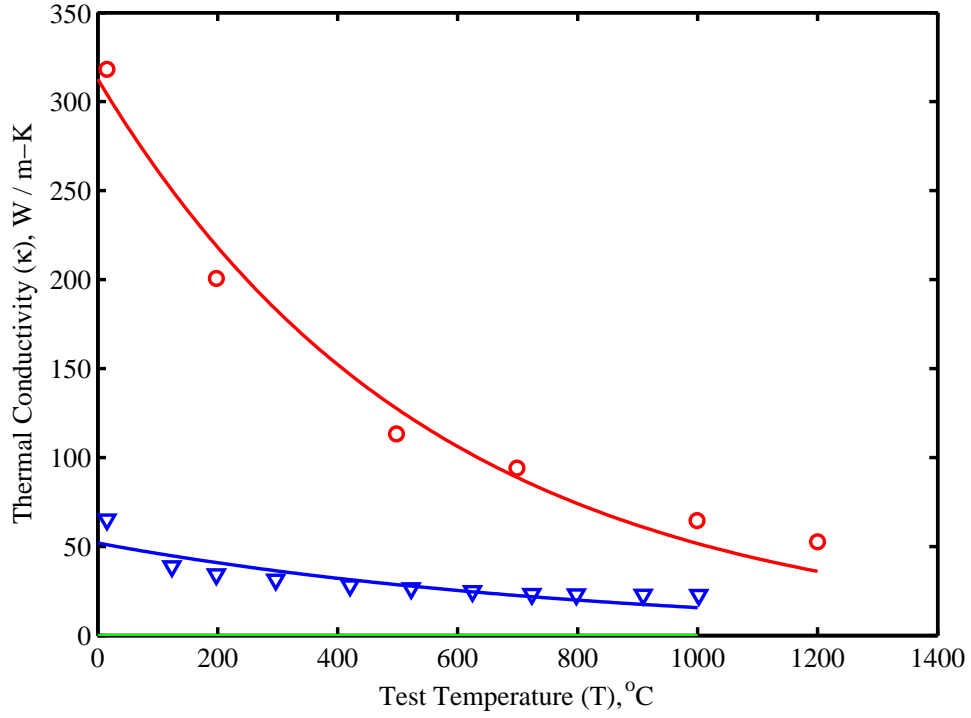


Figure 71: This figure compares the transverse thermal conductivity of monolithic CVD SiC and two grades of SiC/SiC composites [39][55]. The  $\circ$  symbol represents CVD SiC. The  $\nabla$  symbol represents CVR SiC/SiC. The green line represents CVI SiC/SiC (baseline).

The thermal conductivity of CVD SiC as shown in Figure (71) can be described by the exponential equation:

$$k = 312.7209 \times \exp(-0.0018 \times T) \quad (124)$$

The thermal conductivity of CVR SiC/SiC as shown in Figure (71) can be described by the exponential equation:

$$k = 51.951 \times \exp(-0.0012 \times T) \quad (125)$$

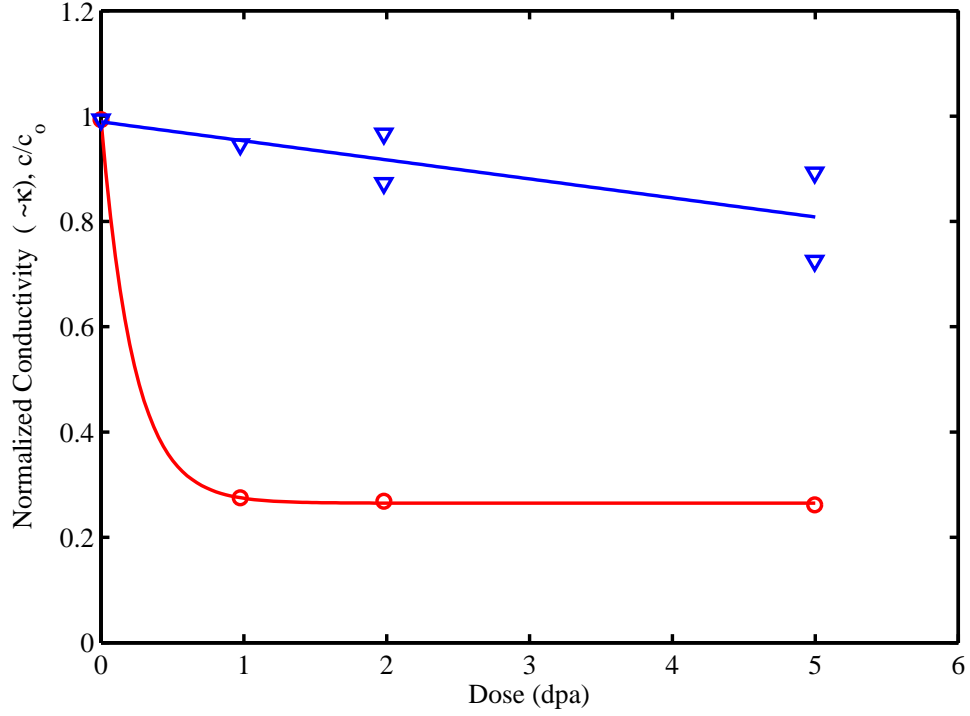


Figure 72: This figure shows the normalized electrical and thermal conductivity plotted versus the irradiation dose ( $1\text{dpa} = 10^{25} \text{ n m}^{-2}$ ). The samples were irradiated in HFR Petten. The  $\circ$  symbol represents the thermal conductivity, and the  $\nabla$  symbol represents the electrical conductivity.

The normalized thermal conductivity as shown in Figure (72) can be described by the exponential equation:

$$\tilde{k} = 0.265 + 0.728 * \exp(-4.371 * d) \quad (126)$$

The normalized electrical conductivity as shown in Figure (72) can be described by the linear equation:

$$\tilde{k} = -3.615 \times 10^{-2}d + 0.893 \quad (127)$$



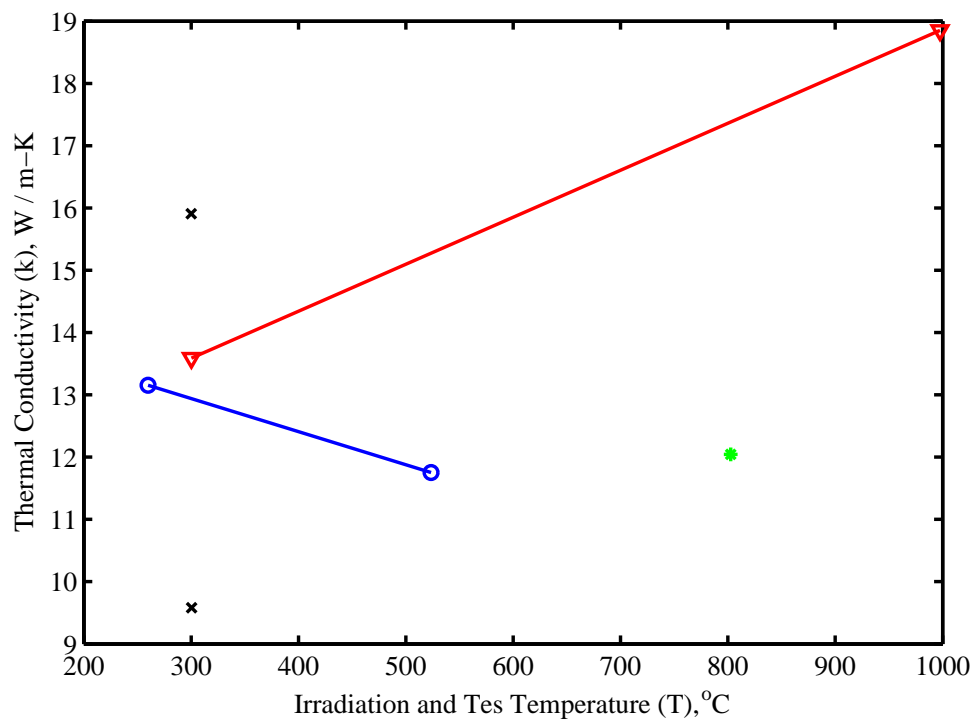


Figure 73: Effect of neutron irradiation on the thermal conductivity of bulk SiC [41] [42] [43] [44]. The studies in refs [42] [43] [44] were performed on samples irradiated to 25-43 dpa, whereas the data by [41] were obtained on samples irradiated to 0.1 dpa.

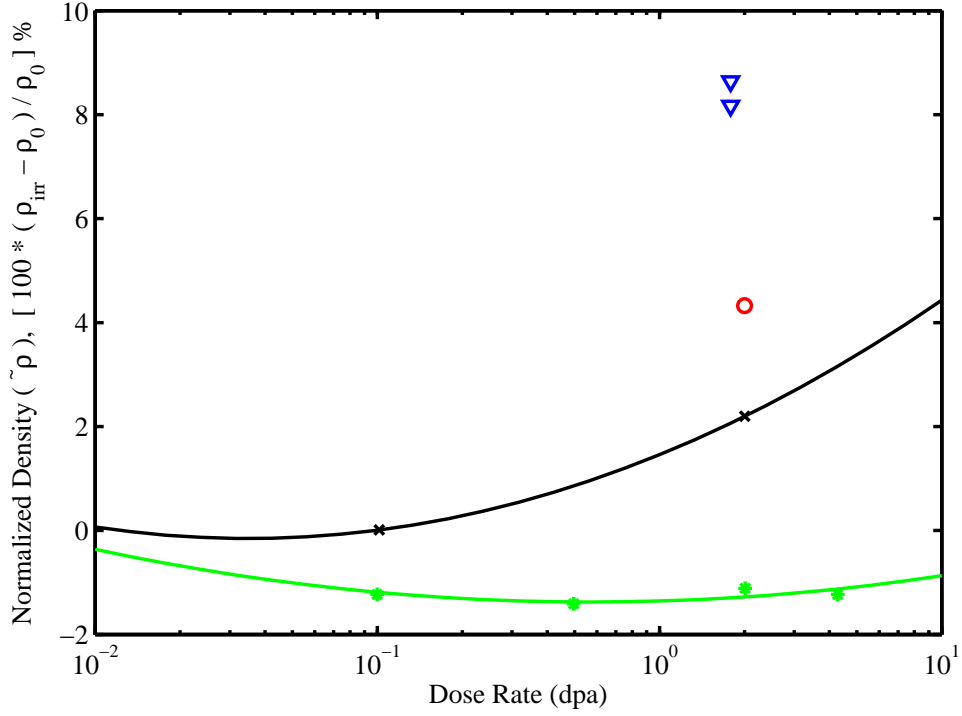


Figure 74: Comparison of the effect of low-dose irradiation at 500-650°C on the density of SiC and SiC-based fibers [56][41][44][57]

The normalized density ( $\tilde{\rho}$ ) as a function of dpa for Hi-Nicalon, at 550°C can be expressed by letting  $x_L = \log_{10}(dpa)$  in the equation:

$$\tilde{\rho} = 0.759x_L^2 + 2.213x_L + 1.459 \quad (128)$$

The normalized density ( $\tilde{\rho}$ ) as a function of dpa for CVD SiC, at 500°C to 550°C can be expressed by letting  $x_L = \log_{10}(dpa)$  in the equation:

$$\tilde{\rho} = 0.328x_L^2 + 0.159x_L - 1.357 \quad (129)$$

The electrical conductivity (S/m) of CVD SiC (irradiated and non-irradiated) at 22°C as a function of dose rate (Gy/s) can be represented by letting  $Y = \log_{10}$  (Electrical Conductivity) and letting  $X = \log_{10}$  (Dose Rate) in the equation:

$$Y = 4.069 \times 10^{-2}X + 2.245 \quad (130)$$

A direct form of the relationship is given by:

$$\sigma_e = 175.79\phi_\gamma^{0.041} \quad (131)$$

The electrical conductivity (S/m) of Nicalon (irradiated) as a function of dose rate (Gy/s) can be represented by letting  $Y = \log_{10}$  (Electrical Conductivity) and letting  $X$

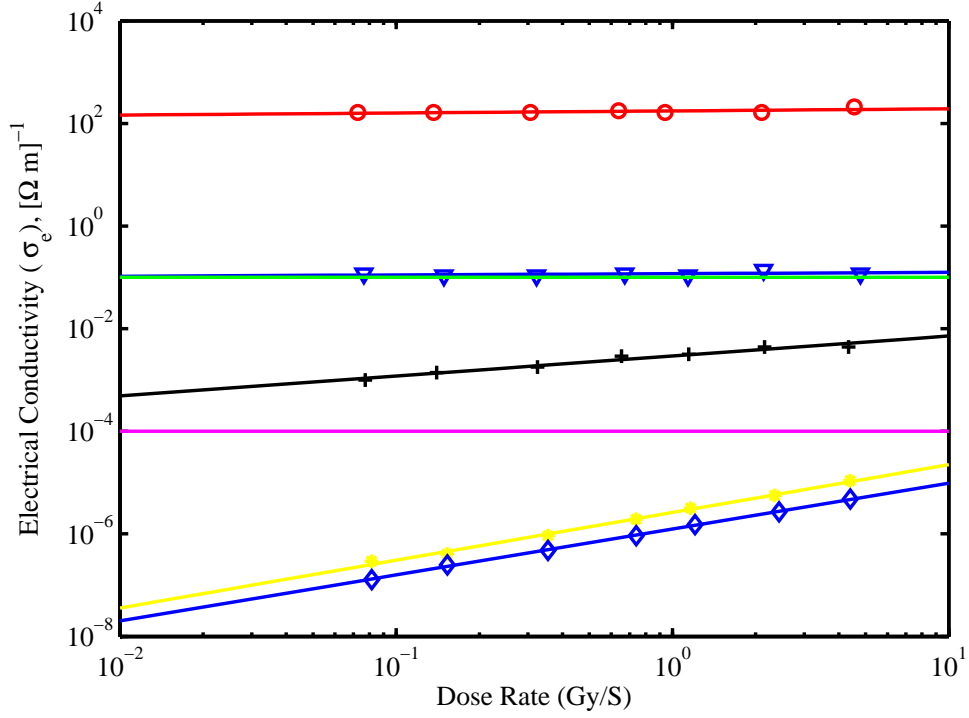


Figure 75: Radiation enhanced conductivity of select monolithic SiC [58]

$= \log_{10} (\text{Dose Rate})$  in the equation:

$$Y = 2.495 \times 10^{-2}X - 0.928 \quad (132)$$

A direct form of the relationship is given by:

$$\sigma_e = 0.118\phi_\gamma^{0.025} \quad (133)$$

The electrical conductivity (S/m) of Nicalon (non-irradiated) as a function of dose rate (Gy/s) can be represented by letting  $Y = \log_{10} (\text{Electrical Conductivity})$  and letting  $X = \log_{10} (\text{Dose Rate})$  in the equation:

$$Y = -2.483 \times 10^{-17}X - 1 \quad (134)$$

A direct form of the relationship is given by:

$$\sigma_e \approx 0.1 \quad (135)$$

The electrical conductivity (S/m) of Hexoloy  $\alpha$  SiC irradiated at 22°C as a function of dose rate (Gy/s) can be represented by letting  $Y = \log_{10} (\text{Electrical Conductivity})$  and letting  $X = \log_{10} (\text{Dose Rate})$  in the equation:

$$Y = 0.389X - 2.533 \quad (136)$$

A direct form of the relationship is given by:

$$\sigma_e = 2.93 \times 10^{-3} \phi_\gamma^{0.389} \quad (137)$$

The electrical conductivity (S/m) of Hexoloy (non-irradiated) as a function of dose rate (Gy/s) can be represented by letting  $Y = \log_{10}$  (Electrical Conductivity) and letting  $X = \log_{10}$  (Dose Rate) in the equation:

$$Y = -9.93 \times 10^{-17} X - 5.583 \quad (138)$$

A direct form of the relationship is given by:

$$\sigma_e \approx 0.1 \quad (139)$$

The electrical conductivity (S/m) of Kyocera  $\beta$  SiC irradiated at 200°C as a function of dose rate (Gy/s) can be represented by letting  $Y = \log_{10}$  (Electrical Conductivity) and letting  $X = \log_{10}$  (Dose Rate) in the equation:

$$Y = 0.931X - 5.583 \quad (140)$$

A direct form of the relationship is given by:

$$\sigma_e = 2.612 \times 10^{-6} \phi_\gamma^{0.931} \quad (141)$$

The electrical conductivity (S/m) of Kyocera  $\beta$  SiC at 22°C as a function of dose rate (Gy/s) can be represented by letting  $Y = \log_{10}$  (Electrical Conductivity) and letting  $X = \log_{10}$  (Dose Rate) in the equation:

$$Y = 0.895X - 5.906 \quad (142)$$

A direct form of the relationship is given by:

$$\sigma_e = 1.241 \times 10^{-6} \phi_\gamma^{0.895} \quad (143)$$

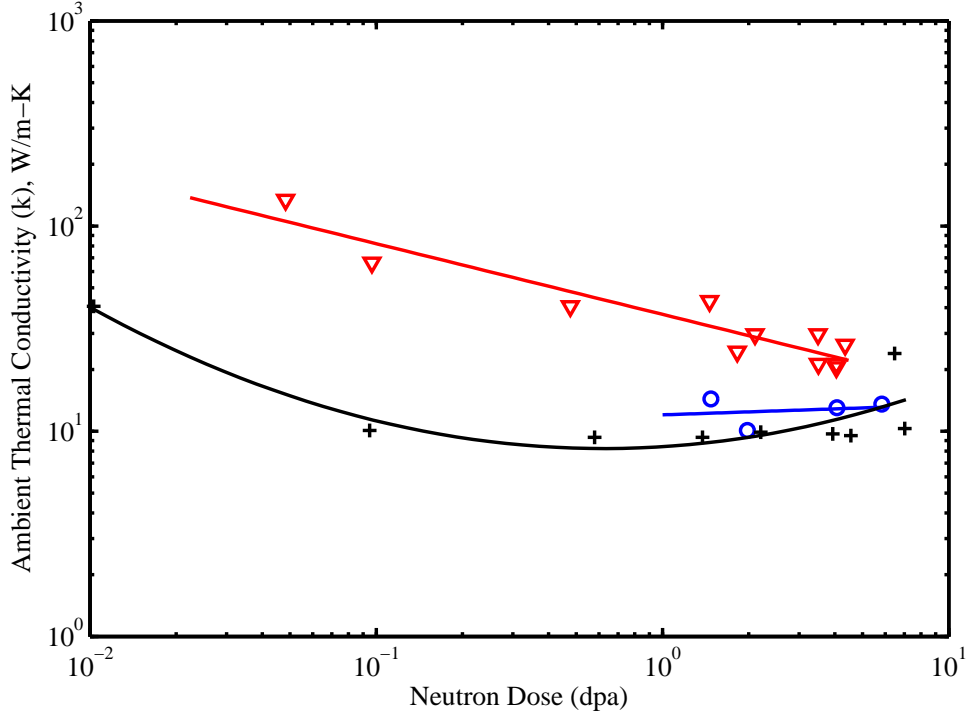


Figure 76: This figure depicts the room temperature thermal conductivity ( $k$ ) of CVD SiC as a function of neutron dose (dpa) and irradiation temperature [58][59].

The room temperature thermal conductivity ( $k$ ) of Rohm Haas CVD SiC as a function of neutron dose (dpa) and irradiated at 800°C can be represented by letting  $Y = \log_{10}(k)$  and letting  $X = \log_{10}(\text{dpa})$  in the equation:

$$Y = -0.345X + 1.57 \quad (144)$$

A direct form of this equation is given by:

$$k = 37.154 \times (\text{dpa})^{-0.345} \quad (145)$$

The room temperature thermal conductivity ( $k$ ) of Rohm Haas CVD SiC as a function of neutron dose (dpa) and irradiated at 500°C can be represented by letting  $Y = \log_{10}(k)$  and letting  $X = \log_{10}(\text{dpa})$  in the equation:

$$Y = 0.048X + 1.08 \quad (146)$$

A direct form of this equation is given by:

$$k = 12.023 \times (\text{dpa})^{0.048} \quad (147)$$

The room temperature thermal conductivity ( $k$ ) of Rohm Haas CVD SiC as a function of neutron dose (dpa) and irradiated at 300°C can be represented by letting  $Y = \log_{10}(k)$

(k) and letting  $X = \log_{10}(\text{dpa})$  in the equation:

$$Y = 0.214X^2 + 0.088X + 0.925 \quad (148)$$

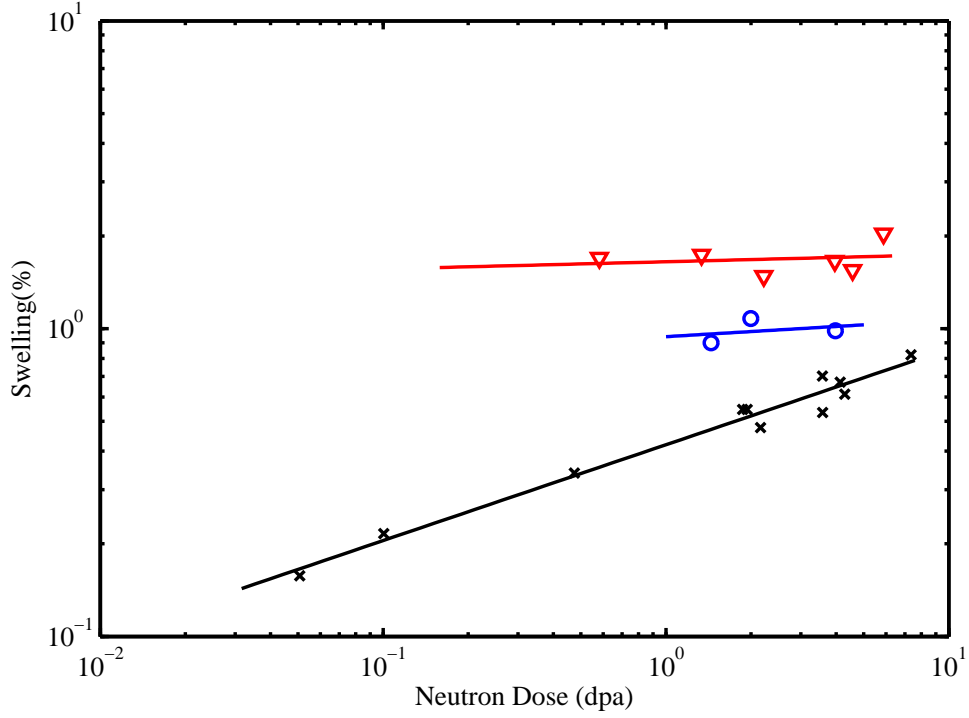


Figure 77: This figure depicts the room temperature swelling (%) of CVD SiC as a function of neutron dose (dpa) and irradiation temperature [58].

The room temperature swelling (%) of Rohm Haas CVD SiC as a function of neutron dose (dpa) and irradiated at 300°C can be represented by  $Y = \log_{10} (\%)$  and letting  $X = \log_{10}(\text{dpa})$  in the equation:

$$Y = 0.023X + 0.217 \quad (149)$$

A direct form of this equation is given by:

$$\frac{\delta v}{v} = 1.648 \times (\text{dpa})^{0.023} \quad (150)$$

The room temperature swelling (%) of Rohm Haas CVD SiC as a function of neutron dose (dpa) and irradiated at 300°C can be represented by  $Y = \log_{10} (\%)$  and letting  $X = \log_{10}(\text{dpa})$  in the equation:

$$Y = 0.055X - 0.026 \quad (151)$$

A direct form of this equation is given by:

$$\frac{\delta v}{v} = 0.942 \times (\text{dpa})^{0.055} \quad (152)$$

The room temperature swelling (%) of Rohm Haas CVD SiC as a function of neutron dose (dpa) and irradiated at 300°C can be represented by  $Y = \log_{10} (\%)$  and letting  $X$

$= \log_{10}(\text{dpa})$  in the equation:

$$Y = 0.311X - 0.377 \quad (153)$$

A direct form of this equation is given by:

$$\frac{\delta v}{v} = 0.419 \times (dpa)^{0.311} \quad (154)$$



## A Ashbys' Design Correlations[60]

### A.1 Mechanical Properties

Compressive Strength (MPa),  $\sigma_c$  is given by:

$$\sigma_c = (0.1 - 1.0)\sigma_{c,s} \times \left(\frac{\rho}{\rho_s}\right)^{3/2} \quad (155)$$

Young's modulus (GPa),  $E$

$$E = (0.1 - 4)E_s \left(\frac{\rho}{\rho_s}\right)^2 \quad (156)$$

Shear modulus (GPa),  $G$

$$G \approx \frac{3}{8} \left(\frac{P}{P_s}\right) \quad (157)$$

Bulk modulus (GPa),  $K$

$$K \approx \frac{3}{8} \left(\frac{P}{P_s}\right) \quad (158)$$

Flexural Modulus (GPa),  $E_f$

$$E_f \approx E \left(\frac{P}{P_s}\right) \quad (159)$$

Poisson's ratio,  $\nu$

$$0.32 - 0.34 \quad (160)$$

Compressive strength (MPa),  $\sigma_c$

$$\sigma_c = (0.1 - 1.0)\sigma_{c,s} \left(\frac{\rho}{\rho_s}\right)^2 \quad (161)$$

Tensile strength (MPa),  $\sigma_c$

$$\sigma_f \approx (1.1 - 1.4)\sigma_c \quad (162)$$

Endurance limit (MPa),  $\sigma_e$

$$\sigma_e \approx (0.5 - 0.75)\sigma_c \quad (163)$$

Densification strain,  $\epsilon_D$

$$\epsilon_D = (0.9 - 1.0) \times \left(1 - 1.14 \frac{\rho}{\rho_s} + 0.4 \left(\frac{\rho}{\rho_s}\right)^3\right) \quad (164)$$

Loss coefficient,  $\eta$

$$\eta \approx (0.95 - 1.05) \times \frac{\eta_s}{(\rho/\rho_s)} \quad (165)$$

Hardness (MPa), H

$$H = \sigma_c(1 + 2\frac{\rho}{\rho_s}) \quad (166)$$

Initiation toughness (J/m<sup>2</sup>)J<sub>IC</sub>

$$J_{IC} \approx \beta\sigma_{y,s}\ell(\frac{\rho^*}{\rho_s})^p \quad (167)$$

## A.2 Thermal Properties

Thermal Conductivity (W/m.K), k

$$(\frac{\rho}{\rho_s})^{1.8} < \frac{k}{k_s} < (\frac{\rho}{\rho_s})^{1.65} \quad (168)$$

## A.3 Electrical Properties

Resistivity (10<sup>-8</sup> ohm.m), R

$$(\frac{\rho}{\rho_s})^{-1.6} < \frac{R}{R_s} < (\frac{\rho}{\rho_s})^{-1.85} \quad (169)$$

## References

- [1] R.G. Munro. Material properties of a sintered alpha-sic. *J. Phys. Chem. Ref. Data.*, 26(5):1195–1203, 1997.
- [2] Z. Li and R.C. Bradt. *J. Am. Ceram. Soc.*, 69:863, 1986.
- [3] N.L. Hecht, G.A. Graves, D.E. McCullum, A.P. Berens, S. Goodrich, J.D. Wolf, J.R. Hoenigman, P. Yancy, D. Grant, and S. Hilton. Evaluation of environmental effects in toughened ceramics for advanced heat engines, investigation of selected sic and si and si ceramics. Technical Report ORNL/Sub/84-00221/2, Oak Ridge National Laboratory, 1990.
- [4] D.J. Green, J.R. Hellman, and M.F. Modest. Physical property measurements of high temperature composites. In J.R. Hellman and B.K. Kennedy, editors, *Projects Within The Center for Advanced Materials. December 1, 1989 to February 28, 1990*, pages 71–90. Pennsylvania State University Press, 1990.
- [5] 'C.H. McMurty, W.D.G. Boeker, S.G Seshadri, J.S. Zanghi, and J.E. Garnier'. *Am. Cer. Soc. Bull.*, 66:352, 1987.
- [6] N. L. Hecht, S. M. Goodrich, L. Chuck, D. E. McCullum, and V. J. Tenner. *Am. Cer. Soc. Bull.*, 71:653, 1992.
- [7] C.A. Tracy and G.D. Quinn. *Ceramic Engineering Science Project*, 15:837, 1994.
- [8] E.H. Kraft and G.I. Dooher. Mechanical response of high performance silicon carbide. *Carborundum Company, Research and Development Division*, August 1976.
- [9] P.F. Becher. *Journal of Material Science*, 19:2805, 1984.
- [10] A. Ghosh, M.G. Jenkins, K.W. White, A.S. Kobayashi, and R.C. Bradt. *J. Am. Ceram. Soc.*, 72:242, 1989.
- [11] J.L Smialek and N.S. Jacobson. *Journal of American Ceramics Society*, 69:741, 1986.
- [12] F.F. Lange. *Journal of American Ceramic Society*, 53:290, 1970.
- [13] G. Orange, H. Tanaka, and G. Fantozzi. *Ceram Interr.*, 13:159, 1987.
- [14] Q. Zhang and S Chou. *Journal of Inorganic Material*, 1986.

- [15] D.E. McCullum, N.L. Hecht, L. Chuck, and S.M. Goodrich. *Ceram. Eng. Sci. Proc.*, 12:1886, 1991.
- [16] K.D. McHenry and R.E. Tressler. *Journal of American Ceramic Society*, 63:152, 1980.
- [17] M. Srinivasan and S.G. Seshadri. *Fracture Mechanics for Ceramics, Rocks, and Concrete*, chapter Application of Single Edge Notched Beam and Indentation Techniques to Determine Fracture Toughness of Alpha Silicon Carbide, pages 46–48. American Society for Testing and Materials, 1981.
- [18] T.E. Easter, R.C. Bradt, and R.E. Tressler. *Journal of American Ceramic Society*, 64:731, 1981.
- [19] K.T. Faber and A.G. Evans. *Journal of American Ceramics Society*, 66:C–94, 1983.
- [20] J.E. Lane, C.H. Carter Jr., and R.F. Davies. *Journal of American Ceramic Society*, 71:281, 1988.
- [21] J.C Conway Jr., J.J. Mecholsky Jr., S.M. Wiederhorn, O.M. Jadaan, D.L. Shellman, and D.C. Cramer. *Projects Within the Center for Advanced Materials, 1 September 1989 to 30 November 1989*, chapter Test Methodology for Tubular Components, pages 141–160. Pennsylvania State University Press, 1989.
- [22] S.M. Wiederhorn, D.C. Crammer, and Jr. R.F. Krause. *Projects Within the Center for Advanced Materials, CAM-9002, GRI-90/0205*, chapter Test Methodology for Tubular Components, pages 333–360. Pennsylvania State University Press, 1991.
- [23] R.L. Allor and S. Jahanmir. *American Ceramic Society Bulletin*, 75:40, 1996.
- [24] E. Rabinowicz. *Prod. Eng.*, 19:71, 1958.
- [25] S.M. Hsu, D.S. Lim, Y.S. Wang, and R.G. Munro. *Lubr Eng.*, 1991.
- [26] X. Dong, S. Jahanmir, and L.K Ives. *Trib. Inter.*, 28:559, 1995.
- [27] C.S. Yust and F.J. Carignan. *ASLE Trans.*, 28:245, 1984.
- [28] M.G. Gee, C.S. Matharu, E.A Almond, and T.S. Eyre. *Wear*, 138:169, 1990.
- [29] J. Denape and J. Lamon. *Journal of Material Science*, 25:3592, 1990.
- [30] Engineering property data on selected ceramics. vol. 2 ceramics. Technical report, Columbus, OH, 1979.
- [31] R. Morrel. Handbook of properties of technical and engineering ceramics, part 1: An introduction for the engineer and designer. Technical report, 1985.
- [32] Y. Fujisawa, K Matsusue, and K. Takahara. *J. Soc. Mater. Sci. Jpn.*, 35:1112, 1986.

- [33] P.T.B. Shaffer. *Engineered Materials Handbook, Vol. 4, Ceramics and Glasses*, volume 4, chapter Engineering Properties of Carbides, pages 804–811. Asm International, 1991.
- [34] M.E. Schlesinger. *Engineered Materials Handbook, Vol. 4, Ceramics and Glasses*, volume 4, chapter Melting Points, Crystallographic Transformation, and Thermodynamic Values, pages 883–891. Asm International, 1991.
- [35] C.H. McMurtry, W.D.G Boecker, S.G. Seshadri, J.S. Zanghi, and J.E. Garnier. *Am. Ceram. Soc. Bull.*, 66:325, 1987.
- [36] E.H. Kraft and J.A. Coppola. Thermo-mechanical properties of sintered alpha silicon carbide. Technical report, Carborundum Company, March 1977.
- [37] J.R. Hellman, D.J. Green, and M.F. Modest. *Projects Within the Center for Advanced Materials, September 1, 1990 to November 30, 1990*, chapter Physical Property Measurements of High Temperature Composites, pages 75–87. Pennsylvania State University Press, 1990.
- [38] Final report on poisson’s ratio and cte determinations. Technical Report 2005, EMTL, 1998.
- [39] Morton product literature, 1995.
- [40] W.Kowbel, K.T. Tsou, J.C. Withers, and G.E. Youngblood. Fusion materials semi-annual progress report. Technical report, DOE/ER-0313/23, DEC 31 1997.
- [41] L.L. Snead et al. *Journal of Nuclear Materials*, page 253, 1998.
- [42] D.J. Senior, G.E. Youngblood, C.E. Moore, D.J. Trimble, G.A. Newsome, and J.J. Woods. *Fusion Technology*, 30(943), 1996.
- [43] G.E. Youngblood and R.H. Jones. Fusion materials semiannual progress report. Technical report, Oak Ridge National Lab, December 1997.
- [44] G.W. Hollenberg et al. *Journal of Nuclear Materials Semiannual Progress Report*, 70:219, 1995.
- [45] R. Blackstone and E.H. Voice. *Journal of Nuclear Materials*, 35:319, 1977.
- [46] R. Price. *Nucl. Tech.*, 35:320, 1977.
- [47] G.E. Youngblood and D.J. Senior. Effects of irradiation and post-irradiation annealing on the thermal conductivity/diffusivity of monolithic sic and f-sic/sic composites. *Journal of Nuclear Materials*, pages 507–512, 2004.
- [48] R.P. Thorn, V.C. Howard, and B. Hope. *Proceedings of the British Ceramic Society*, 7:449, 1995.

- [49] M. Rohde. *Journal of Nuclear Materials*, 182:87, 1991.
- [50] D.J. Senior, G.E. Youngblood, L.R. Greenwood, D.V. Archer, D.L. Alexander, M.C. Chen, and G.A. Newsome. *Journal of Nuclear Materials*, 317:145, 2003.
- [51] G.E. Youngblood, David J. Senior, and Russel H. Jones. Modeling the transverse thermal conductivity of 2-d sic<sub>f</sub>/sic composites made with woven fabric. *Fusion Science and Technology*, 45:583–591, 2004.
- [52] H. Kishimoto, Y. Katoh, and A. Kohyama. Microstructural stability of sic and sic/sic composites under high temperature irradiation environment. *Journal of Nuclear Materials*, 307-311:1130–1134, 2002.
- [53] C. Vahlas, P. Rocabois, and C Bernard. *Journal of Material Science*, 29:5839, 1994.
- [54] R. Scholz, F. dos Santos Marques, and B Riccardi. Electrical conductivity of silicon carbide composites and fibers. *Journal of Nuclear Materials*, 307-311:1098–1101, 2002.
- [55] W. Kowbel, K.T. Tsou, J.C. Withers, and G.E. Youngblood. Fusion materials semiann. prog. rep. page 172, Dec 1997. DOE/ER-0313/23.
- [56] M.C. Osborne. Ph.d thesis. *Rensselaer Polytechnic Institute*, 1997. Materials Science and Engineering Dept.
- [57] K. Okamura et al. *Journal of Nuclear Materials*, 329(155-157), 1988.
- [58] L.L. Snead. Limits on irradiation-induced thermal conductivity and electrical resistivity in silicon carbide materials. *Journal of Nuclear Materials*, 329-333:524–529, 2004.
- [59] G.E. Youngblood, D.J. Senior, and R.H. Jones. Fusion materials semiannual progress report doe/er-0313/33. 2002.
- [60] Michael F. Ashby, Anthony Evans, Norman A. Fleck, Lorna J. Gibson, John W. Hutchinson, and Hayden N.G. Wadley. *Metal Foams: A Design Guide*. Butterworth Heinemann, 2000.